

Development of RFQ Particle Dynamics Simulation Tools and Validation with Beam Tests.

DISSERTATION
zur Erlangung des Doktorgrades
der Naturwissenschaften

vorgelegt beim Fachbereich Physik
der Johann Wolfgang Goethe - Universität

von
JOHANNES M. MAUS
aus Frankfurt am Main

Frankfurt am Main 2010
D30

vom Fachbereich Physik der
Johann Wolfgang von Goethe-Universität als Dissertation angenommen.

Dekan: Prof. Dr. D. Rischke
Gutachter: Prof. Dr. A. Schempp
Prof. Dr. U. Ratzinger

Datum der Disputation: 13.12.2010

Contents

0	Zusammenfassung	5
1	Introduction	11
2	Radiofrequency Quadrupole	14
2.1	Principle of an RFQ	14
2.2	Resonator Concepts	17
2.3	Design Strategies	19
2.3.1	LANL Four-Section Design	20
2.3.2	Equipartitioning Design Strategy	22
2.4	Description of the RF field in an RFQ	24
2.4.1	Multipole Coefficient Approximation of RFQ Field	25
3	Poisson Solver	36
3.1	Multigrid Solver	38
3.2	Ingredients of Multigrid Cycles	40
3.2.1	Restriction Operator	43
3.2.2	Prolongation Operator	44
4	Verification of the Multigrid Solver	45
4.1	Examples with no Charges	45
4.2	Examples with Charges	48
4.2.1	Examples with no Image Charge Effect	50
4.2.2	Examples with Image Charge Effect	53
5	RFQ Simulation Results Using the Multigrid Poisson Solver	58
5.1	Description of the Set of Test-RFQs	58
5.2	External Field	60
5.2.1	Illustration of the Field	62
5.2.2	Comparison to Potential of Multipole Expansion Method	67
5.2.3	Comparison of Ex	72
5.2.4	Influence on the Single Particle Dynamics	75
5.2.5	Collective Effects	80
5.2.6	Sensitivity of the Poisson Solver	81
5.3	Internal Field	82
5.3.1	Influence on Single Particle Dynamics	84

5.3.2	Collective Effects	86
5.3.3	Sensitivity of the Poisson Solver	88
5.3.4	Space Charge with Image Charge Effect	89
6	Experiments with the MAFF RFQ	96
6.1	Basics of RF-Structures	98
6.1.1	Quality Factor Q	98
6.1.2	Shunt Impedance	101
6.2	Measurement of Shunt Impedance	102
6.2.1	Perturbation Capacitor	103
6.2.2	Gamma-Spectroscopy	103
6.3	Measurement of the Output Energy	105
6.4	Measurement of the Transmission	107
6.5	Overview of Shunt Impedance Measurements	110
6.6	Comparison to beam dynamic simulations	111
6.7	Conclusion	112
7	Summary	114
	Bibliography	121
	Lebenslauf	122
	Akademische Lehrer	123
	Danksagung	124

0 Zusammenfassung

Die vorliegende Arbeit beschäftigt sich mit der Simulation der Teilchendynamik in Radiofrequenz-Quadrupolen (RFQs) und mit der Durchführung von Strahlungsmessungen an einer RFQ-Struktur, deren Ergebnisse mit der Simulation verglichen werden.

RFQs werden heute für viele unterschiedliche Projekte eingesetzt. Sie sind die erste HF-Beschleunigerstruktur bei fast jedem modernen Linearbeschleuniger (Linac). Ihre Aufgabe besteht darin, den Gleichstromstrahl der Ionenquelle zu fokussieren, zu Teilchenpaketen zu formen (bunchen) und für die Injektion in folgende Strukturen vorzubeschleunigen. Die Endenergie kann dabei zwischen 100 keV/u und mehreren MeV/u liegen. RFQs bestehen im Wesentlichen aus vier Stäben (Elektroden), die einen Quadrupol bilden. Um einen longitudinalen Feldanteil zu erhalten, ist auf den Elektroden eine sinusoidale „Störung“ (Modulation) aufgebracht.

Bei Untersuchungen zur Teilchendynamiksimulation in RFQs wurden verschiedene Programme verglichen und Unterschiede gefunden. Dies ist der Grund, das vorhandene Programm zur Simulation der Teilchendynamik um wesentliche Funktionen zu erweitern, um so zusätzlich die Unterschiede und Abweichungen zu Experimenten erklären zu können. Der Kern dieser Erweiterung stellt ein Multigrid Poisson-Solver dar, der sowohl für die Berechnung der genauen HF-Felder, als auch zur Berechnung der Raumladung unter Berücksichtigung von Bildladungen auf den leitenden Oberflächen verwendet werden kann. Bis dahin wurden die HF-Felder über eine Multipolentwicklung und die Raumladung über eine 2D-Routine mit Näherungen für die Bildladung näherungsweise berechnet.

Das zweite Kapitel dieser Arbeit führt in die Funktionsweise von RFQs ein. Es werden verschiedene Resonatorkonzepte dargestellt und verglichen, mit denen die in der Teilchendynamik gefundenen Geometrien der Elektroden in reale HF-Strukturen umgesetzt werden können. Anschließend werden zwei Strategien vorgestellt, mit denen die Struktur der Elektroden entworfen werden kann. Zum einen handelt es sich um die klassische Methode, die am Los Alamos National Laboratory in den 1980ern entwickelt wurde und zum anderen um das so genannte „Equipartitioning“, bei dem

die Raumladungseffekte des Strahls schon während des Designvorgangs berücksichtigt werden, um ein Ausbalancieren der freien Energie zwischen den verschiedenen Freiheitsgraden zu erreichen, sodass eine Minimierung des Emittanzwachstums erzielt werden kann. Anschließend werden die elektrischen Felder, die zwischen den Elektroden entstehen, ausgehend von der Laplace-Gleichung in Zylinderkoordinaten hergeleitet. Da die Elektroden den wesentlichen kapazitiven Teil des HF-Resonators darstellen und keine (wesentlichen) Ströme auf den Elektroden auftreten, ist der Teil um die Strahlachse frei von magnetischen Feldern und das Vektorpotential kann vernachlässigt werden. Aus Symmetriegründen können etliche Koeffizienten der Multipolentwicklung weggelassen werden. Der einfachste Fall benutzt nur noch zwei Terme (Zwei-Term-Potential) und wurde lange Zeit wegen der eingeschränkten Rechenleistung vorhandener Computer zur Simulation von RFQs eingesetzt. Später wurde die Anzahl der Koeffizienten auf acht erhöht (Multipol-Potential). Unabhängig von der Anzahl der Multipole bleibt der Bereich, in dem dieses Verfahren eine adäquate Darstellung der Felder ist, eingeschränkt. Bei der Simulation von Hochstromanwendungen sowie bei Anwendungen mit kleiner Apertur (lokaler minimaler Abstand Elektrode-Strahlachse) verlassen Teilchen diesen Bereich und erfahren falsche Kräfte. Für kritische Anwendungen wie zum Beispiel IFMIF, wo die transversale Fokussierung wegen des hohen Strahlstroms groß ist und bei denen eine Aussage über die Orte der Teilchenverluste getroffen werden soll, ist eine möglichst genaue Beschreibung der Felder unausweichlich.

Im dritten Kapitel werden die Funktionsweisen des Multigrid Poisson-Solvers und dessen Komponenten erläutert. Zuerst wird das Gauß-Seidel-Verfahren beschrieben, welches ein iteratives, infinites Differenzenverfahren zur Lösung von Differentialgleichungen auf einem Gitter darstellt. Das Mehrgitterverfahren zeigt ein deutlich besseres Konvergenzverhalten als diese Methode. Wichtig ist, dass das Gauß-Seidel-Verfahren die Eigenschaft hat, die hochfrequenten Anteile des Fehlers auf dem Gitter schnell und effektiv zu dämpfen, während die tieffrequenten Anteile kaum reduziert werden und dadurch zum eingeschränkten Konvergenzverhalten beitragen. Für den Multigrid Poisson-Solver wird nun ausgenutzt, dass bei dem Übergang von einem feinen Gitter auf ein gröberes der tieffrequente Anteil des feinen Gitters zu einem hochfrequenten Anteil auf dem groben Gitter wird. Mit der Kombination erhält man einen leistungsstarken Solver. Eine typische Multigrid Iteration kann wie folgt aussehen: Zuerst wird das Potential auf dem feinsten Gitter mit Hilfe von n Durchläufen des Gauß-Seidel-Verfahrens (typisch: $n=4$) geglättet und der Defekt (Abweichung der

linken von der rechten Seite der Poissongleichung) bestimmt und auf ein gröberes Gitter übertragen, wobei für den Defekt wieder eine Differentialgleichung gilt, die die gleiche Form hat wie die Poissongleichung, sodass genauso verfahren werden kann wie zuvor: n Durchläufe des Gauß-Seidel-Verfahren zur Glättung. So wird verfahren bis das grösste Gitter erreicht wird, welches genau gelöst werden muss. Dabei bietet sich wiederum das Gauß-Seidel-Verfahren an, das nun sehr schnell ist, da das Gitter deutlich weniger Gitterpunkte aufweist. Anschließend wird das Ergebnis des grössten Gitters mit Hilfe des Prolongationsoperators auf das nächst feinere Gitter übertragen und verrechnet, um anschließend wiederum mit n Durchläufen des Gauß-Seidel-Verfahrens geglättet zu werden. So wird bis zum feinsten Gitter verfahren. Typischerweise sind fünf solcher Multigriditerationen notwendig, um das Potential um die Strahlachse eines RFQs mit ausreichender Genauigkeit zu bestimmen. Es werden abschließend verschiedene Routinen beschrieben, mit denen der Übergang von einem Gitter auf ein anderes realisiert werden kann, sowie verschiedene Reihenfolgen der Gitter mit verschiedenen Auflösungen.

Da die Felder in RFQs komplex sind, werden zur Überprüfung der Funktionsweise und des Verhaltens des entwickelten Multigrid Poisson-Solvers im vierten Kapitel dieser Arbeit verschiedenen Testprobleme betrachtet. Diese lassen sich in zwei verschiedene Kategorien unterteilen: Probleme ohne Raumladung, bei denen das Potential durch die Randbedingungen (Elektroden) bestimmt wird und Probleme mit einer zusätzlichen Raumladung. Erste sind vergleichbar mit der Berechnung der externen HF-Feldern und zweite mit der Raumladungsbetrachtung der Ionen. Den ersten Test stellt eine einfache Box mit Potential 1 auf den Oberflächen und einem verschwindenden Potential innerhalb der Box als Ausgang für den Solver dar, der innerhalb weniger Schritte die richtige Lösung (homogenes Potential 1) erhält. Anschließend wird das Potential einer kleinen geladenen Kugel in einer geerdeten Box betrachtet, um festzustellen, ob solche kleinen starken Übergänge ein Problem für den Poisson-Solver darstellen. Als letztes Beispiel in dieser Kategorie wurde das Feld eines kleinen Plattenkondensators berechnet, der sich wiederum in einer geerdeten Box befindet. Auch hier wurde innerhalb weniger Rechenschritten das erwartete Potential erhalten. In der zweiten Kategorie wurden zuerst Raumladungsdichten mit der Form eines Zylinders und mit einer Kugel in einem geerdeten größeren Zylinder betrachtet. Dies entspricht in etwa der Situation eines Gleichstromstrahls, der in eine RFQ injiziert wird und später im Verlauf der Struktur zu einem Teilchenpaket „gebuncht“ wurde. Der größere geerdete Zylinder minimiert die Bildladungen. Auch diesen Anforderung-

en kann der implementierte Multigrid Poisson-Solver schnell und effektiv entsprechen. Anschließend wurde die Fähigkeit zur Berechnung von Bildladungen genauer untersucht. Dazu wurde eine Punktladung vor einer geerdeten Platte gesetzt und das erhaltene Potential mit dem Potential von zwei Punktladungen gleicher Ladung jedoch mit unterschiedlichem Vorzeichen verglichen, die sich im doppeltem Abstand Platte Punktladung befanden. Die Potentiale stimmen überein. Abschließend wurden jeweils wieder die Potentiale von Ladungsdichten mit der Form eines Zylinders und einer Kugel, die in einem unmodulierten Quadrupolkanal platziert wurden, betrachtet. Dabei wurde die Apertur variiert und festgestellt, dass dies einen großen Einfluss auf das entsprechende Potential hat und zwar über den kompletten Verlauf von der Strahlachse bis zu den Elektroden hinweg.

Nachdem zunächst einfache Beispiele betrachtet wurden, werden nun im fünften Kapitel die Auswirkungen der verschiedenen Methoden zur Berechnung der Hochfrequenz- und Raumladungsfelder in RFQ-Beschleunigern auf die Transmission einer Gruppe von unterschiedlichen RFQs untersucht. Diese RFQs wurden mit demselben Verfahren generiert und unterscheiden sich in ihrer minimalen Apertur, um so festzustellen, ob die Wahl dieses Parameters von dem verwendeten Simulationsprogramm/Routine abhängt. Zuerst werden die wesentlichen Strukturparameter der RFQs dargestellt und diskutiert. Es handelt sich dabei um IFMIF-ähnliche Designs. Im folgendem Abschnitt werden sowohl die transversalen wie auch die longitudinalen HF-Felder für verschiedene Zellgeometrien illustriert und diskutiert. Danach werden die Potentiale, die durch den Multigrid Poisson Solver berechnet wurden, mit denen von der Multipolentwicklung verglichen. Während im Bereich der Strahlachse beide Methoden zu sehr ähnlichen Potentialen kamen, unterschieden sich diese weiter von der Strahlachse entfernt jedoch zunehmend, wie aus den Grafiken für die relativen und absoluten Unterschiede hervorgeht. Analog zum Potential wurden die einzelnen Komponenten des elektrischen Feldes der verschiedenen Methoden untereinander verglichen. Während normalerweise mit 10^4 bis 10^6 Teilchen gerechnet wird, wurde der Einfluss der Unterschiede in den Feldern auf die Dynamik einzelner Teilchen untersucht. Dazu wurde zuerst das Verhalten des Synchronsteilchens betrachtet, wobei kleine Unterschiede zu erkennen waren, die daher kommen, dass der Poisson Solver die Randfelder vor den Elektroden berechnet und die andere Methode dies nicht kann. Als weiteres, einzelnes Teilchen wurde ein beliebiges Teilchen gewählt und die Impulsänderungen entlang der Struktur mit guter Übereinstimmung gegenübergestellt. Nun wurde der Einfluss auf die Transmission der Test-RFQs mit 10^4 Teilchen untersucht, wobei fest-

gestellt wurde, dass die Kurven der beiden Methoden bis auf diejenigen RFQs gut übereinstimmen, die eine kleine Apertur aufweisen und bei denen viele Teilchen den Elektroden näher kommen. Abschließend zur Betrachtung der HF-Felder wurde die Empfindlichkeit des Solvers auf die Wahl der Gitterauflösung und die der Anzahl von Multigrid Iterationen und Glättschritten untersucht, um festzustellen welche Mindestwerte eingehalten werden müssen. Für die Raumladungsberechnung wurde analog verfahren, wobei nun sowohl zwischen einer alten Raumladungsroutine als auch zwischen dem Multigrid Poisson Solver mit und ohne Bildladung unterschieden wurde. Die Betrachtung des Verhaltens eines einzelnen Teilchens ergab auch hier gute Übereinstimmungen. Für den Vergleich der Transmission der verschiedenen RFQs wurden zuerst nur Simulationen ohne Bildladung betrachtet. Insgesamt wurde der Multigrid Poisson Solver mit zwei bekannten Raumladungsroutinen verglichen, wobei die 2D Vergleichsroutine etwas niedrigere Transmissionen vorhersagt, aber die anderen beiden Routinen liegen dicht beieinander. Weiterer Vorteil des Multigrid Poisson Solvers ist die deutlich kürzere Rechendauer. Auch hier wurde wieder die Empfindlichkeit des Multigrid Solvers auf die Wahl der oben genannten Parameter untersucht. Im letzten Teil des Kapitels wurde der Effekt der Bildladungen auf den Elektroden untersucht. Dafür wurden nur die Randbedingungen des Gitters auf die Form der Elektroden abgeändert. Zuerst wurden die entstandenen Felder und Potentiale verglichen. Dabei wird deutlich, dass der Effekt der Bildladungen erstens in der Nähe der Elektroden sehr groß ist und zweitens auch über den gesamten Bereich beeinflussend ist. Dies wird in der Transmission der Gruppe von Test-RFQs besonders deutlich. Die Transmission wurde bei allen RFQs reduziert, wenngleich der Effekt für RFQs mit kleiner Apertur besonders groß ist ($\sim 10\%$). Dies ist deutlich mehr, als durch andere Methoden, die den Strahl durch Punkt- und Linienladungen darstellen und den Effekt durch Näherungen berechnen, bestimmt wurde. Dies kann erklären, warum Hochstrom-RFQs oftmals eine geringere Transmission haben, als durch Simulationen vorhergesagt wurde.

Das letzte Kapitel dieser Arbeit befasst sich mit der experimentellen Arbeit an einem RFQ-Beschleuniger. Dazu wird zunächst ein kleiner Überblick über die wesentlichen HF-Parameter gegeben: Resonanzfrequenz, Güte und R_p -Wert. Danach wird das MAFF (Munich Accelerator for Fission Fragments) Projekt beschrieben, für welches die RFQ gebaut wurde. Die Maschine wurde am IAP an einem Teststand aufgebaut, aber es konnte zunächst kein beschleunigter Strahl am Ausgang der RFQ gemessen werden. Die Fragestellung war, warum die Struktur nicht beschleunigt und

ob es strahldynamische Gründe dafür gibt, die mit Hilfe des Programms, das im ersten Teil dieser Arbeit beschrieben wurde, analysiert und gefunden werden können. Dafür war es notwendig, den Zustand der Maschine hinreichend genau zu messen, um andere mögliche Fehlerquellen ausschließen zu können. Es wurde der R_p -Wert, der angibt, wie effektiv die eingekoppelte HF-Leistung in Beschleunigungsspannung umgesetzt werden kann, mit unterschiedlichen Methoden gemessen. Bei der Gammaskopie bei unterschiedlichen Leistungspegeln wurde eine Schwachstelle der Maschine gefunden, die die Feldverteilung im Resonator störte. Dies wurde durch Simulationen nachvollzogen. Im nächsten Schritt wurde ein Energiespektrum des beschleunigten Strahls aufgenommen. Es wurde festgestellt, dass die RFQ Protonen zu der Designenergie beschleunigen kann. Die Transmission der Maschine wurde mit einem Heliumstrahl gemessen und zu etwa 75% bestimmt. Zum Schluss wurden die Messergebnisse mit denen der Simulation verglichen. Im Rahmen der Messgenauigkeit konnte eine gute Übereinstimmung festgestellt werden.

Mit Hilfe des in dieser Arbeit integrierten Multigrid Poisson Solvers konnte die Genauigkeit der Strahldynamikrechnungen vor allem bei Hochstromanwendungen und bei RFQ-Beschleunigern mit kleiner Apertur deutlich verbessert werden. Es stellte sich heraus, dass der Einfluss der Bildladungen bisher unterschätzt wurden. Mit den Programmentwicklungen lässt sich die Teilchendynamik zukünftiger RFQs realistischer simulieren und hilft damit bessere Designs zu entwerfen mit kleinem Emittanzwachstum und hoher Transmission.

1 Introduction

Accelerators are spread all over the world and are used for many different applications. They are designed to deliver ion beams of a certain energy, species, current, brilliance etc. They consist of an ion source, which produces the ions for accelerations, acceleration structures, transport sections, diagnostic modules and a target area depending on the purpose of the accelerator. There are two main type of applications: fundamental research and secondary applications making use of high energy ion beams.

To gain information about an object in small scales the interaction between the object and radiation can analyzed. The resolution scales with the wavelength and therefore with the energy of the radiation. Accelerators are used to produce high energy beams with small wavelength to analyse the configuration of matter by observing the scattered beam after passing through the sample.

On the other side accelerators are used as synchrotron light sources to produce light with special characteristics such as high brightness, high intensity and low emittance as well as high level polarization. Free electron lasers (FEL) are used to produce coherent light of high power of a wide range of wavelength. The XFEL is designed to produce x-rays of about 1 nm.

In nuclear physics and atomic physics, accelerators are needed for a wide range of different research areas such as interaction between nucleus and electron cloud, nuclear reaction up to high energies, verification of the standard model, study and generation of exotic nuclei, antiprotons and high compressed matter, exact mass measurements, or to generate a quark-gluon plasma, just to mention a few. Another exciting application of accelerators is to build a neutron source, which then can be used in many ways. An example for an existing neutron source is the Spallation Neutron Source (SNS) at the Oak Ridge National Laboratory in Tennessee, USA which provides neutrons for a variety of experiments and material improvements. At the IAP in Frankfurt a neutron source is currently under development and will be used e.g. for the analysis of neutron capture processes, which is important for the understanding of the nucleo synthesis in stars and especially in red giants and to study the n-capture

cross-sections of elements which part of radioactive waste more accurately [MCM⁺06]. Two further neutron source projects should be mentioned as well: the International Fusion Materials Irradiation Facility (IFMIF) and the European research programme for the transmutation of high level nuclear waste in an accelerator driven system (Eurotrans). The aim of the first project is to simulate neutron fluxes similar to the one expected in fusion reactors to find material which can resist these fluxes.

Another field where accelerator are commonly used are commercial applications such as application in medicine, doping of semiconductors, sterilization, and material analysis. In the medicine they are for treatments e.g. brain tumors and for various diagnostics.

As the wide range of applications suggest, the different demands on the accelerator in terms of ion species (or electrons), energy, beam current and quality, operating frequency and much more will lead to completely different designs depending on the purpose of the machine. Designing and building such machines or even parts of such machines is therefore a quite challenging task. Moreover, the boundary of realizable machines is continuously pushed to higher levels.

This thesis deals with one accelerator structure which is normally used as the first stage of a linear hadron accelerator: the radio-frequency quadrupole (RFQ). It bunches, focuses and accelerates particles from some 1 – 100 keV/u up to several MeV/u. The first part of this thesis covers the development of a fast, accurate tool to simulate the particle dynamics inside the fields of an RFQ which is very important, since the design cannot be readjusted once the machine is built. Therefore an existing program (PteqHI) was used and the description of the electric field as well as the space and image charge fields was enhanced from a semi analytic description with numerically calculated coefficients to a multigrid Poisson solver, which takes the exact boundaries into account. The effects of a more realistic description of the field inside the RFQ will be presented. Especially the image effects have been underestimated by the old routines. For high energy and high current applications such as neutron sources a precise knowledge of the behavior of the beam inside the structure is needed to reduce losses in the high energy part of the RFQ to avoid activation of the accelerating structure. Accurate simulations are needed as well to determine suitable designs, which reduce beam losses and emittance growth compared to existing designs while shorten the overall length of the RFQ.

The first chapter gives a small introduction to radiofrequency quadrupole accelerators. Different types of resonator structures are described as well as two different

design strategies. Afterwards, the potential and the electric field needed for the beam dynamic calculations in an RFQ are discussed. In chapter 3 the concept of a multigrid Poisson solver is described, which has been implemented as a part of this thesis. In the following chapter some basic (test) problems are used to test the solver. In chapter 5 a set of 12 different RFQs (designs), which have been generated following the same rules with one parameter varied, is used to analyze effects of a more accurate description of the fields. It is shown that the accuracy of the old multipole expansion method is limited for the RF fields and that the old space charge routines are restricted as well. The advantages of the new Poisson solver are explained. The new implemented multigrid Poisson solver is for both (RF field and space charge field (with image effect)) a better representation of the actual field especially for critical high current applications and for precise loss estimations.

The last chapter deals with experimental work at an existing RFQ. After a small introduction to the MAFF project for which the RFQ was designed, some basic RF parameters are introduced and measurements at the MAFF-IH RFQ including the transmission, output energy, and shunt impedance of the structure is presented. The experimental results will then finally be compared to the particle dynamic simulations of that RFQ.

2 Radiofrequency Quadrupole

The radio frequency quadrupole (RFQ) was invented in 1969 by Kapchinsky and Teplyakov at the Moscow Experimental and Theoretical Physics Institute (ITEP) [KT70]. This idea led to the first operating prototype in 1974 in the UDSSR. In 1978 physicists at the Los Alamos National Laboratory (LANL) picked up the idea of the RFQ and made major contributions in terms of investigation on beam dynamics including space charge effects leading to the program PARMTEQ which is widely used today. The outstanding features of the RFQ were demonstrated in a “proof of principle” experiment in 1980 [CSW79], [Kle83]. In the following years the RFQ became so popular that many laboratories and universities throughout the world built and commissioned RFQs; especially in Frankfurt at the IAP, where a different type of resonance structure was invented [Sch90]. The RFQ has the ability to replace the electrostatic accelerators which were used as injectors for further RF-accelerators (DTLs) and therefore to reduce the length of the accelerator and to increase beam current. The main function of an RFQ is to bunch an incoming DC beam of particle and to accelerate the beam to an energy up to ~ 5 MeV/u. Over the whole structure the beam is kept focused by alternating gradient focusing. These three functions are realized with the RF fields only.

2.1 Principle of an RFQ

Figure 2.1 shows a set of four electrodes forming an electrical quadrupole. The polarity of the electrodes alternates with time. The variation of the voltage and the movement of particles along the beam axis lead to an alternating gradient focusing similar to magnetic/electrostatic quadrupole lenses. Particles injected into the electric quadrupole have an initial correlation (phase) to the applied RF voltage. As the particles travel through the channel, their position and the electric field change. If the longitudinal velocity of the particles remains unchanged, each position can be associated with a certain electric field and the longitudinal periodicity depends on the

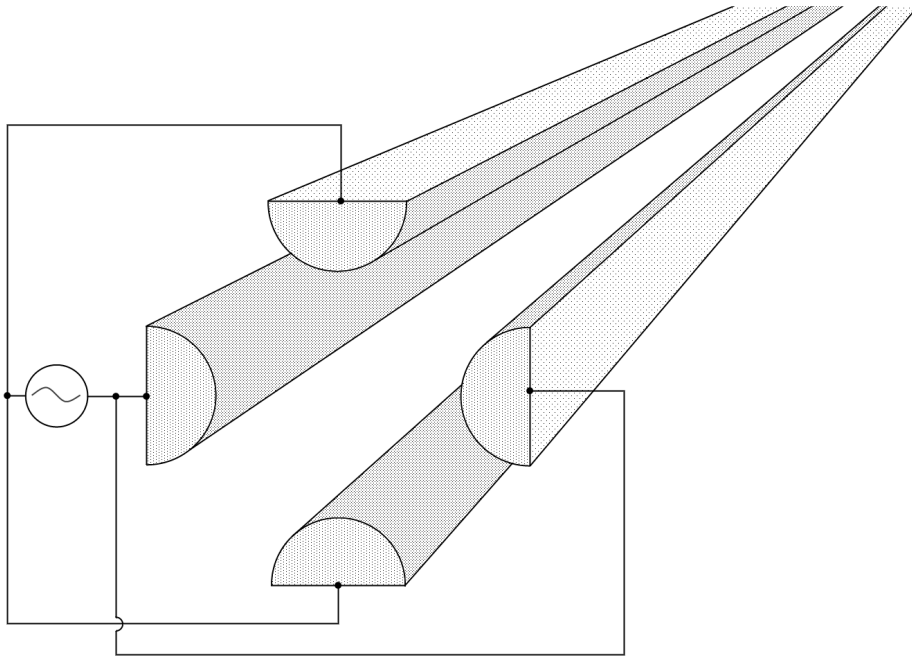


Figure 2.1: Quadrupole with time varying polarity.

velocity of the particle and the wavelength of the RF field ($\beta\lambda$)

In the first half of an RF period the particle is exposed to a focusing field in one plane and to a defocusing field in the other plane. In the second half of the RF period the polarity of the field has changed and therefore the focusing field of the first plane has changed to a defocusing field. If the electric field and therefore the forces are chosen suitably, an overall focusing of the particles can be achieved. This is the situation of the alternating gradient focusing without the longitudinal end effects like in static quadrupoles.

Because the geometry of the electrodes described above does not introduce any longitudinal field components, this setup can not be used to form bunches and to accelerate. In order to generate longitudinal field components the quadrupole symmetry of the electrodes needs to be disturbed. This is shown in Figure 2.2. When the vertical electrode has a distance a from the beam axis, the horizontal electrode has a distance of $a \cdot m$ from the axis. a is known as the aperture and m is the modulation which is typically varied between 1 and 3. After a certain distance c_L the perturbation has changed, so that vertical electrode has a distance of $a \cdot m$ and the horizontal of a from the beam axis. If the distance c_L is synchronized to the RF field and the

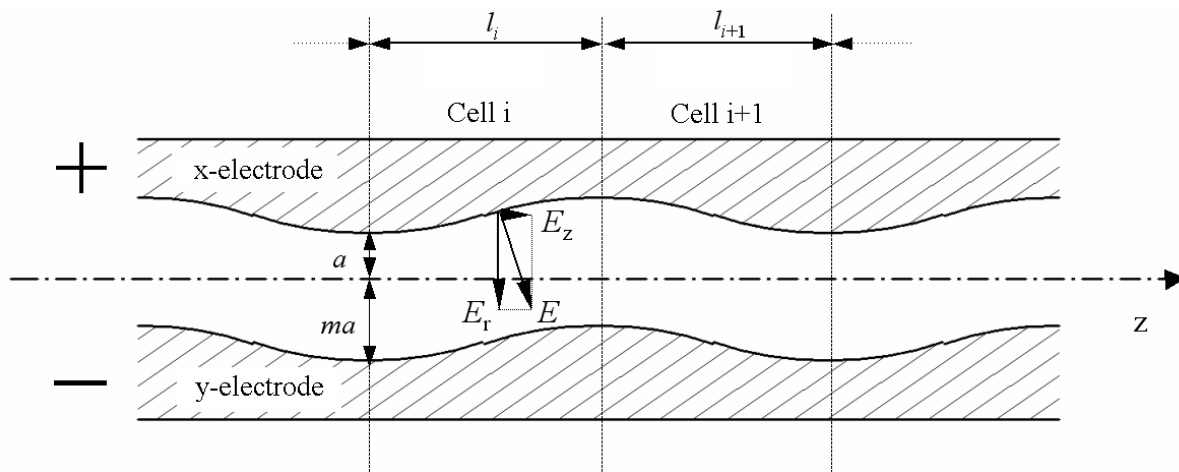


Figure 2.2: Quadrupole with time varying polarity and modulation.

particle's velocity

$$c_L = \frac{\beta\lambda}{2} \quad (2.1)$$

the particle sees a net accelerating field in every cell. This is the key idea of the RFQ principle. Typical values for the cell length c_L are between 1 cm and 10 cm. A setup of electrodes like the one shown in Figure 2.2 is now able to bunch and accelerate particles longitudinally and to keep them focused in the transverse plane at all time.

Due to the nature of the Gauss's law

$$\nabla \mathbf{E} = \frac{\rho}{\epsilon_0} \quad (2.2)$$

it is not possible to form a focusing electrical field in all three planes at the same times if no charge is involved to form the field ($\rho = 0$). (Gauss's law can be used, since the situation of a particle moving in time with a electromagnetic wave is virtually static ($d \ll \lambda$.) That is why a longitudinal field will lead to a so called transverse RF defocusing force. So the parameters of the RFQ have to be chosen to assure that the beam remains well focused over the complete structure.

2.2 Resonator Concepts

The frequency range of RFQs starts from some 10s MHz and goes up to several 100s MHz and for different frequencies, different resonator concepts are used to achieve well working machines. The first RFQs were four vane type RFQs shown in Figure 2.3. The four vane RFQ is a cavity resonator with four vanes mounted inside which form the quadrupole. In order to generate the correct field, a quadrupole symmetric electrical transverse mode has to be excited. The TE_{210} mode is applied. The third index indicates that the longitudinal field distribution has no fluctuation. Since the four vane RFQ is a cavity resonator, the geometric size of the structure scales with the resonance frequency and for low frequencies the structure becomes unpractically large in diameter (a 100 MHz four vane structure has a diameter of about 1 m).

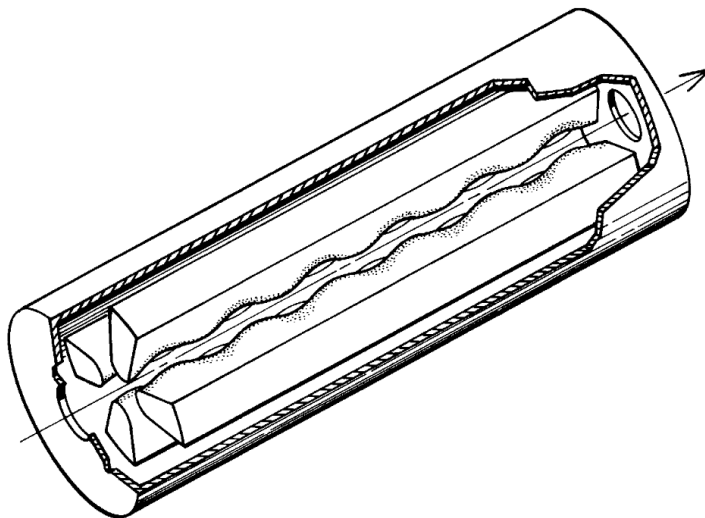


Figure 2.3: Four vane type RFQ [CSW79].

The split coaxial type RFQ is shown in Figure 2.4. It is mostly used for low frequencies (below 100 MHz), because it is a relatively compact machine in this frequency range [AFM⁺89], [LLD⁺89].

The four rod type RFQ shown in Figure 2.5 is made up of strong coupled $\frac{\lambda}{4}$ -resonators. The $\frac{\lambda}{4}$ -resonators are capacitively shortened with the electrodes forming the capacity. The support plate and the ground plate form the inductance [Sch90]. Since the four rod RFQ is a line resonator, the tank has only minor influences on the RF behavior of the structure compared to other types. Another advantage is that they are easy to access and to adjust.

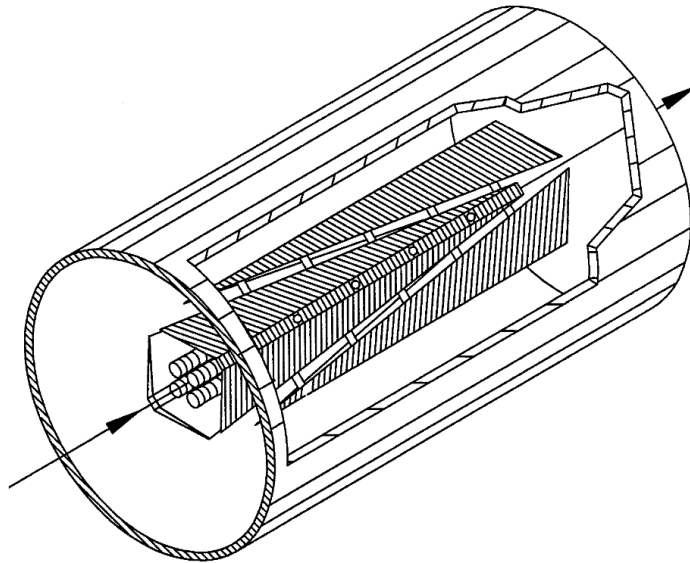


Figure 2.4: Split coaxial type RFQ [Mül79].

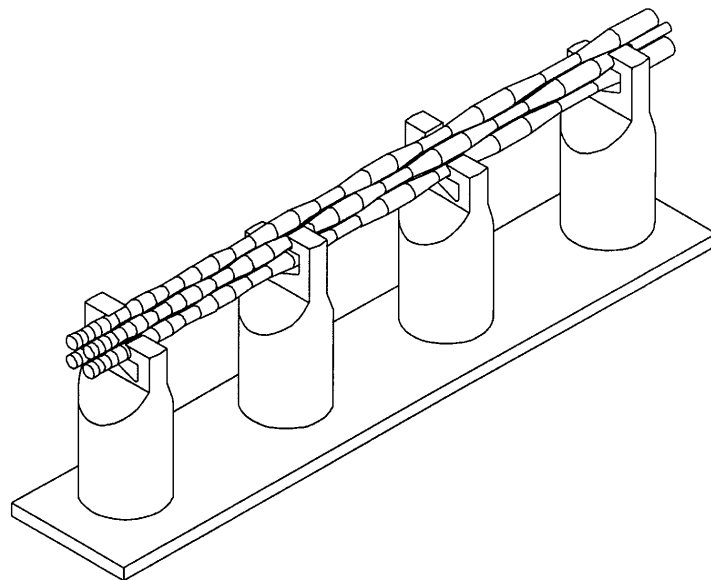


Figure 2.5: Four rod type RFQ.

The last type of RFQs is the IH-type RFQ shown in Figure 2.6. It is a cavity resonator in which the TE_{111} mode is excited. The electrodes are placed on rings which are mounted on the supports [Rat98] [Rat96].

For high frequencies above 300 MHz a four vane type RFQ is normally pre-

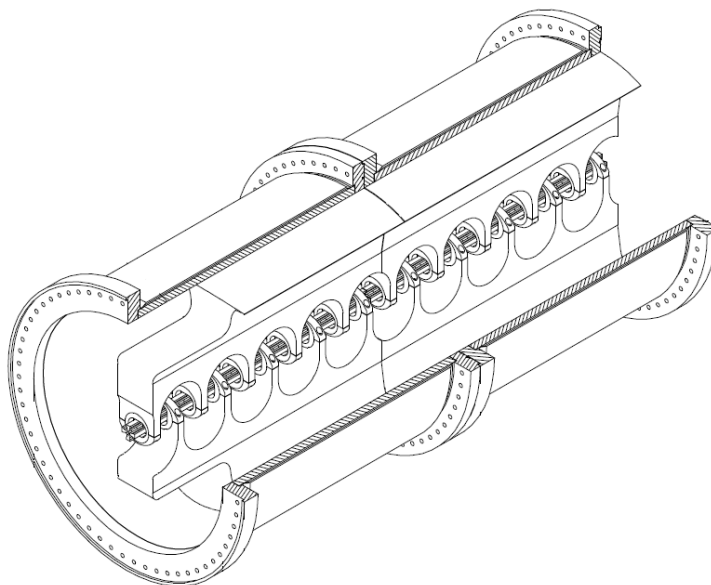


Figure 2.6: IH type RFQ (36 MHz machine at GSI) [Rat96].

ferred, because this type of resonator has than feasible dimensions and good RF performance.

If the frequency is lower than 100 MHz the dimensions of a four vane type RFQ becomes impractically big and the four rod or the IH type RFQ result in smaller structures. In between, the four rod, four vane or the IH type RFQ can be used.

2.3 Design Strategies

There are many different strategies to design RFQs and to achieve suitable RFQs. Every RFQ has its own purpose and has to meet its own requirements which differ from one machine to another. Contrary to the assumption that a high transmission is the main goal in designing RFQs, there are many different considerations to balance. Reducing the overall length of the RFQ will lead to a proportional cheaper and easier to machine structure. If the intervane voltage is reduced, less RF power is needed to achieve its working point. There are a variety of different parameters, which interact,

and can be chosen freely to some extent. The goal of designing an RFQ is to determine the shape of the vanes inside the RFQ, when parameters like ion species, initial and final energy, frequency and intervane voltage (which can also be varied along the structure) or the desired space-charge physics focusing characteristics are given. The shape is described with the following geometric functions: aperture $a(z)$, modulation $m(z)$, cell length $cl(z)$ (respectively phase $\phi_s(z)$), where z is the axial distance along the structure. Two different design strategies will be described in more detail.

2.3.1 LANL Four-Section Design

The standard design of an RFQ to control the beam was developed at LANL in the 1980s. The RFQ is subdivided into four sections performing different tasks depending on the shape of the beam at the current stage. The sections are radial matching section, shaper, gentle buncher, and accelerating section. They will be described here in more detail.

In order to obtain these functions, certain rules need to be formulated. Kapchinsky and Teplyakov already proposed to keep the longitudinal phase advance for zero current σ_{t0} and the spatial length of the separatrix Z_B constant.

$$Z_B = \frac{\beta\lambda\psi}{2\pi} \quad (2.3)$$

where ψ is the angular length of the separatrix, which is related to the synchronous phase ϕ_s by:

$$\tan \phi_s = \frac{\sin \psi - \psi}{1 - \cos \psi} \quad (2.4)$$

The idea of Kapchinsky and Teplyakov was to keep the charge density distribution approximately constant, while accelerating and bunching the beam, which should reduce space charge effects like radial emittance growth. A constant charge density can be achieved by constant Z_B and constant σ_{t0} . The invariance of Z_B determines ϕ_s with equations 2.3 and 2.4. The function $A(z)$ (defined in equation 2.43) is then determined by equation 2.66 and therewith the aperture $a(z)$. The disadvantage of this method is that the function $A(z)$ takes on small values especially for large synchronous phases, which leads to long structures, particularly as the input synchronous phase approaches -90° . To avoid this the initial synchronous phase has to be changed which reduces the

capture efficiency of the RFQ. In order to overcome this problem two new invariants are defined to replace σ_{l0} and Z_B :

$$\epsilon = \frac{-2\pi\sigma_{l0}}{\sigma_{l0}^2} \quad (2.5)$$

$$\alpha = \sigma_{l0}Z_b^2. \quad (2.6)$$

A positive ϵ yields to a decreasing σ_{l0} with a constant percentage rate and therefore the separatrix length Z_B slowly increases. The advantage of this approach is the ability to compress and expand a charge density in its size depending on the choice of ϵ [CSW79]. With the described procedure the beam can be bunched without introducing a high radial emittance growth. Therefore this section is referred to as the gentle bunching section [Wan98]. In order to increase the capture efficiency, another section is added in front of the gentle bunching section, which has a synchronous phase of $\phi_s = -90^\circ$, where the separatrix has the largest phase width and therefore best longitudinal acceptance, and an initial value for the acceleration efficiency $A = 0$. This section is referred to as the shaper section. Following the gentle bunching section a fourth section is added, which keeps the exit value of the gentle bunching section constant to accelerate the particles further. Hence, it is called accelerator section. The last

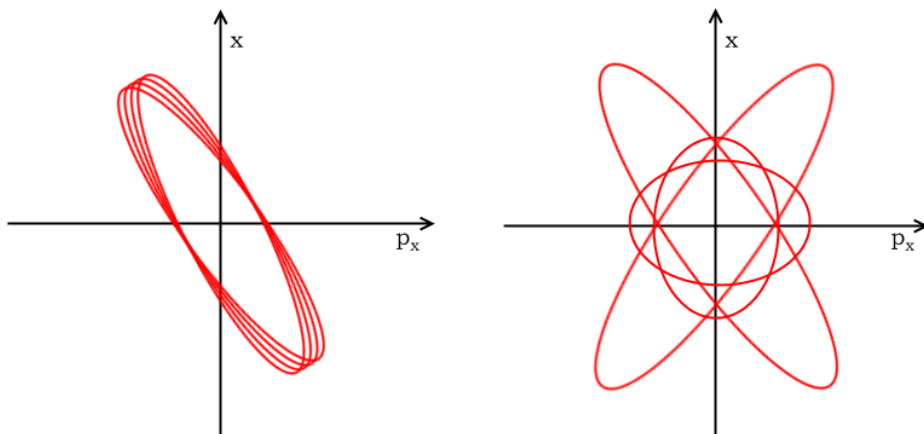


Figure 2.7: The acceptance of an RFQ with and without a Radial Matching Section.

problem to be solved is to inject a DC beam into a time-varying focussing/accelerating channel, which has a time depending acceptance, since the matched ellipse parameters of the shaper section do not depend on the RF phase and are relatively independent of the position along the RFQ. This is done in the radial matching section by tapering the

electrodes at the input of the structure, in the manner that the focussing strength χ changes from almost zero to its full value at the start of the Shaper Section after some focussing periods [Cra84]. There is no modulation ($m = 1$) in the radial matching section, so it is purely quadrupole symmetric. The acceptance of an RFQ with and without a radial matching section is shown in Figure 2.7. A secondary advantage of the radial matching section is that it reduces fringe field effects for both longitudinal and transverse motions by increasing the aperture at the beginning of the RFQ. A typical LANL design is shown in Figure 2.8, indicating how the parameters change in an RFQ of this type and the different sections.

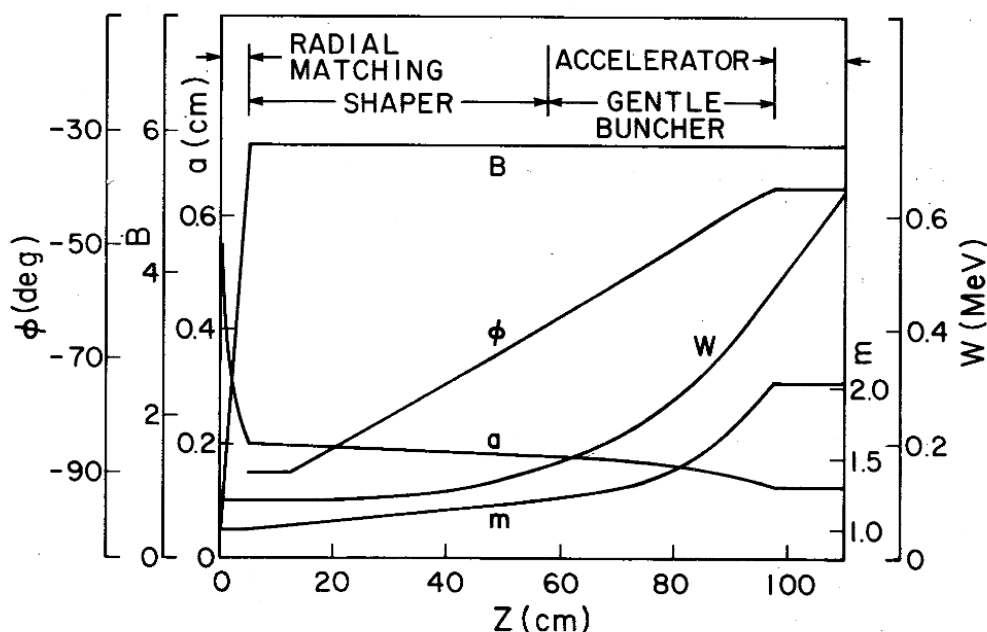


Figure 2.8: Example of a LANL design for a 425 MHz [CSW79].

The LANL design strategy can be improved by allowing more variation of the parameters to gain shorter RFQs with small emittance growth. For instance B is kept constant over nearly the whole RFQ in the LANL concept, but rising B linearly and keeping the geometric length of the bunch constant can lead to compact RFQs with high transmission [Sch96].

2.3.2 Equipartitioning Design Strategy

While designing an RFQ according to the classic LANL approach described above, the behavior of the beam in terms of beam sizes and space charge effects is not fully taken

into account. The consequence is that the matched conditions of the beam are not always satisfied causing beam halo formation and radial emittance growth especially in high current machines, when the beam dynamics is dominated by space charge effects [Jam93]. In the case of a matched beam, the beam-density contours coincide with the ellipses corresponding to the particle trajectories that requires a smooth and coordinated change of the parameters [ZJZ⁺08]. The matching equations according to the smooth approximation theory are

$$\epsilon_{tn}^2 = \frac{a_t^4 \gamma^2 \sigma_t^2}{\lambda^2} \quad (2.7)$$

$$\epsilon_{ln}^2 = \frac{a_l^4 \gamma^6 \sigma_l^2}{\lambda^2}, \quad (2.8)$$

where ϵ is the normalized RMS emittance, σ is the phase advance with beam current, a_t and a_l are the transverse and longitudinal RMS beam radii (assuming an ellipsoidal particle distribution). The idea of the equipartitioning design is to balance the internal energies in the beam between the transverse and longitudinal degrees of freedom. Doing so, the free energy that could cause emittance growth, is minimized and the beam is in equilibrium [Jam81]. If that is the case the following equation is satisfied

$$\frac{\epsilon_{ln} \sigma_l}{\epsilon_{tn} \sigma_t} = \frac{\epsilon_{ln} a_t}{\epsilon_{tn} a_l} = 1 \quad (2.9)$$

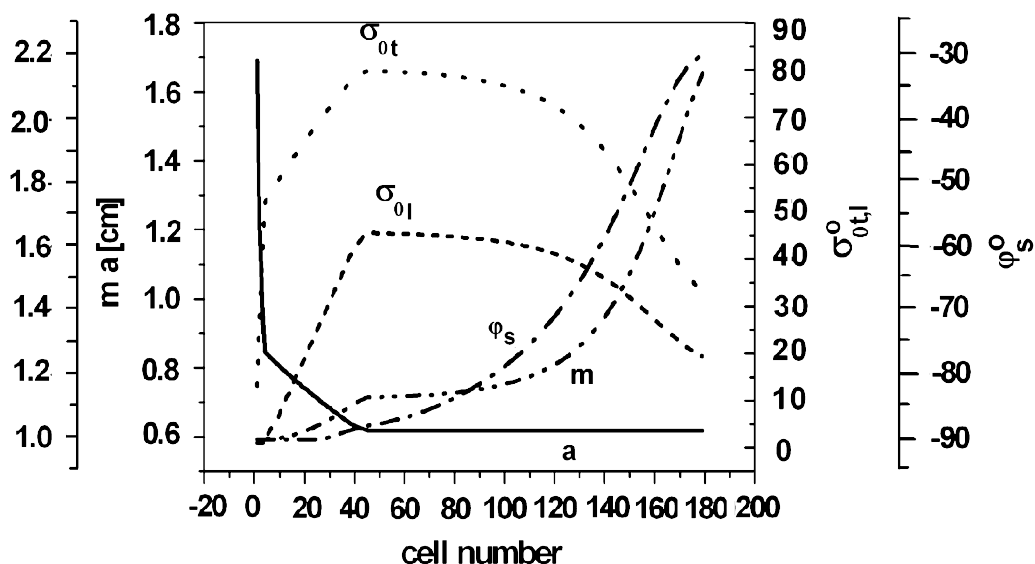


Figure 2.9: Example of an equipartitioning design [ZJZ⁺08].

An equipartitioning design is achieved by combining equations 2.7, 2.8 and 2.9 to gain rules for the choice of the parameters $a(z)$, $m(z)$ and $\phi_s(z)$. An example of the evolution of the main parameters of an RFQ designed with the equipartitioning strategy is shown in Figure 2.9.

2.4 Description of the RF field in an RFQ

All different types of RFQ structures have in common that there is no magnetic field in the region close to the beam axis. Only the electric field is present there and acts on the particles. This concurs with the fact that the area around the beam axis refers to the capacitive component of the RF-structure. Therefore, the vector potential \mathbf{A} of the Maxwell equation

$$\mathbf{E} = -\nabla\Psi - \frac{\partial\mathbf{A}}{\partial t} \quad (2.10)$$

can be neglected and the electric field is then a pure function of a scalar potential Ψ

$$\mathbf{E} = -\nabla\Psi. \quad (2.11)$$

The benefit from the neglect of the vector potential is that the beam dynamics can be studied independently of the electrodynamic behavior of the structure. Only the solution of the electrostatic Laplace equation has to be known.

$$\Delta\Psi = 0 \quad (2.12)$$

The time dependency is a pure sinusoidal one.

$$\Psi = \Phi \cdot \sin(\omega t - \phi) \quad (2.13)$$

So in order to find the field in the useful region of an RFQ near the beam axis, the Laplace equation has to be solved taking the electrodes as the boundary conditions into account. Three options are possible: the first is to solve the equation analytically and to machine the electrodes to fit the analytical answer. It has to be noted that it is not possible to machine electrodes following the exact analytical shape due to high peak fields which will lead to sparking and therefore prohibit reliable operation. The electrodes will be machined somewhat close to the analytical answer and show directly

one disadvantage of this method. The second method is to approximate the field near the beam axis by a cylindrically symmetric analytical approximation; this method was derived by Kapchinsky and has been the primary method of use. The third option is to solve the Laplace equation numerically on a grid for given and realizable shape of the electrodes. The implementation of this method is part of this thesis.

2.4.1 Multipole Coefficient Approximation of RFQ Field

The symmetry of the RFQ suggests to describe the Laplace equation (2.12) in cylindric coordinates [Jac62]:

$$\frac{1}{r} \frac{\partial}{\partial r} \left(r \frac{\partial \Phi(r, \theta, z)}{\partial r} \right) + \frac{1}{r^2} \frac{\partial^2 \Phi(r, \theta, z)}{\partial \theta^2} + \frac{\partial^2 \Phi(r, \theta, z)}{\partial z^2} = 0. \quad (2.14)$$

To solve equation 2.14 an ansatz is chosen where Φ is the product of three functions depending on r , θ , and z respectively

$$\Phi(r, \theta, z) = R(r) \cdot \Theta(\theta) \cdot Z(z). \quad (2.15)$$

Inserting equation 2.15 into equation 2.14 leads to

$$\frac{1}{r} \left(\frac{\partial R}{\partial r} + r \frac{\partial^2 R}{\partial r^2} \right) \Theta Z + \frac{1}{r^2} \frac{\partial^2 \Theta}{\partial \theta^2} R Z + \frac{\partial^2 Z}{\partial z^2} R \Theta = 0 \quad (2.16)$$

Then multiplying by $\frac{1}{R\Theta Z}$

$$\frac{1}{R} \frac{\partial^2 R}{\partial r^2} + \frac{1}{r \cdot R} \frac{\partial R}{\partial r} + \frac{1}{\Theta \cdot r^2} \frac{\partial^2 \Theta}{\partial \theta^2} + \frac{1}{Z} \frac{\partial^2 Z}{\partial z^2} = 0 \quad (2.17)$$

$$\Rightarrow \frac{1}{R} \frac{\partial^2 R}{\partial r^2} + \frac{1}{r \cdot R} \frac{\partial R}{\partial r} + \frac{1}{\Theta \cdot r^2} \frac{\partial \Theta}{\partial \theta} = -\frac{1}{Z} \frac{\partial^2 Z}{\partial z^2} \quad (2.18)$$

Since, equation 2.18 needs to be true for arbitrary r , θ , and z , both sides of the equation have to be constant and equal:

$$-\frac{1}{Z} \frac{\partial^2 Z}{\partial z^2} = k^2 \quad (2.19)$$

$$\frac{1}{R} \frac{\partial^2 R}{\partial r^2} + \frac{1}{r \cdot R} \frac{\partial R}{\partial r} + \frac{1}{\Theta \cdot r^2} \frac{\partial^2 \Theta}{\partial \theta^2} = k^2 \quad (2.20)$$

Equation 2.19 describes the z -dependency of the potential Φ :

$$\frac{\partial^2 Z}{\partial z^2} \pm k^2 Z = 0, \quad (2.21)$$

where k is an arbitrary constant. The solution of equation 2.21 depends on the sign of the constant k . The solution for the three cases are:

$$k < 0 : Z(z) = A \cdot \sinh(kz) + B \cdot \cosh(kz) \quad (2.22)$$

$$k > 0 : Z(z) = A' \cdot \sin(kz) + B' \cdot \cos(kz) \quad (2.23)$$

$$k = 0 : Z(z) = A'' \cdot z + B'' \quad (2.24)$$

Equation 2.20 can be converted to:

$$\frac{r^2}{R} \frac{\partial^2 R}{\partial r^2} + \frac{r}{R} \frac{\partial R}{\partial r} - r^2 \cdot k^2 = -\frac{1}{\Theta} \frac{\partial^2 \Theta}{\partial \theta^2} \quad (2.25)$$

Following the same argument as for equation 2.18, one obtains:

$$\frac{r^2}{R} \frac{\partial^2 R}{\partial r^2} + \frac{r}{R} \frac{\partial R}{\partial r} - r^2 \cdot k^2 = m^2 \quad (2.26)$$

$$\frac{1}{\Theta} \frac{\partial^2 \Theta}{\partial \theta^2} = m^2 \quad (2.27)$$

The solution for the angular dependency of the potential is of the same kind as the solution for the longitudinal dependency:

$$m < 0 : \Theta(\theta) = A \cdot \sinh(m\theta) + B \cdot \cosh(m\theta) \quad (2.28)$$

$$m > 0 : \Theta(\theta) = A' \cdot \sin(m\theta) + B' \cdot \cos(m\theta) \quad (2.29)$$

$$m = 0 : \Theta(\theta) = A'' \cdot \theta + B'', \quad (2.30)$$

where m is a constant. For the solution of equation 2.26 the signs of k and m have to be taken into account. For the cases $k < 0 \wedge m < 0$ and $k < 0 \wedge m = 0$ (and for $k > 0 \wedge m < 0$, if m is replaced by $i \cdot m$) the solution for the radial component of the potential is:

$$R(r) = a \cdot I_m(kr) + B \cdot I_{-m}(kr) + C \cdot K_m(kr) + D \cdot K_{-m}(kr), \quad (2.31)$$

where $I_{\pm m}$ and $K_{\pm m}$ are the modified Bessel functions of the first respectively second class and of m order. For the cases $k < 0 \wedge m > 0$ and $k > 0 \wedge m = 0$ (and for $k, m > 0$, if m is replaced with $i \cdot m$) the solution of equation 2.26 is:

$$R(r) = A \cdot J_m(kr) + B \cdot J_{-m} + C \cdot Y_m(kr) + D \cdot Y_{-m}(kr), \quad (2.32)$$

where $J_{\pm m}$ and $Y_{\pm m}$ are the Bessel functions of the first respectively second class and of m order. For the case, where $k = 0$, the dependency of the radial component has the following form:

$$m < 0 : R(r) = A \cdot r^m + B \cdot r^{-m} \quad (2.33)$$

$$m > 0 : R(r) = A' \cdot \cos(m \cdot \log(r)) + B' \cdot \sin(m \cdot \log(r)) \quad (2.34)$$

$$m = 0 : R(r) = A'' \cdot \log(r) + B'' \quad (2.35)$$

The general solution of the potential Φ in cylindric coordinates is a linear combination of the single solutions [Dup00].

Taking the symmetry of the quadrupole into account, m needs to be an even number with the consequence that $I_m(kr)$ and $I_{-m}(kr)$ are identical. If it is assumed that the structure is periodic in z , which means that the change in modulation is neglected, then $k \rightarrow n \cdot k$ with $k = \frac{2\pi}{\beta\lambda}$, where n is an even number. Therefore, the potential has the following form:

$$\Phi(r, \theta, z) = \frac{V_0}{2} \left[\sum_{m=0}^{\infty} A'_{0m} r^{2m} \cos(2m\theta) + \sum_{m=0}^{\infty} \sum_{n=1}^{\infty} A'_{nm} I_m(kr) \cos(2m\theta) \cos(nkz) \right]. \quad (2.36)$$

Two Term Potential

In practice equation 2.36 will not be used directly, but with a reduced number of coefficients. The simplest choice is to just use the first two coefficients, which leads to the so called two term potential. Back in the 1980s when the first simulation tools were implemented a two term potential approach was used. It has to be noted that real electrodes cannot be machined following this formula, due to practical reasons and peak surface fields. So making use of the two term potential for beam dynamics is an approximation of the fields inside the structure near the beam axis, which has been a good solution back in the days when calculating capacity of computers was limited.

The first two coefficients of equation 2.36 are the A_0 and the A_{10} term and the potential is then [CWY⁺05]:

$$\Phi(r, \theta, z) = [A_0 r^2 \cos(2\theta) + A_{10} I_0(kr) \cos(kz)]. \quad (2.37)$$

The values of the coefficients A_0 and A_{10} are determined from the boundary conditions appropriate to the electrode geometry. A_0 term refers to a pure quadrupole term being responsible for the transverse field and therefore the transverse AG focusing of the RFQ. The A_{10} term is a monopole term which is responsible for the longitudinal field. The potential can be rewritten in the following sense. At a certain time of the RF period the potential of the horizontal and vertical electrodes are $+\frac{V_0}{2}$ and $-\frac{V_0}{2}$. At the longitudinal position $z = 0$ the horizontal vane tip has a distance $r = a$ from the beam axis and the angle $\theta = 0$

$$+\frac{V_0}{2} = A_0 a^2 + A_{10} I_0(ka). \quad (2.38)$$

for the vertical vane tip ($\theta = \pi/2$) the displacement $r = m \cdot a$

$$-\frac{V_0}{2} = A_0 (ma)^2 + A_{10} I_0(kma). \quad (2.39)$$

Solving equations 2.38 and 2.39 for A_0 and A_{10} leads to

$$A_0 = \frac{V_0}{2a^2} \frac{I_0(ka) + I_0(kma)}{m^2 I_0(ka) + I_0(kma)}, \quad (2.40)$$

and

$$A_{10} = \frac{V_0}{2} \frac{m^2 - 1}{m^2 I_0(ka) + I_0(kma)}. \quad (2.41)$$

Now, two dimensionless constants can be defined:

$$\chi = \frac{I_0(ka) + I_0(kma)}{m^2 I_0(ka) + I_0(kma)} \quad (2.42)$$

$$A = \frac{m^2 - 1}{m^2 I_0(ka) + I_0(kma)} \quad (2.43)$$

These constants correspond to the old ones

$$A_0 = \chi \cdot \frac{V_0}{2a^2} \quad (2.44)$$

$$A_{10} = A \cdot \frac{V_0}{2}. \quad (2.45)$$

The full time dependent two term potential can now be written

$$\Psi = \frac{V_0}{2} \left[\chi \frac{r^2}{a^2} \cos(2\theta) + AI_0(kr) \cos(kz) \right] \sin(\omega t + \phi) \quad (2.46)$$

Substituting $x = r \cos \theta$ and $y = r \sin \theta$ the two term potential in Cartesian coordinates is found

$$\Psi = \frac{V_0}{2} \left[\chi \frac{x^2 - y^2}{a^2} + AI_0(kr) \cos(kz) \right] \sin(\omega t + \phi). \quad (2.47)$$

For the beam dynamic simulation the components of the electric field have to be known and not the scalar potential. The field can be found by taken the partial derivative of the potential. Doing so, the components of the electric field in cylindric coordinates are:

$$E_r(r, \theta, z) = -\frac{\partial \Phi}{\partial r} = -\frac{\chi V_0 r}{a^2} \cos(2\theta) - \frac{V_0 A k}{2} I_1(kr) \cos(kz) \quad (2.48)$$

$$E_\theta(r, \theta, z) = -\frac{1}{r} \frac{\partial \Phi}{\partial \theta} = \frac{\chi V_0 r}{a^2} \sin(2\theta) \quad (2.49)$$

$$E_z(r, \theta, z) = -\frac{\partial \Phi}{\partial z} = \frac{AV_0 k}{2} I_0(kr) \sin(kz), \quad (2.50)$$

The time dependency is of course sinusoidal again ($\sin(\omega t + \phi)$). The first term of equation (2.48) describes the quadrupole focusing whose strength depends on the term $\frac{V_0 \chi}{a^2}$. The second term of the same equation corresponds to the RF defocusing, which occurs when a longitudinal field component is introduced. If the electrodes have no modulation ($A(m=1) = 0$) this term vanishes. In the course of the structure when the modulation increases, the RF defocusing increases as well and the quadrupole strength ($\sim \chi$) decreases. This leads to the assumption that the two parameters χ and A are coupled. The equation

$$A = 1 - \chi \cdot I_0(ka). \quad (2.51)$$

shows this coupling. Again, this means that the sum of the focusing strength and the accelerator factor is equal to a constant and therefore an accelerating force always results in a smaller transverse focusing. Consequently, the modulation has an upper limit, when the transverse focussing of the RFQ becomes too small. To accelerate ions to higher energies the modulation can be held constant at some practical value from a certain point on. With higher energies the velocity of the particles increase and therefore the cells get longer and achieving the longitudinal field becomes inefficient leading to high RF power consumption. Therefore an RFQ structure is not suitable to accelerate ions to very high beam energies.

The components of the electric field can also be expressed in Cartesian coordinates [Wan98]

$$E_x = -\frac{\chi V_0}{a^2}x - \frac{kAV_0}{2}I_1(kr)\frac{x}{r}\cos(kz) \quad (2.52)$$

$$E_y = \frac{\chi V_0}{a^2}y - \frac{kAV_0}{2}I_1(kr)\frac{y}{r}\cos(kz) \quad (2.53)$$

$$E_z = \frac{kV_0A}{2}I_0(kr)\sin(kz). \quad (2.54)$$

With

$$\mathbf{F} = q\mathbf{E} \quad (2.55)$$

and the equation of motion of particles traveling through an RFQ can be formed

$$\ddot{x} + x\frac{q}{m}\left(\frac{XV_0}{a^2}x + \frac{kAV_0}{2}I_1(kr)\frac{x}{r}\cos(kz)\right)\sin(\omega t - \phi) = 0 \quad (2.56)$$

$$\ddot{y} + y\frac{q}{m}\left(-\frac{XV_0}{a^2}x + \frac{kAV_0}{2}I_1(kr)\frac{x}{r}\cos(kz)\right)\sin(\omega t - \phi) = 0 \quad (2.57)$$

$$\ddot{z} - \frac{kV_0A}{2}I_0(kr)\sin(kz)\sin(\omega t - \phi) = 0. \quad (2.58)$$

For a further analysis the modified Bessel functions are approximated by $I_0(kr) \approx 1$ and $I_1(kr) \approx kr/2$. One obtains for the transverse equation of motion

$$\ddot{x} + x\left(\frac{qXV_0}{ma^2} + \frac{qk^2AV_0}{4m}\cos(kz)\right)\sin(\omega t + \phi) = 0. \quad (2.59)$$

The longitudinal coordinate of the particles can be expressed by $kz = \omega t$. Doing so the second term of equation 2.59, which describes the RF defocussing, depends on

$\cos(kz) \sin(kz - \phi)$. This can be averaged over one cell length $l = \frac{\beta\lambda}{2}$

$$\frac{2}{\beta\lambda} \int_0^{\beta\lambda/2} \cos(kz) \sin(kz - \phi) dz = -\frac{2}{\beta\lambda} \sin(\phi) \int_0^{\beta\lambda/2} \cos^2(kz) dz \approx -\frac{1}{2} \sin \phi. \quad (2.60)$$

Replacing the independent variable t by the dimensionless variable $\tau = 1/2(\omega t - \phi)$ one finds that the transverse equation of motion is the well known Mathieu's Equation:

$$\frac{\partial^2 x}{\partial \tau^2} + (\Delta_{RF} + B \sin 2\tau) x = 0 \quad (2.61)$$

with:

$$\Delta_{RF} = \frac{qAV_0 \sin \phi}{2mc^2 \beta^2} \quad (2.62)$$

$$B = \frac{2q\chi V_0}{ma^2 \omega^2}, \quad (2.63)$$

where Δ_{RF} is the RF defocussing factor, and B is the transverse focussing factor. In fact, B is a more frequently used physical quantity than the focussing efficiency χ . β is the relativistic velocity of the particle. Δ_{RF} is proportional to the frequency and A (acceleration efficiency). B is proportional to the applied voltage and to the reciprocal aperture square ($\propto \frac{V}{a^2}$). For a strong transverse focusing a small aperture and a high voltage at the sparking limit is chosen. Since $\sin \phi < 0$ for longitudinal stability, the RF defocussing factor is normally $\Delta_{RF} < 0$ increasing the divergence of a particle away from the beam axis [Sta90]. In order to keep the transverse motion of the particles stable, the parameters of the RFQ need to be chosen in such a manner that the solution of the Mathieu's differential equation is within the stable region [Zha05].

For the longitudinal equation of motion one finds

$$\frac{\partial^2 z}{\partial \tau^2} - 2Bz = 0 \quad (2.64)$$

The particles perform longitudinally a simple oscillation about a synchronous particle. This oscillation is demonstrated in Figure 2.10. When a particle is ahead of the synchronous particle, it arrives earlier at the cell center when the RF field has not yet its full value, so it is exposed to a weaker field than the synchronous particle and will be less accelerated. Consequently it falls back to the synchronous particle. A particle which arrives at the center of a cell after the synchronous particle will see a bigger

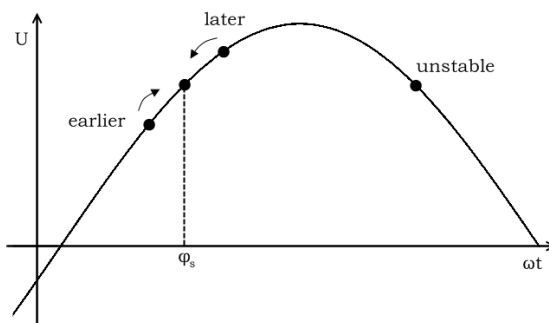


Figure 2.10: Longitudinal phase focussing.

field and will therefore catch up to the synchronous particle. Particles having a phase difference more than a certain value, can not be brought back to the synchronous particle and will therefore leave the bucket.

The oscillation of the particle around a synchronous particle in both transverse and longitudinal plane can be expressed by phase advances (per RF period or per another unit length, such as meters or cell length). These quantities give information of how much the phase relative to the synchronous particle change over one unit length [YJL⁺06]. For zero current and unit length of one RF period, they are defined by

$$\sigma_{t0}^2 = \Delta_{RF} + \frac{B^2}{8\pi} \quad (2.65)$$

$$\sigma_{l0}^2 = -2\Delta_{RF}. \quad (2.66)$$

When considering a beam with non neglectable current the phase advances are damped by a space charge term as follows

$$\sigma_t^2 = \Delta_{RF} + \frac{B^2}{8\pi} - \frac{I\lambda^3(1 - ff)}{a^3b\gamma^3}k \quad (2.67)$$

$$\sigma_l^2 = -2\Delta_{RF} - \frac{2I\lambda^3ff}{a^3b\gamma^3}k, \quad (2.68)$$

where a and b are transverse and longitudinal rms beam radii respectively, λ is the RF wavelength, I is the beam current, ff is the ellipsoid form factor, γ and β are the relativistic gamma and beta, and $k = \frac{3 \cdot 10^{-6} z_0 q}{8\pi m_0 c^2}$ with $z_0 = 376.73\Omega$ [LJDK96].

An example of a program using the two term potential is RFQSIM based on early PARMTEQ-versions maintained at IAP which has the advantage that applications like funneling and deceleration can be simulated [Thi07], [Dei87].

Eight Term Potential

The usefulness of the 2-term potential is limited by practical machining considerations for some cell geometries. It is also easier to machine a sinusoidal longitudinal profile instead of Bessel function profile, and this profile has also the advantage of a somewhat higher accelerating gradient. Therefore a more practical vane shape has commonly been adopted, as shown in Figure 2.11 (circular vane tip, sinusoidal longitudinal modulation). Eight terms of Equation 2.36 are used to approximate the

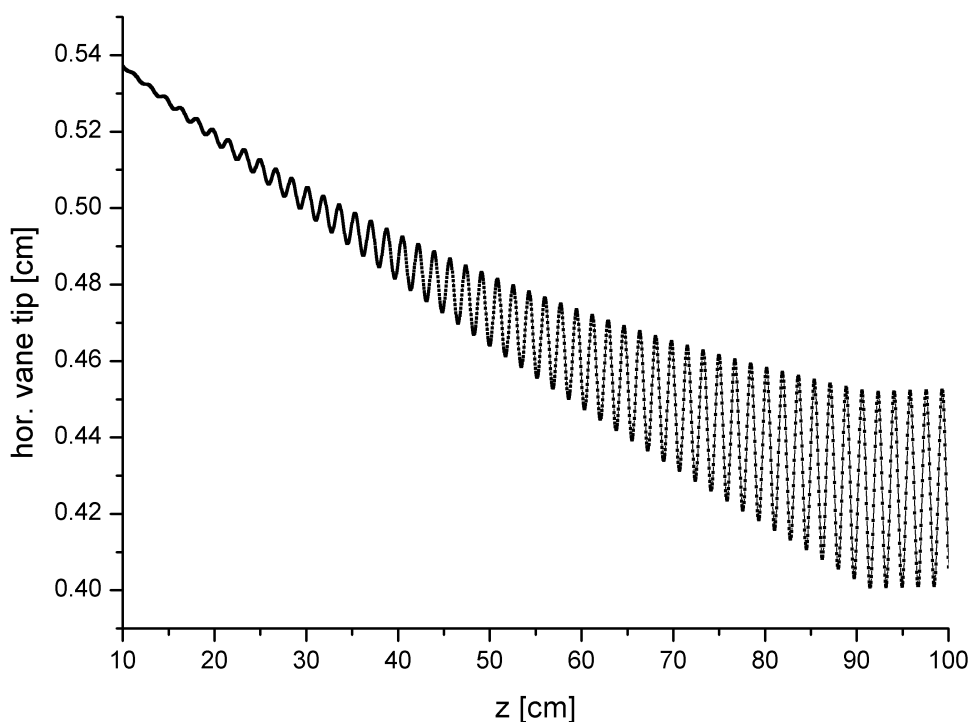


Figure 2.11: Example of the evolution of the position of a vane tip (the beam velocity is not changing in this section).

central region fields. In PARMTEQM the multipole coefficients are interpolated from data files, which contain coefficients for different cell configurations. They have been calculated following

$$A_{nm} = \frac{16}{\pi V I_{2m}(nka) L_c} \int_0^{\pi/2} \int_0^{L_c} U(a, \theta, z) \cos(2m\theta) \cos(nkz) d\theta dz, \quad (2.69)$$

where $U(a, \theta, z)$ is the numerical solution of the potential found by Poisson solver (CHARGE 3D in case of PARMTEQM) [Dup00]. The integration path is a cylinder with the radius of the minimum aperture around the beam axis and a length of the cell length. Therefore the eight term multipole expansion is only accurate in this region and gives imprecise values beyond the cylinder.

Limitations of the Multipole Representation

The accuracy of the representation is (strictly) limited to the radial region less than the minimum aperture a as shown in Figure 2.12, by the cylindrical symmetry of Equation 2.36. Figure 2.13 shows the difference between the field calculated from

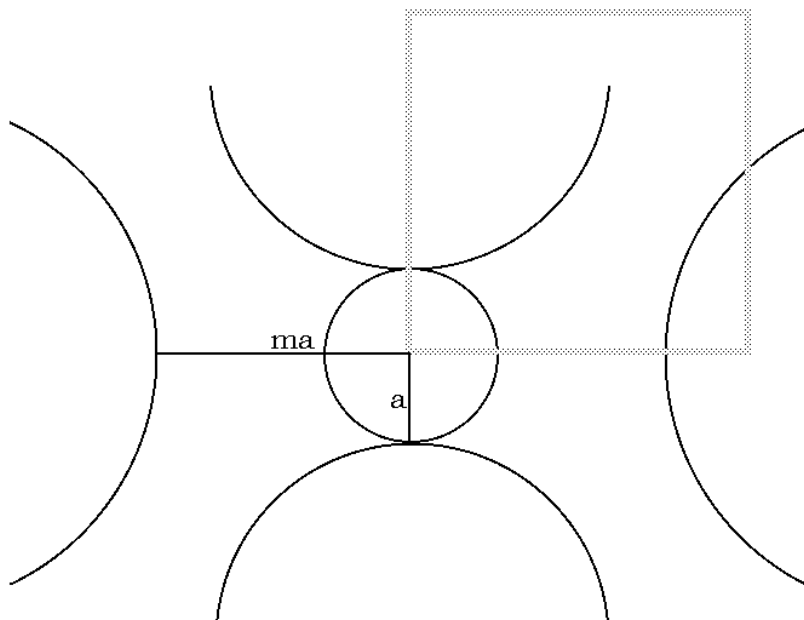
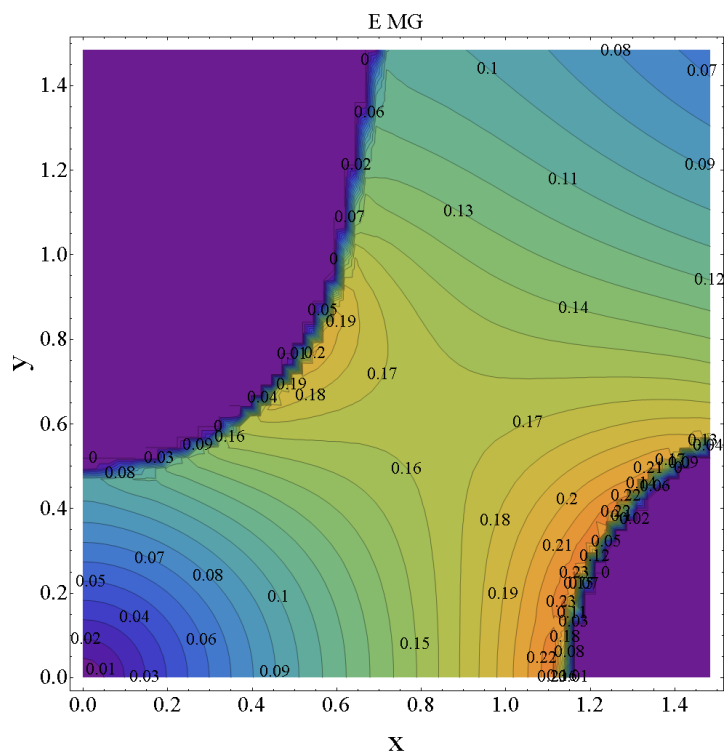
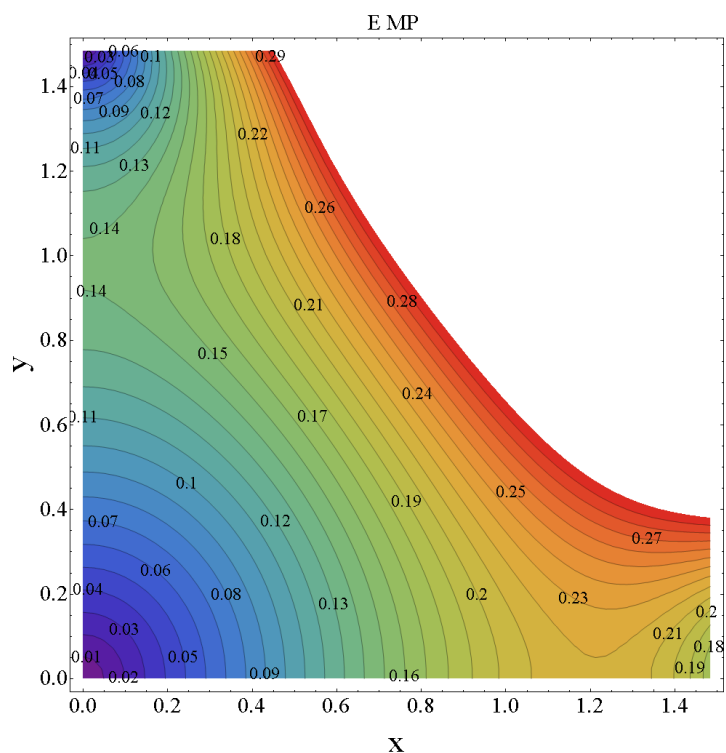


Figure 2.12: Accurate region of the eight term multipole expansion is only with a circle with the radius of the minimum aperture a around the beam axis. The modulation $m = 3$.

the eight term multipole representation and from a numerical solution of the Laplace equation for a typical vane shape. The large error in the region between a and ma , where particles that might tend to be lost would travel, prompted the development of the Poisson/Laplace solver of this thesis. The Poisson solver is now feasible because of the computing power available with modern computers.



(a) Absolute electric field from multigrid Poisson solver



(b) Absolute electric field from multipole expansion method

Figure 2.13: Fields from eight term multipole expansion and multigrid Poisson solver at the dashed area in Figure 2.12.

3 Poisson Solver

For accurate beam dynamic simulation, the electric field of the useful region inside the RFQ has to be known. Therefore the Poisson equation (2.12) as described in chapter 2 has to be solved. One method which can be used to solve the Poisson equation is the finite difference method. The differential equation is discretized on a suitable grid (or mesh). The simplest type of grid for calculation of the field inside an RFQ is an isotropic Cartesian grid in 3D. Generally, it is not necessary to have the same grid spacing in the longitudinal and in the transverse plane, so an anisotropic Cartesian grid would be a reasonable choice. An anisotropic grid has the disadvantage that the Poisson solver becomes more complex (and slower).

The general notation of the Poisson equation with boundary conditions is

$$\begin{aligned} L^\Omega u(\mathbf{x}) &= f^\Omega(\mathbf{x}) \quad (\mathbf{x} \in \Omega) \\ L^\Gamma u(\mathbf{x}) &= f^\Gamma(\mathbf{x}) \quad (\mathbf{x} \in \Gamma := \partial\Omega) , \end{aligned} \quad (3.1)$$

where u donates the potential, $\mathbf{x} = (x, y, z) \in \Omega$ in our case, L^Ω is a linear differential operator on some domain $\Omega \subset \mathbb{R}^3$ and L^Γ ($\Gamma := \partial\Omega$) is a boundary operator. f^Ω and f^Γ are the given source functions (charge density) of the Poisson equation. In short, equation 3.1 will be written as

$$Lu = f \quad (3.2)$$

For the 3D case it can again be rewritten as

$$\begin{aligned} \frac{\partial^2 u}{\partial x^2} + \frac{\partial^2 u}{\partial y^2} + \frac{\partial^2 u}{\partial z^2} &= f \quad (3.3) \\ \frac{u_{i+1} - 2u + u_{i-1}}{\Delta x^2} + \frac{u_{j+1} - 2u + u_{j-1}}{\Delta y^2} + \frac{u_{k+1} - 2u + u_{k-1}}{\Delta z^2} &= f \end{aligned}$$

This can be solved for u and with $\alpha = \frac{\Delta z}{\Delta x}$ and $\beta = \frac{\Delta z}{\Delta y}$ and $r = \frac{f}{\Delta z^2}$.

$$u_{ijk} = \frac{1}{2(1 + \alpha^2 + \beta^2)} (\alpha^2(u_{i+1} + u_{i-1}) + \beta^2(u_{j+1} + u_{j-1}) + u_{k+1} + u_{k-1} - r)$$

So the value for one grid point can be expressed by the values of its surrounding points. With this method only the next neighbor points will be considered. A more complex stencil would take more grid points into account (e.g. four in each direction). The simplest finite difference method is the Jacobi iteration solver where new values are calculated for all grid points using the old values.

$$\begin{aligned} z_{ijk}^{m+1} &= \frac{1}{2(1 + \alpha^2 + \beta^2)} (\alpha^2(u_{i+1}^m + u_{i-1}^m) + \beta^2(u_{j+1}^m + u_{j-1}^m) + u_{k+1}^m + u_{k-1}^m - r) \\ u^{m+1} &= z_{ijk}^{m+1} \end{aligned}$$

where m refers to the m -th iteration and u^m to the old approximation and u^{m+1} to the new approximation. With this schema every grid point becomes recalculated after one another.

By introducing a relaxation parameter ω this simple iteration method can be generalized:

$$u^{m+1} = u^m + \omega(z_{ijk}^{m+1} - u^m) \quad (3.4)$$

This is often referred to the ω -damped Jacobi relaxation (ω -JAC). For $\omega = 1$, the ω -JAC and the Jacobi iteration correspond.

A second type of iterative solver is the Gauss-Seidel method which uses the value of the new grid point as soon as it is calculated

$$z_{ijk}^{m+1} = \frac{1}{2(1 + \beta^2\gamma^2)} (\alpha^2(u_{i+1}^m + u_{i-1}^{m+1}) + \beta^2(u_{j+1}^m + u_{j-1}^{m+1}) + u_{k+1}^m + u_{k-1}^{m+1} - r).$$

A good choice for the overrelaxation parameter ω will lead to a good reduction of the error and therefore a good convergence rate. The following characteristic of either one of the two solvers is very important for the multigrid idea: After applying a few iteration steps, the error of the approximation does not necessary become much smaller, but it becomes smooth. The smoothing capability of the solver is equivalent to the reduction of the high frequency part of the error of the approximation. The

low frequency part of the error is much more difficult to reduce. This is illustrated in Figure 3.1. The initial values are randomly spread between 0 and 1. After a few cycles the high frequencies are damped and only low frequency variations on the grid remain. The smoothing factor of the iterative smoother strongly depends on the overrelaxation parameter ω . A good choice for ω is between 0.8 and 1.

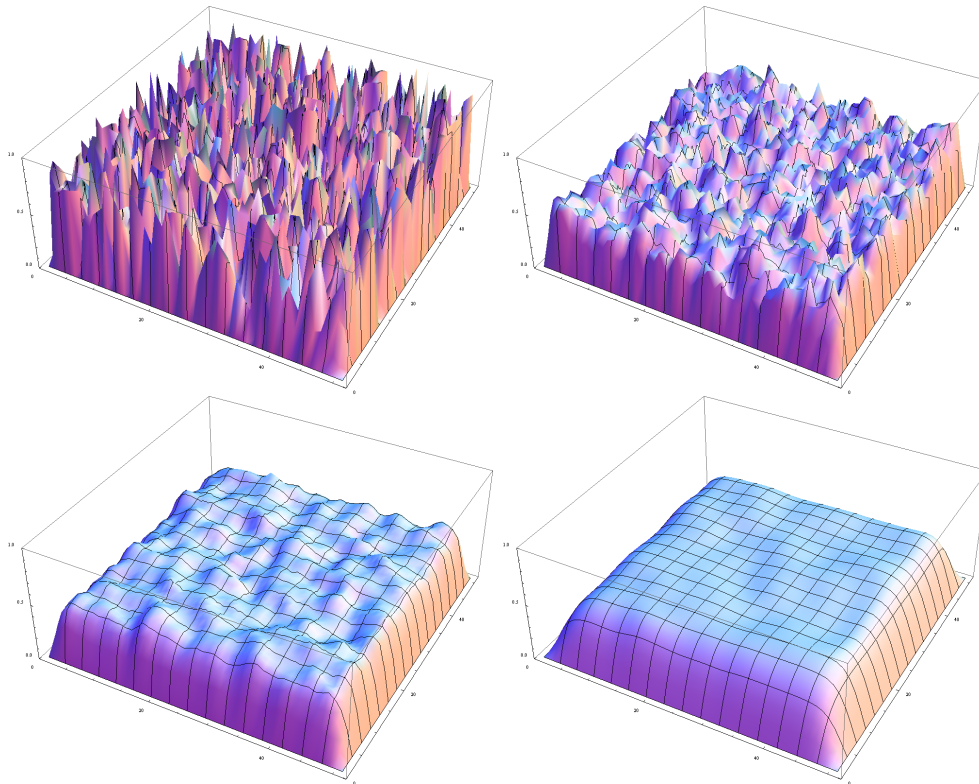


Figure 3.1: Initial values and approximation after 1, 3, and 10 cycles. The high frequency components are sufficiently reduced, whereas the low frequency components remain.

3.1 Multigrid Solver

A classical reference on Poisson equation solution by grid methods is Hockney [HE88]. The best modern method is to use multiple grids - the multigrid method - as presented in [TOS01], which includes a good summary of how the multigrid method absorbs and extends the earlier methods.

The first concept of the multigrid idea is that an iterative solver such as the Gauss-Seidel solver smoothes the error of an approximation within a few iterations and

can therefore be used as a smoother. The second concept is the so called coarse grid principle [TOS01]: If an error is well smoothed it can be approximated on a (much) coarser grid without losing information. The low frequency components of the fine grid are transferred to high frequency components on the coarse grid. The error can be further reduced on the coarser grid with less computational effort, since the number of grid points is reduced.

The error v_h^m of an approximation u_h^m of the solution u is defined by

$$v_h^m := u - u_h^m \quad (3.5)$$

and can generally be expressed by an Fourier expansion

$$v_h^m(\mathbf{x}) = \sum_{i,j,k=1}^{n-1} \alpha_{i,j,k} \sin(i\pi x) \sin(j\pi y) \sin(k\pi z) \quad (3.6)$$

The error can not be calculated directly, since the solution u of the Poisson equation is not known at any time. Therefore it is useful to define the defect or residual of the approximation u_h^m by

$$d_h^m := f_h - L_h u_h^m. \quad (3.7)$$

The defect is a measure of how much the Laplacian of a given approximation differs from the source term of the Poisson equation. It can therefore be used to determine the quality of the solver and its ability to converge. The defect equation

$$L_h v_h^m = d_h^m \quad (3.8)$$

is equivalent to the definition of the error

$$u = u_h^m + v_h^m. \quad (3.9)$$

The discrete eigenfunctions of the discrete Laplace operator L_h are

$$\varphi_{i,j,k}(\mathbf{x}) = \sin(i\pi x) \sin(j\pi y) \sin(k\pi z) \quad (i, j, k = 1, \dots, n-1). \quad (3.10)$$

$\varphi_{i,j,k}(\mathbf{x})$ can be split into two components: one high frequency part, which means that $n/2 \leq \max(i, j, k) < n$ and one low frequency part for $\max(i, j, k) < n/2$, where n is the number of grid points per direction. Equation 3.6 can now be written as

$$v(\mathbf{x}) = \sum_{i,j,k=1}^{n-1} \alpha_{i,j,k} \varphi^{i,j,k}(\mathbf{x}) = \sum_{n/2 \leq \max(i,j,k)}^{n-1} \alpha_{i,j,k} \varphi^{i,j,k}(\mathbf{x}) + \sum_{i,j,k=1}^{n/2-1} \alpha_{i,j,k} \varphi^{i,j,k}(\mathbf{x}) \quad (3.11)$$

The ability of the smoother to smooth the error within a few iterations means that the high frequency components of error are reduced, whereas the low frequency components remain comparably unchanged.

Assume that we have two isotropic grids one with a grid spacing of h (Ω_h) and one with $2 \cdot h$ (Ω_{2h}). The low frequencies on Ω_h are also visible on Ω_{2h} and coincide with high frequencies. Whereas the high frequencies on Ω_h vanish on Ω_{2h} (Figure 3.2). This means that the low frequency part of the error on Ω_h , which can not be damped easily with a Gauss-Seidel smoother for example, can be converted to a high frequency error on Ω_{2h} . The high frequency error can then be damped easily using one of the described smoothers. This is the basic concept of a multigrid solver (2 grid) [TOS01].

3.2 Ingredients of Multigrid Cycles

Generally, a multigrid iteration starts on the finest grid Ω_h by applying some smoothing cycles to the approximation u_h^m to reduce the high frequency error. Then the defect d_h^m is calculated by equation 3.7 and restricted to the coarser grid by a restriction schema (d_{2h}^m). The equation

$$L_{2h} \tilde{v}_{2h}^m = d_{2h}^m \quad (3.12)$$

has to be solved on Ω_{2h} , where L_{2h} is the corresponding Laplacian on Ω_{2h} . This can be either done recursively with another multigrid approach since equation 3.12 has the same form than the initial Poisson equation, or by a fast iterative solver. The defect equation 3.12 does not need to be solved exactly. A suitable approximation \tilde{v}_{2h}^m will work as well without essential loss of convergence speed [TOS01]. After \tilde{v}_{2h}^m is computed it will be interpolated to the fine grid \tilde{v}_h (Ω_h) and the new approximation is found by

$$u_h^{m+1} = u_h^m + \tilde{v}_h^m. \quad (3.13)$$

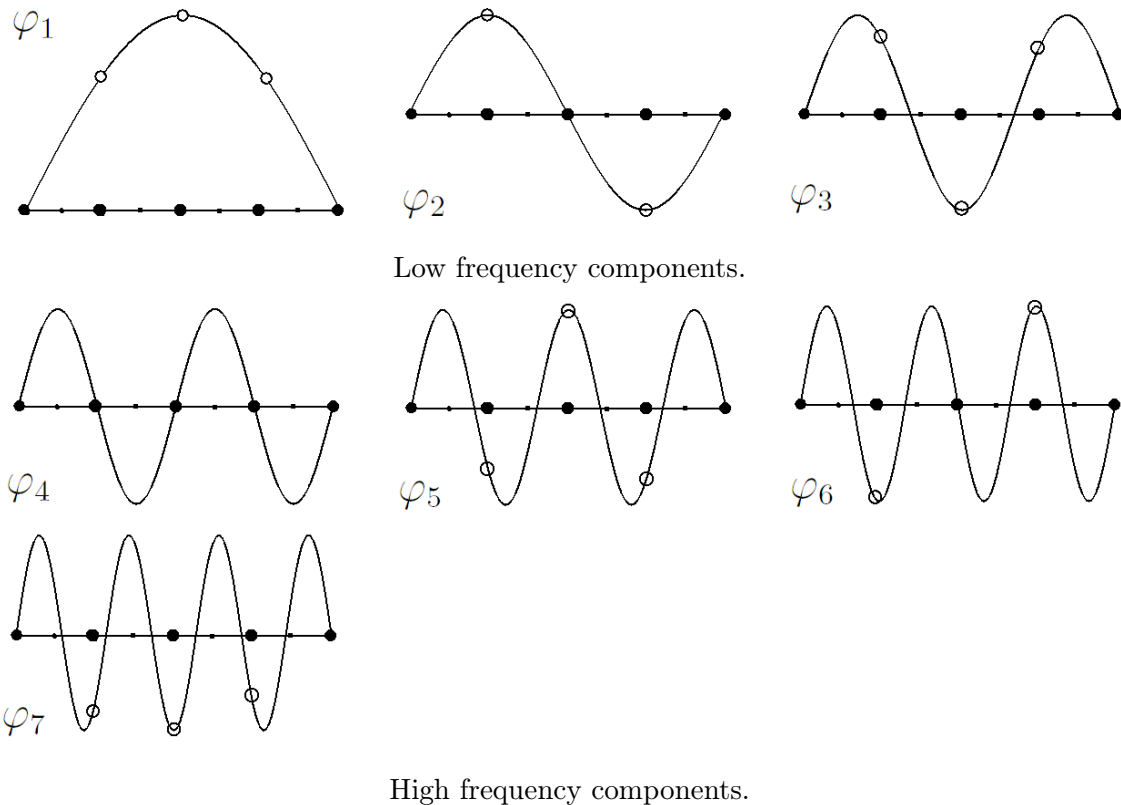


Figure 3.2: Low and high frequency components of the error on a grid Ω_{2h} \bullet for a simple 1D example. Low frequency components are visible on Ω_{2h} (first row), whereas high frequency cannot be represented.

Finally, some postsmoothing steps will be performed to u_h^{m+1} . In the following, different structures of one multigrid iteration are discussed consisting of four grids. For more or less grids similar structures are feasible. All structures start on the finest grid and perform ν_1 cycles to smooth the approximation u_h^m . Then the defect is restricted to the next coarser grid where again ν_1 smoothing cycles are performed. This procedure is repeated until the coarsest grid is reached. This grid is solved using an iterative solver. From this point, the different cycle schema then differ from each other. The V-cycle illustrated on Figure 3.3 solves the coarsest grid once and prolongates then back stepwise to the finest grid performing ν_2 smoothing cycles on the error of every grid level. The W-cycle shown on Figure 3.4 is a more complicated structure. The coarsest grid is now solved more than once and the computational effect for one full W-cycle is higher than for one V-cycle, but the defect will be reduced stronger than by one V-cycle iteration. So the total time versus reduction of the defect might be better for the W-cycle. A last type of multigrid structure is the F-cycle shown in Figure

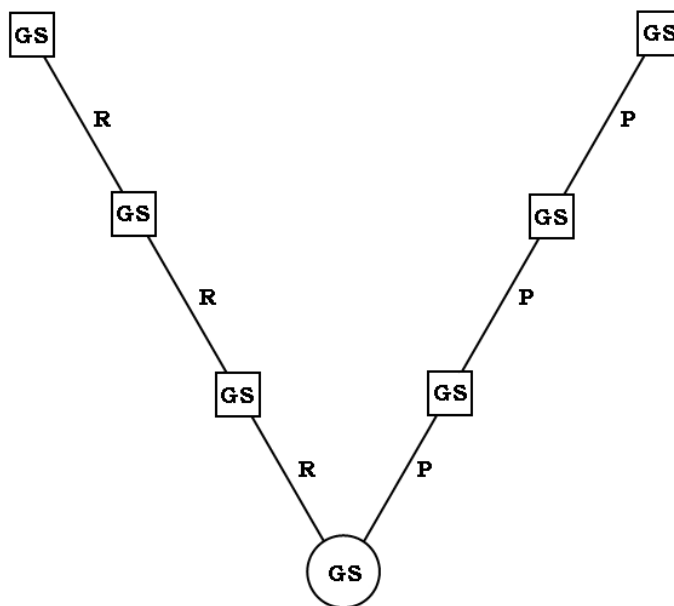


Figure 3.3: V-cycle.

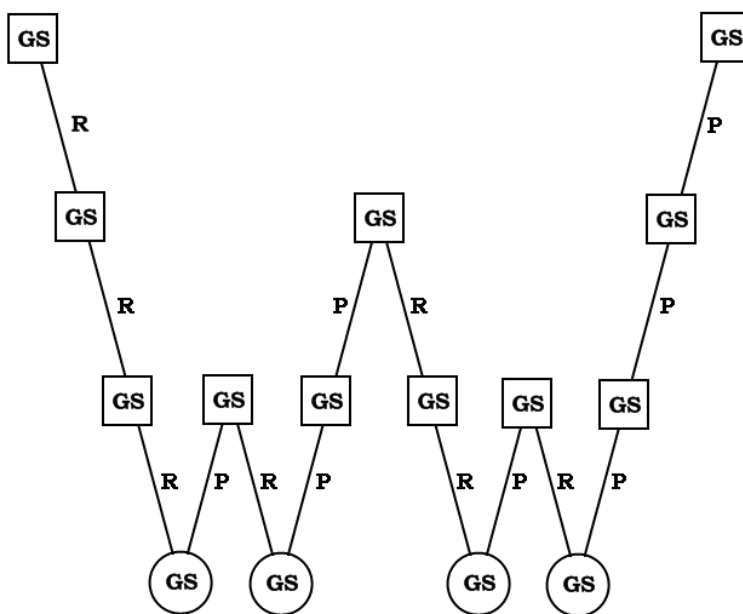


Figure 3.4: W-cycle.

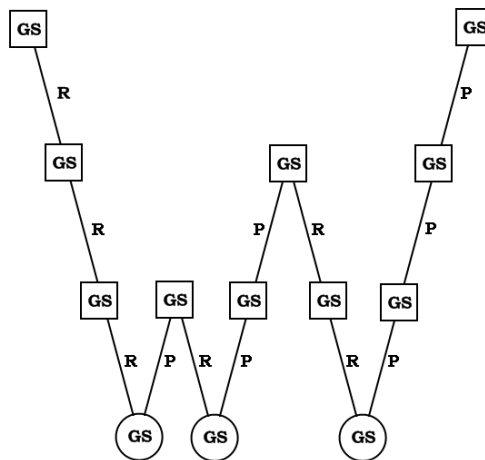


Figure 3.5: F-cycle.

3.5. It strongly depends on the type of problem, which multigrid structure and which values for ν_1 and ν_2 result in a effective solver.

3.2.1 Restriction Operator

The purpose of the restriction operator I_h^{2h} is to map grid functions on Ω_h to grid functions on Ω_{2h} . The simplest restriction operator is the injection operator that connects coinciding grid points directly. Grid points on Ω_h which vanish on Ω_{2h} will not be considered

$$d_{2h}(x, y, z) = I_h^{2h} d_h(x, y, z) = d_h(x, y, z). \quad (3.14)$$

More complex restriction operators are the half weighting (HW) operator and the full weighting (FW) operator, which assign a combination of the neighbouring points to the center grid point. The HW operator is for example defined by

$$\begin{aligned} d_{2h}(x, y, z) = I_h^{2h} d_h(x, y, z) & \quad (3.15) \\ & \frac{1}{12} [6d_h(x, y, z) \\ & + d_h(x - h, y, z) + d_h(x + h, y, z) \\ & + d_h(x, y - h, z) + d_h(x, y + h, z) \\ & + d_h(x, y, z - h) + d_h(x, y, z + h)] \end{aligned}$$

The choice of the restriction operator depends on the actual problem. So it can not be said in general that any restriction operator is superior. For the case of the field inside an RFQ the injection operator was preferred, because it is most efficient in terms of computation time and reduction of the defect.

3.2.2 Prolongation Operator

The purpose of the prolongation operator I_{2h}^h is to map grid functions on Ω_{2h} to grid functions on Ω_h . This can be done by a trilinear interpolation that is illustrated in Figure 3.6. The prolongation operator is given by

$$I_{2h}^h \tilde{v}_{2h}(x, y, z) = \begin{cases} \tilde{v}_h(x, y, z) & \text{for } \bullet \\ \frac{1}{2} (\tilde{v}_{2h}(x, y, z + h) + \tilde{v}_{2h}(x, y, z - h)) & \text{for } \blacksquare \\ \frac{1}{2} (\tilde{v}_{2h}(x + h, y, z) + \tilde{v}_{2h}(x - h, y, z)) & \text{for } \circ \\ \frac{1}{2} (\tilde{v}_{2h}(x, y + h, z) + \tilde{v}_{2h}(x, y - h, z)) & \text{for } \square \end{cases} \quad (3.16)$$

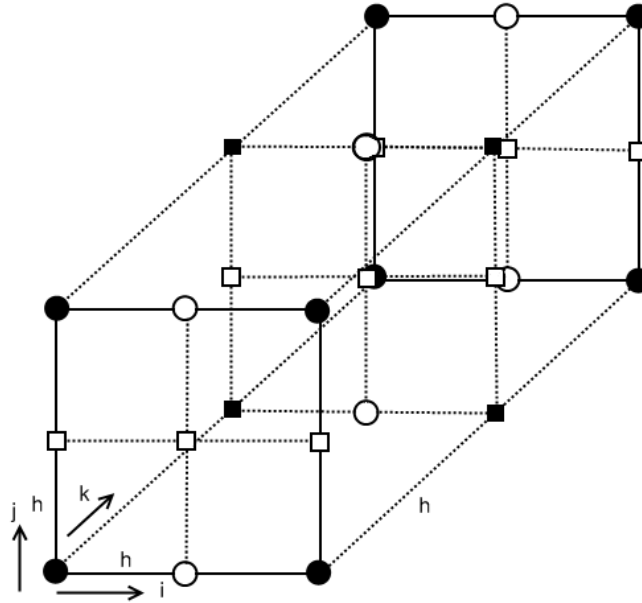


Figure 3.6: Trilinear interpolation in 3D.

4 Verification of the Multigrid Solver

After the main ideas of the multigrid Poisson solver have been illustrated in chapter 3, a verification of the solver will be covered in this chapter. Since the solver will be used to calculate the external field as well as the internal field, two different types of test problems will be considered: one with a charge density introducing the field (leading to Poisson equation) and one without charges, where the field is only generated by the boundary conditions (leading to Laplace equation).

4.1 Examples with no Charges

For the following test problems no charges are placed on the grid. The first test problem is a simple box in three dimensions with potential $\phi = 1$ on its surface and starting values of zero on the grid. The solver should be able to increase the values on the grid to their exact answer of $\phi = 1 \forall \mathbf{x}$. Figure 4.1 shows the initial situation and the potential on the indicated plane after one and three multigrid iterations. It can be seen that the approximation is already within 20% of the exact answer after one iteration. After six iterations the difference is less than 10^{-6} . The oscillations on the right hand side of the box are due to the running direction of the Gauß-Seidel-Smoother, which updates those grid points first, which are closer to the origin. The corresponding defects are shown in Figure 4.2. The absolute values of the defects depend on the grid spacing and are therefore of no interest, instead the change of the magnitude is the important measure. The defect was reduced by a factor of 10^5 within six iterations. The shape of the defect coincides with the approximations minus the solutions which is 1 in this case.

As a second test problem a conducting ball was chosen having zero potential. In its center the potential is forced to be $\phi = 1$. The cut through the initial potential and the approximation of the potential after one and ten multigrid iterations at $z = 0$

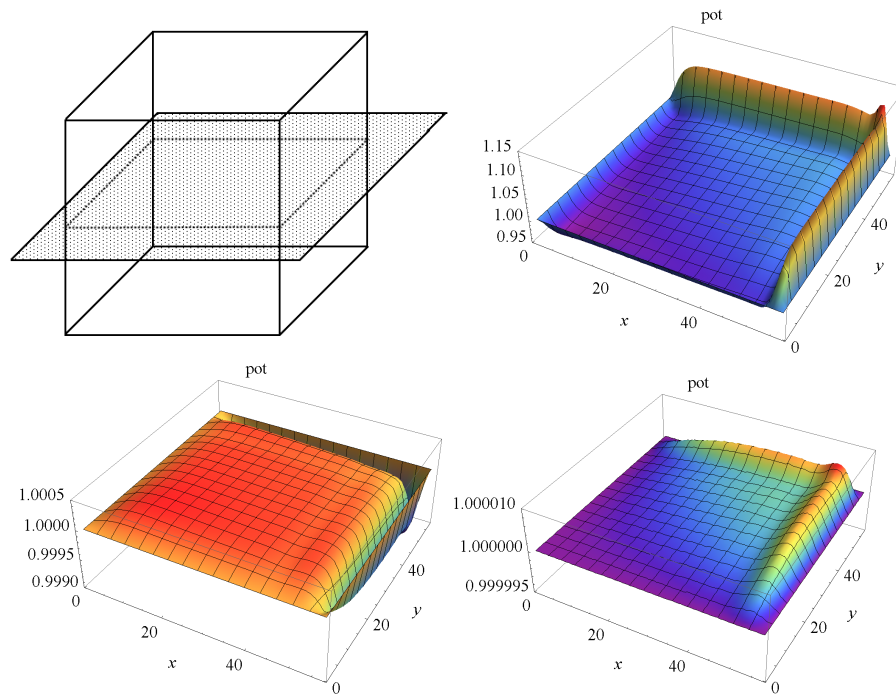


Figure 4.1: Box with $\phi = 1$ on the surface and potentials after 1, 3, and 6 multigrid cycles at the indicated plane.

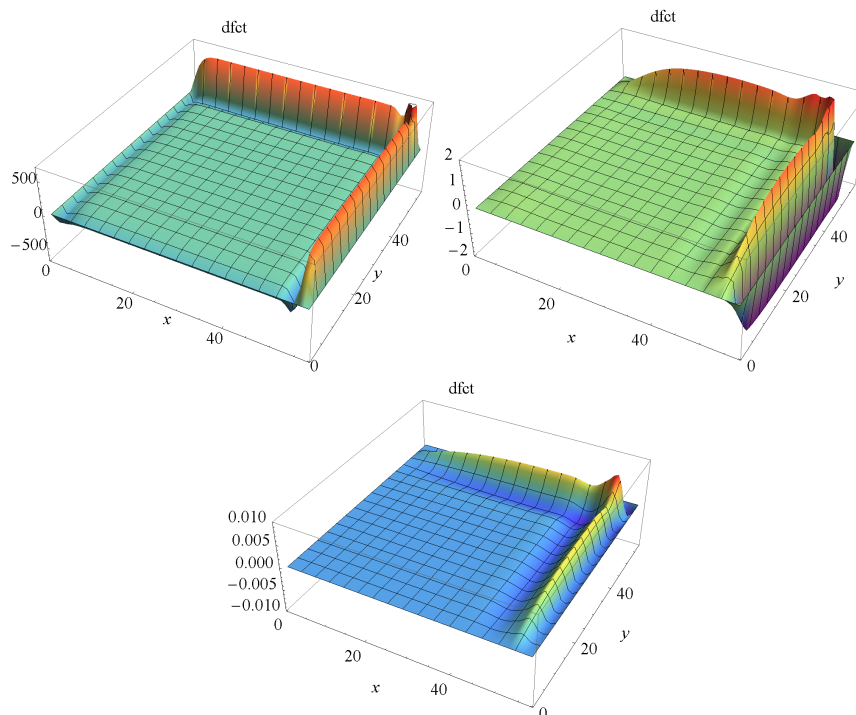


Figure 4.2: Defect after 1, 3, and 6 multigrid iterations of a box with $\phi = 1$ on the surface.

are shown in Figure 4.3. After one iteration the shape of the approximation is already close to the one after ten iterations, so that just minor changes were applied. This demonstrates the advantage of the multigrid method: the ability to reduce the error within a few iterations. The corresponding defects are shown in Figure 4.4. Their

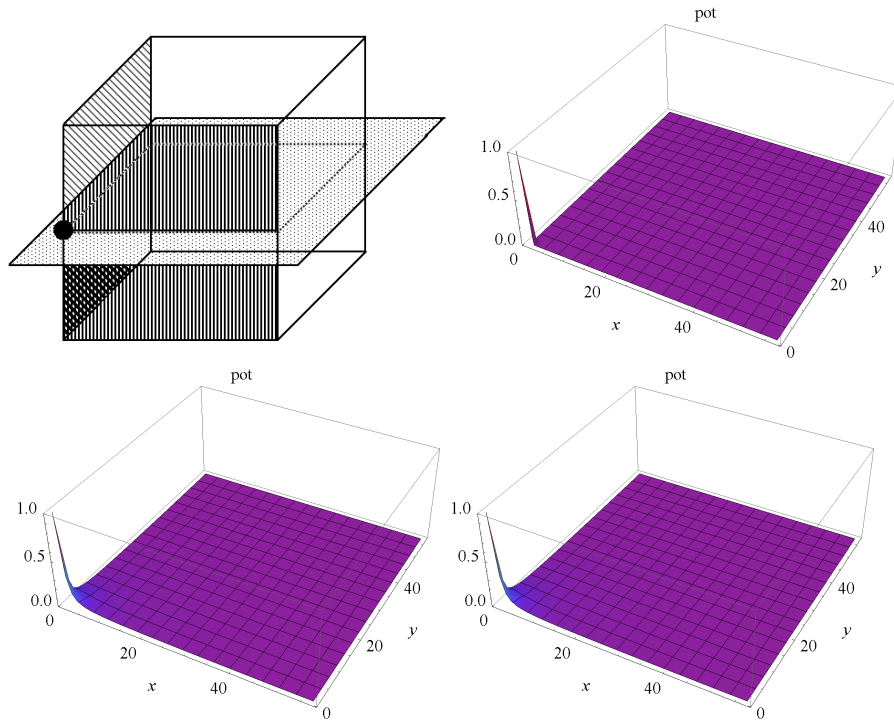


Figure 4.3: Box with charged ball and with vanishing potential on the boundary (the marked boundaries are reflecting ones) and initial potential and potential after 1 and 10 multigrid iterations on the indicated plane

maxima are located around the center where the potential $\phi = 1$ and by the reflecting walls at $x = 0$ and $y = 0$. The defect is reduced by a factor of 10^{12} within 10 iterations.

The last test problem of this kind is a parallel-plate capacitor placed inside a grounded box. The initial potential and the approximations after one and ten multigrid iterations are shown in Figure 4.5. On the initial approximation only the two plates are of opposite potential and the remaining grid points have zero potential. After one iteration the expected shape of the potential was observed. After ten iterations the shape of the approximation has changed a little. This differs when looking at the corresponding defects shown in Figure 4.6. The defect is further reduced after ten iterations by approximately the same factor than in the other test problems mentioned above. If the width of the plate is reduced, convergency of the solver becomes worse.

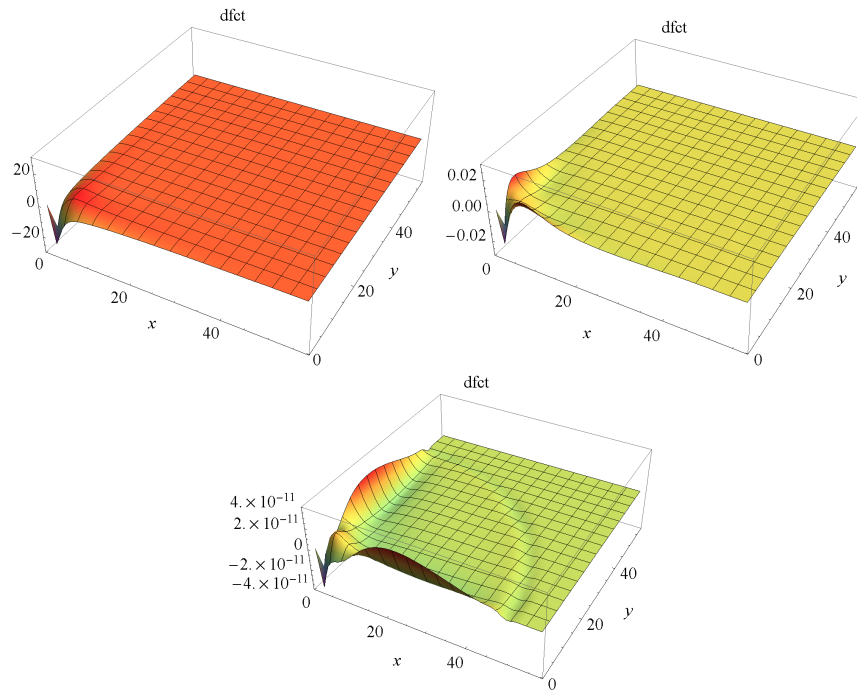


Figure 4.4: Defect after 1, 3, and 10 multigrid iterations of a ball with vanishing potential on the boundary and potential $\phi = 1$ at the center.

This is due to too fine structures on the finest grid, which might vanish on a coarser grid.

4.2 Examples with Charges

This section covers test problems involving nonzero charge densities and zero potential on the boundaries. These type of problems will occur when calculating space charge effects inside the RFQ. The boundaries are then forced to have zero potential, so that effect of image charges is realizable as well. The principle of superposition allows to compute the external and internal fields separately. In most applications a DC beam is injected into the RFQ having the shape of a cylinder two cells long. Further down in the accelerator the beam is bunched and of elliptic shape. It will be surrounded by either the electrodes for the cases considering the image effect or by the cylinder with zero potential and a certain distance to the beam axis for calculations neglecting the image charges.

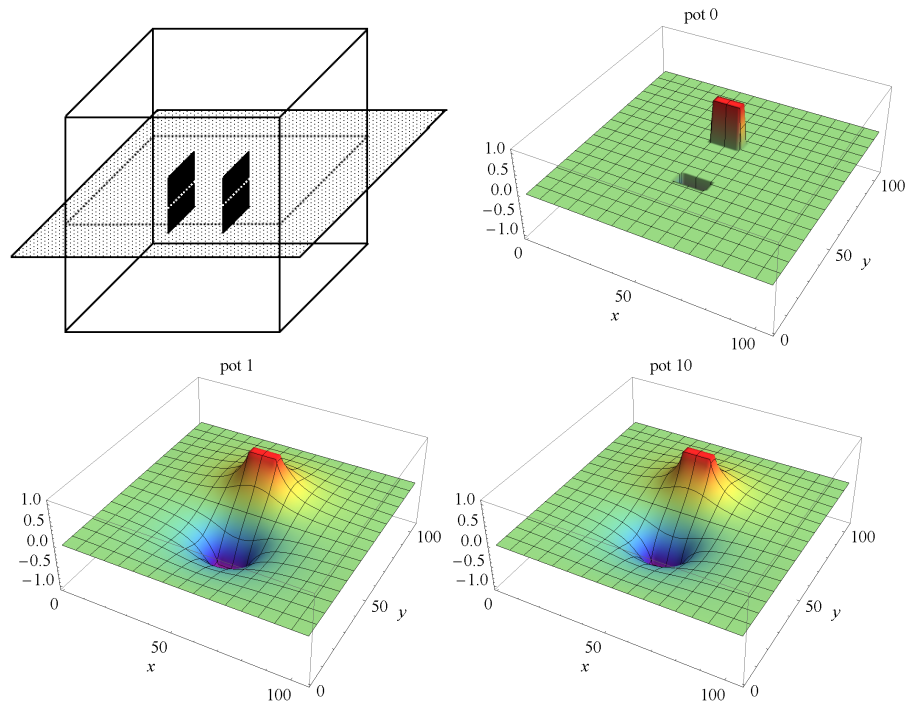


Figure 4.5: Parallel-plate capacitor in a grounded box and initial potential and potential after 1 and 10 multigrid iterations on the indicated plane.

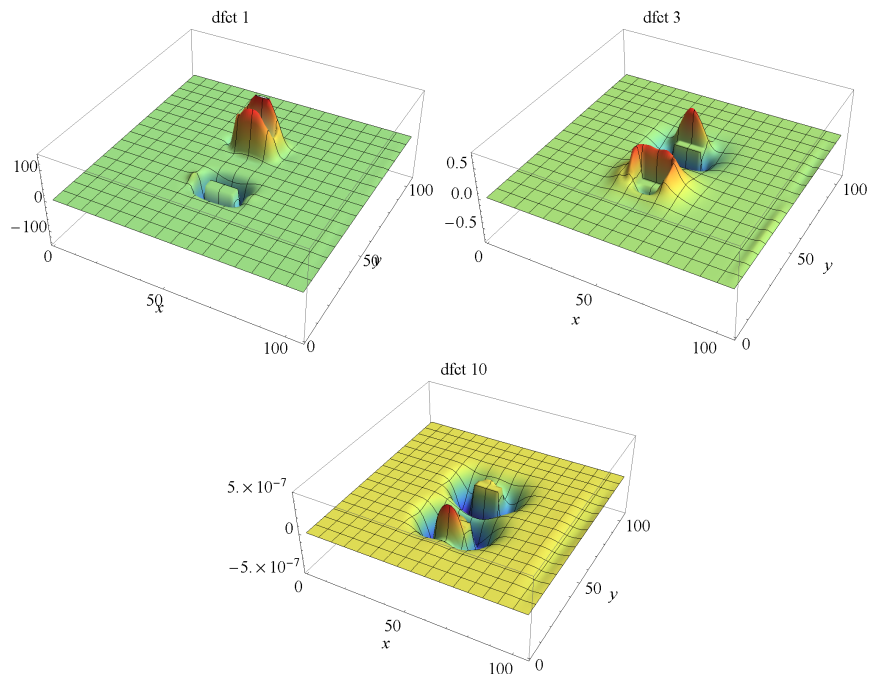


Figure 4.6: Defect after 1, 3, and 10 multigrid iterations of a parallel-plate capacitor in a grounded box.

4.2.1 Examples with no Image Charge Effect

Again, to demonstrate the code, same test problems are described below which have a cylindric boundary with zero potential in which the charges are placed. For space charge simulations in an RFQ the radius of the cylinder needs to be big enough to avoid particles coming too close to the cylinder. Twice the maximum aperture ($2ma$) is normally sufficient.

The first case discussed here is a charge density with the shape of a cylinder placed inside a grounded cylinder. This is the situation of a DC beam injected into the RFQ neglecting the image effect. The ratio of the grounded cylinder radius to the beam radius is 5 to 1. A cut at $y = 0$ of the charge density as well as the approximation of the potential is shown in Figure 4.7 and the corresponding defects are shown in Figure 4.8. The potential has its maximum at the center of the cylinder and falls off to the grounded cylinder. It does not show any longitudinal dependency as expected so that no further steps are necessary to include neighbouring bunches. The defect is reduced by a factor of 10^8 within 10 iterations.

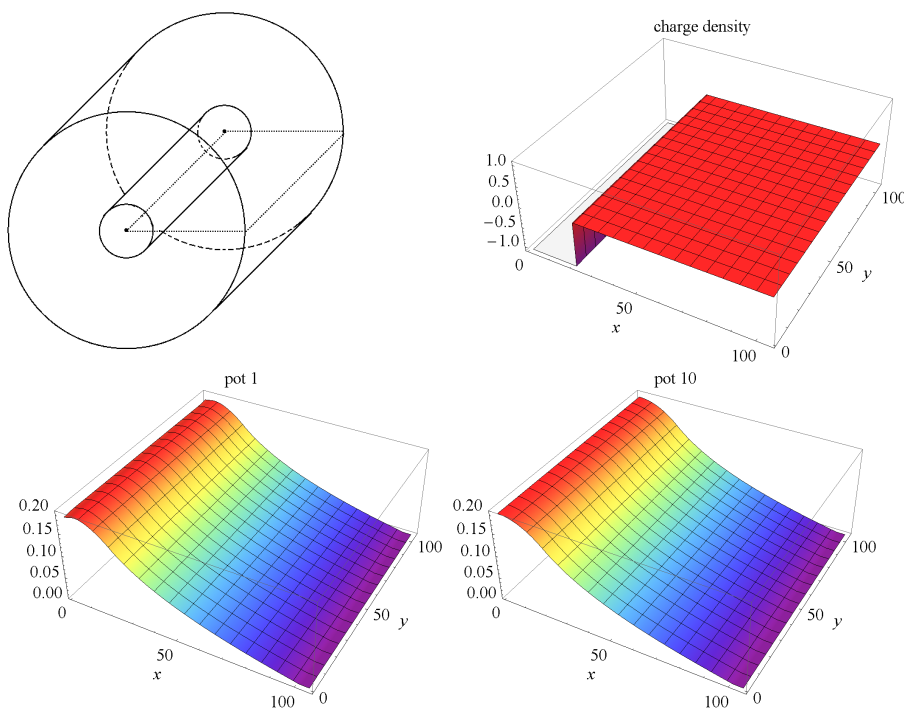


Figure 4.7: Charge cylinder placed inside a grounded cylinder and charge density and approximation of the potential after 1 and 10 multigrid iterations on the indicated plane.

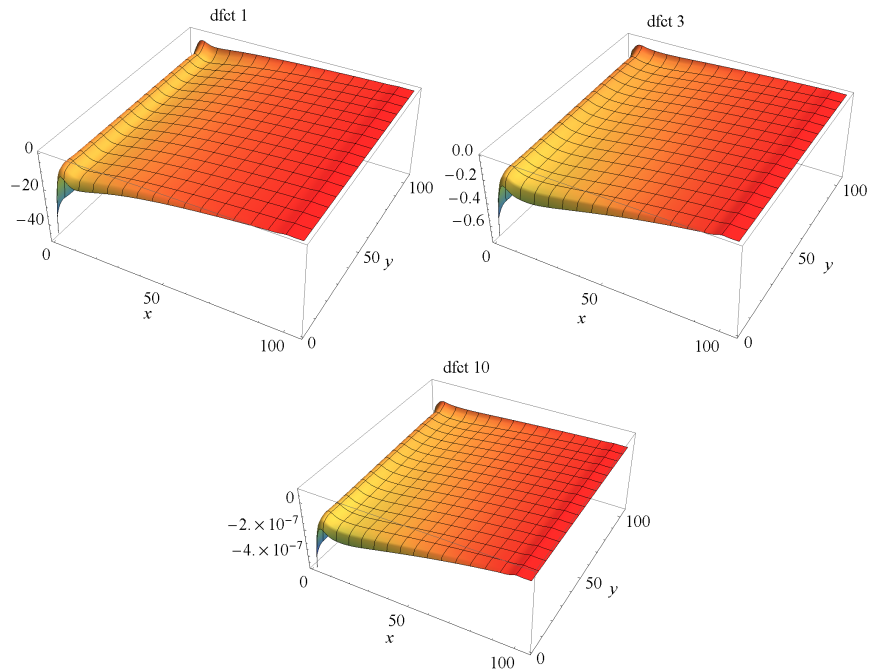


Figure 4.8: Defect after 1, 3 and 10 multigrid iterations of a charge cylinder placed inside a grounded cylinder.

A cut at $y = 0$ of the approximation of the potential as well as of the charge density of a charged ball placed inside a grounded cylinder is shown in Figure 4.9. The grid is periodic in the longitudinal direction, so that neighbouring bunches are fully taken into account. The charged ball has a radius of 20 grid points, and the grounded cylinder radius is 100 grid points. The potential has its maximum at the center of the charged ball and falls off in all directions. In the transverse direction the potential decreases to zero whereas in the longitudinal directions it does not fall down to zero, since the neighbouring charge is taken into account and no conducting boundary is present there. The solver reduces the defects shown in Figure 4.10 strongly by a factor of 10^8 within ten multigrid iterations and is therefore sufficient for computing space charge effects as well. It has to be noted that the maximum of the defect after some iterations is not in the region where the charge is located, but at the edges of the grid where grid points are reflected.

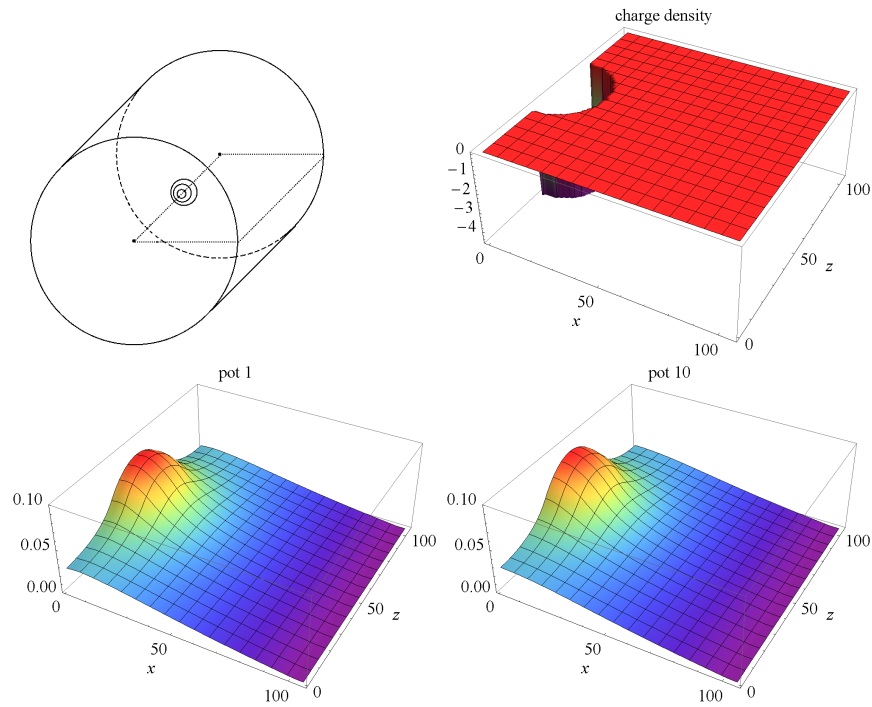


Figure 4.9: Charged ball placed inside a grounded cylinder and charge density and approximation of the potential after 1 and 10 multigrid iterations on the indicated plane.

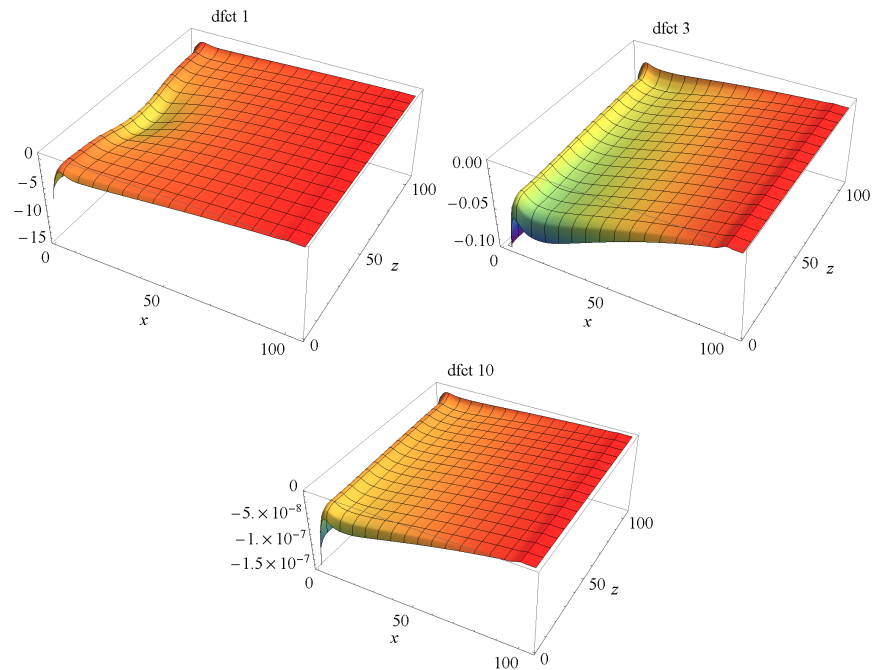


Figure 4.10: Defect after 1, 3 and 10 multigrid iterations of a charged ball placed inside a grounded cylinder.

4.2.2 Examples with Image Charge Effect

Charged particles placed inside an RFQ, will cause image charged on the electrodes which effect the beam. In the following, test problems are described in which the image charge effect is considered. The boundary therefore has the shape of the electrodes of an RFQ and has zero potential, so that the external and the internal fields can be calculated separately making use of the superposition principle.

A simple example of an image charge is the potential of a point charge placed in front of a conducting plate at a distance d . It is equivalent to the situation of two point charges of opposite charge with a distance of $2 \cdot d$ between them. In Figure 4.11 the potential at a perpendicular line to the plate crossing the charge is shown, as well as the potential of two charges with twice the distance. Both potentials have the same shape as expected, so the solver can calculate the image effect correctly as well.

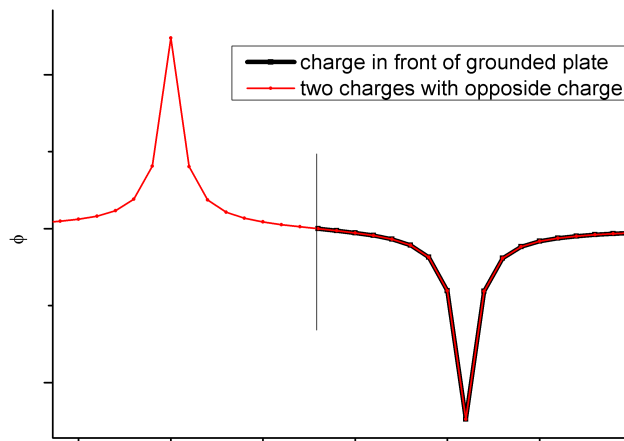


Figure 4.11: Potential of a charge placed in front of a grounded plate and potential of two charges of opposite charge to demonstrate the image charge effect.

The charges used above are now placed inside a grounded quadrupole channel with different apertures. Figure 4.12 shows the potential for the charged cylinder. The maximum of the potential on the beam axis depends on the aperture; with a bigger aperture the maximum increases. Both potentials fall off to zero at the vane tip but in different shape (more stretched for the bigger aperture) and will therefore result in different electric fields. A dependence on the longitudinal position can not be seen, as expected from the reflected longitudinal boundary conditions.

Figure 4.13 shows the potential of a charged ball placed inside a grounded quadrupole channel for different apertures (0.2 cm - 0.8 cm). Just like the charged cylinder the maximum of the potential increases with increasing aperture. The value of potential at the beginning and at the end of the cell also depends on the aperture in the same manner.

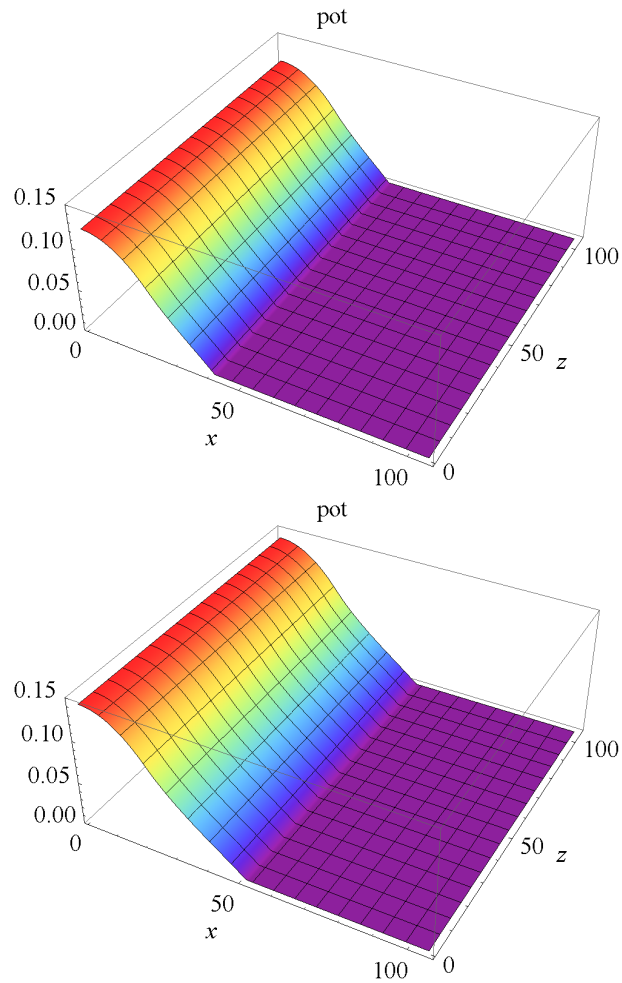


Figure 4.12: Potential after 10 multigrid iterations of a charged cylinder placed inside a quadrupole channel with aperture of 0.4 cm and 0.5 cm.

The shape of the potential on the beam axis is also shown in Figure 4.14 to illustrate the influence of the aperture on the potential. The curves for the smaller apertures are shifted to lower values compared to the curves with bigger apertures. The resulting longitudinal field components will therefore be somewhat close for the different apertures, since the difference between the curves is mainly a constant, which holds only for the longitudinal field. The black curve (aperture and the radius of the

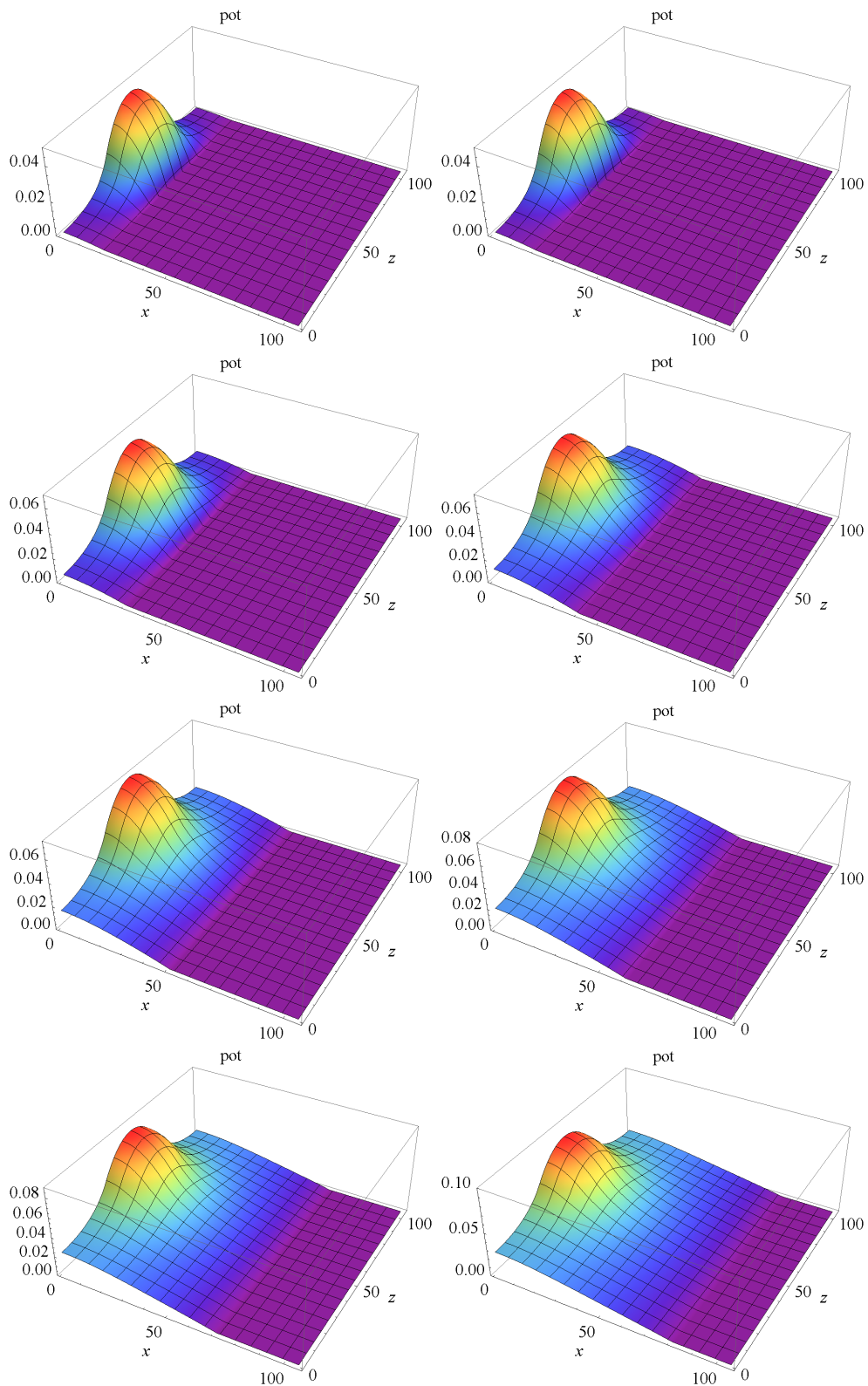


Figure 4.13: Potential after 10 multigrid iterations of a 0.2 cm radius charged ball placed inside a quadrupole channel with apertures from 0.2 cm to 0.8 cm.

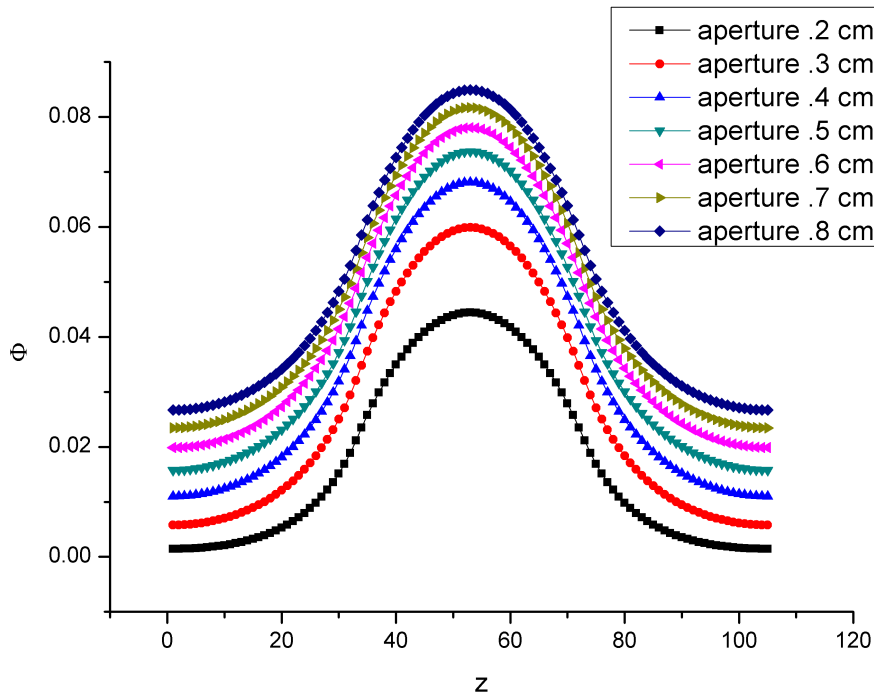


Figure 4.14: Potential along the beam axis of a 0.2 cm radius charged ball placed inside a grounded quadrupole channel with aperture from 0.2 cm to 0.8 cm.

ball are both 0.2 cm) differs in its shape a little from the other curves, since the vane surface is placed directly in front of the charged ball and the image effect is therefore stronger than in the cases having a bigger aperture. If the vane surface is far enough away from the charge density the influence of the image effect is weaker and differences between axial potential decrease. The transverse field, which is the derivative of the curves shown on Figure 4.15, inside the charged ball is quite independent of the aperture, because the potentials (from the center to grid point 20) have the same shape with a constant offset. The field outside the charge density then depends on the aperture. For small apertures the potential must fall off steeper than for big apertures. This results in higher transverse field component for small apertures, because the boundary forces the potential to zero, so it will drop down more rapidly.

Without the image charge effect all of the curves shown above will have the same shape independent of the aperture. Neglecting the image charges in the space charge calculation, leads therefore to strong inaccuracies in the particle dynamic simulations especially for high current and high energy application where the apertures

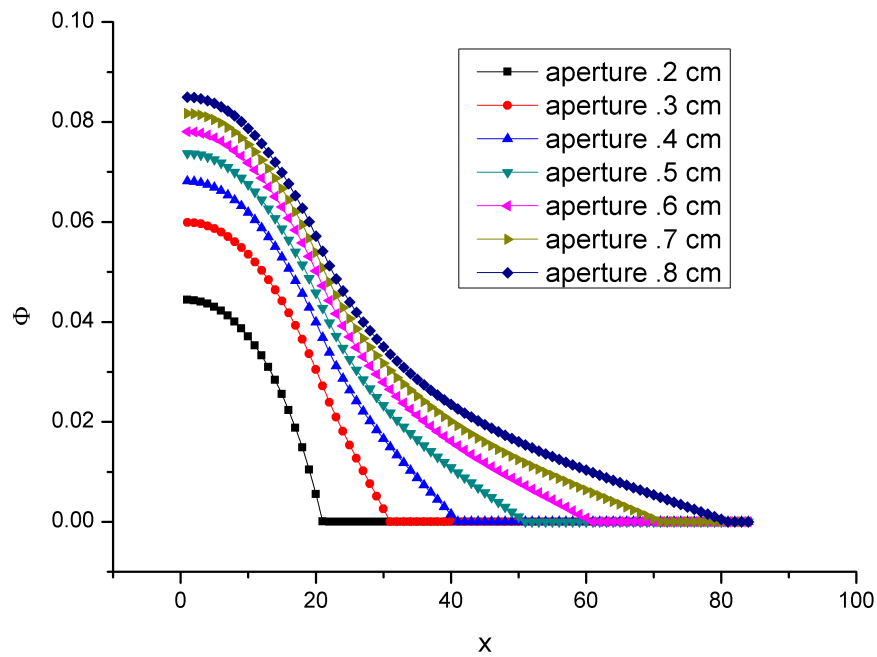


Figure 4.15: Potential on a line from the center of the 0.2 cm radius charged ball to the vane surface.

is kept as small as possible to reduce RF power consumption. Image charges can fully be taken into account by the multigrid Poisson solver and should be used for accurate simulations.

5 RFQ Simulation Results Using the Multigrid Poisson Solver

In this chapter the influence of the multigrid Poisson solver on the simulations of the particle dynamic in RFQs will be described. As the test case a set of 12 RFQs is used, which were designed following the same rules with one parameter varied to find the optimum for this specific parameter. In this case the parameter was the minimum aperture at the end of the shaper section. It has to be mentioned that the goal of designing these RFQs was not to obtain 12 good designs, but to have a wide range of RFQs with differences in their geometry. The same set of RFQs has already been used in [Jam07b] and [Mau08] to compare different simulation programs.

5.1 Description of the Set of Test-RFQs

The main characteristics of the RFQs are chosen to meet the criteria of IFMIF [Jam07a] in terms of resonance frequency, ion species, beam current, et cetera. The main parameters are listed in Table 5.1. The evolution of the aperture of the set of RFQs is shown in Figure 5.1. The different RFQs are identified by the aperture-factor which is proportional to the reciprocal value of the minimum aperture at the end of the shaper section. From the shape of the curves one can tell that the equipartitioning design strategy has been used to lay out the RFQs.

Figure 5.2 shows the evolution of the modulation along the RFQs. They all start with no modulation ($m = 1$) in the radial matching section. The modulation is then increased rapidly to the end of the shaper section, where the beam should reach the equipartitioned, equilibrium condition. In the beginning of the gentle bunching section the modulation is first held constant and then rises further, but with a smaller slope than in the shaper section. The maximum of the modulation is reached at the end of the accelerating section at the end of the RFQ. Even though the basic shapes of the curves are similar for the different RFQs, the values, slopes and section lengths

Frequency	175 MHz
Ion species	deuteron
Input energy	95 keV
Output energy	5 MeV
Beam current	130 mA
Input emittance	150 mm mrad
Voltage	50 – 200 kV
Modulation	1.0 – 2.6
Aperture	0.25 - 1.5 cm

Table 5.1: Main parameters of the set of RFQs used for comparison.

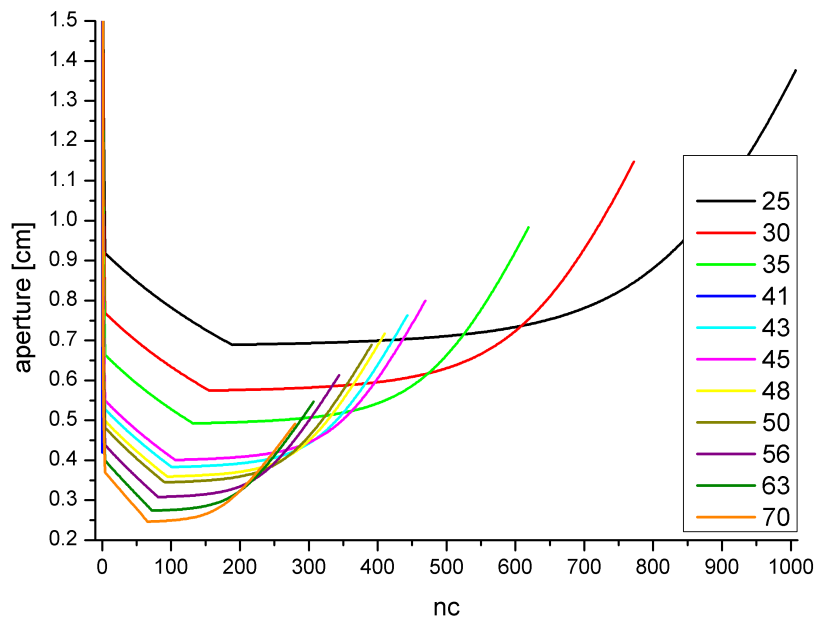


Figure 5.1: Apertures as a function of the cell number for the set 11 RFQs.

differ from RFQ to RFQ.

The synchronous phase of the RFQs is shown in Figure 5.3. The synchronous phase starts with the usual -90° to maximize the longitudinal acceptance for the un-bunched beam and remains unchanged until a designated point in the shaper section, from where it is smoothly increased to start the adiabatic bunching process. In the following gentle bunching and accelerating section the synchronous phase is increased to its final value of around -25° . The slope depends again on the length of the struc-

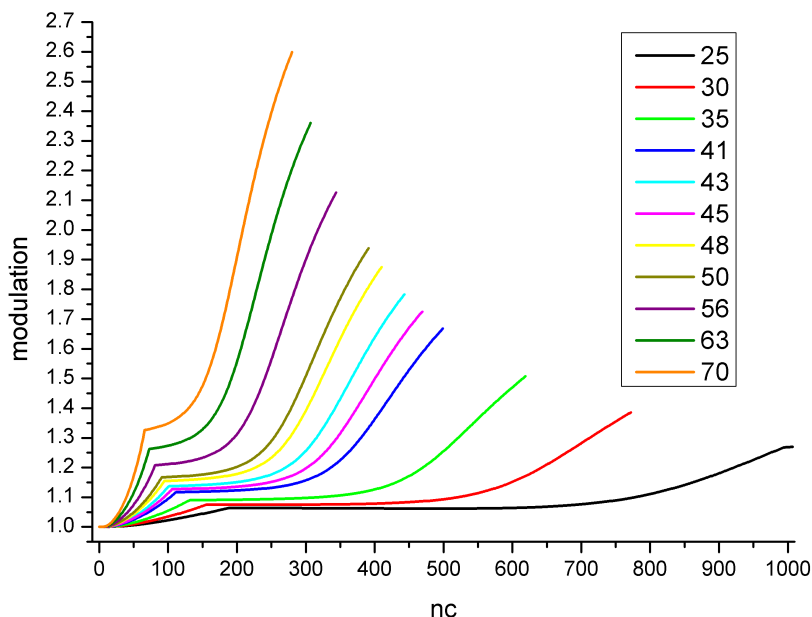


Figure 5.2: Modulation as a function of the cell number for the set 11 RFQs.

ture and therefore on the aperture factor, since the final synchronous phase is similar for all RFQs.

Figure 5.4 pictures the evolution of the energy of the synchronous particle. It starts with the initial input energy of 95 keV and remains unchanged until the end of the gentle bunching section when the synchronous phase has increased. In the accelerating section the synchronous energy is ramped up to its final output energy of 5 MeV.

The different cell lengths of the RFQs are shown in Figure 5.5. They are directly corresponded to the synchronous energy since the frequency is fixed.

5.2 External Field

In this section the influence of the multigrid solver on the external field of the RFQ will be analyzed and compared to the old multipole expansion method. First the field will be illustrated, then the effects on the dynamics of a single particle will be considered and finally, the effect on the particle ensemble will be described. All the corresponding simulations were either done with zero current or with the same space

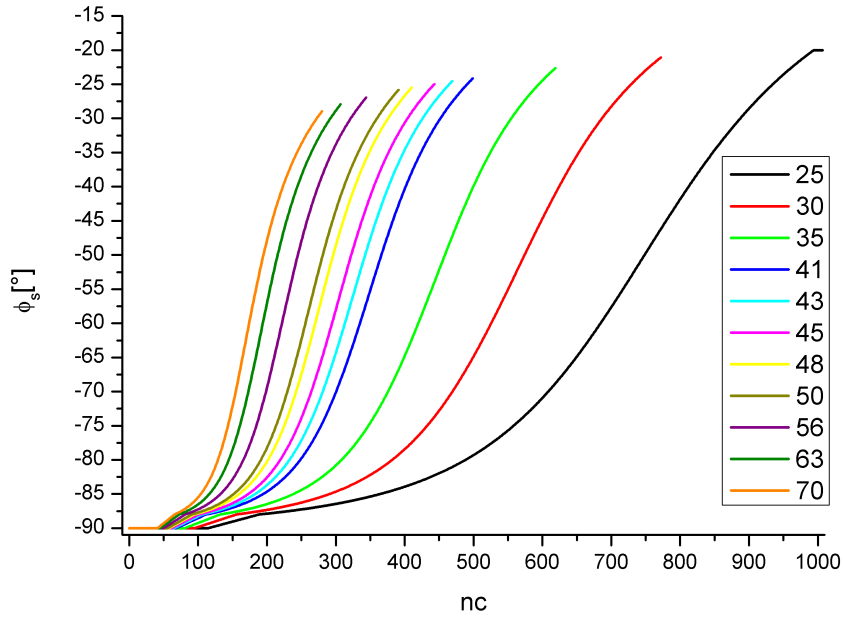


Figure 5.3: Synchronous as a function of the cell number for the set 11 RFQs.

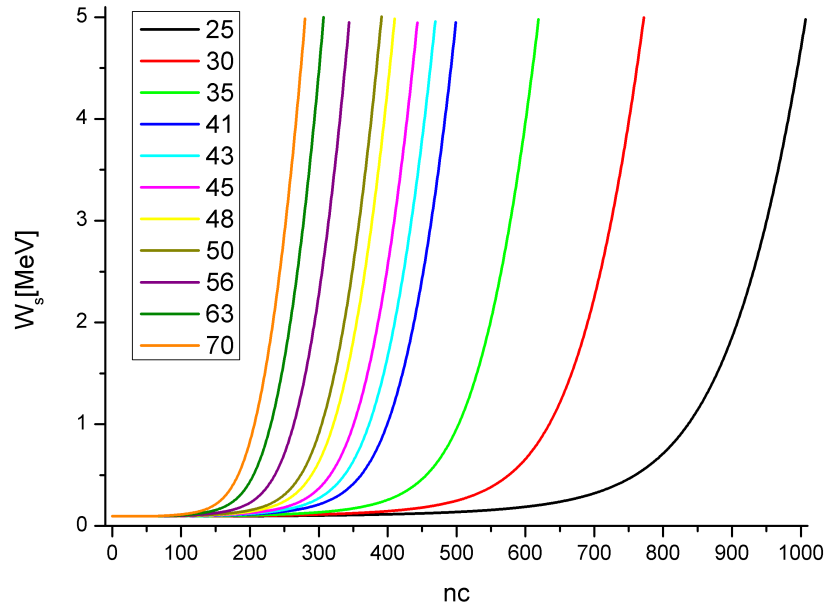


Figure 5.4: Synchronous energy as a function of the cell number for the set 11 RFQs.

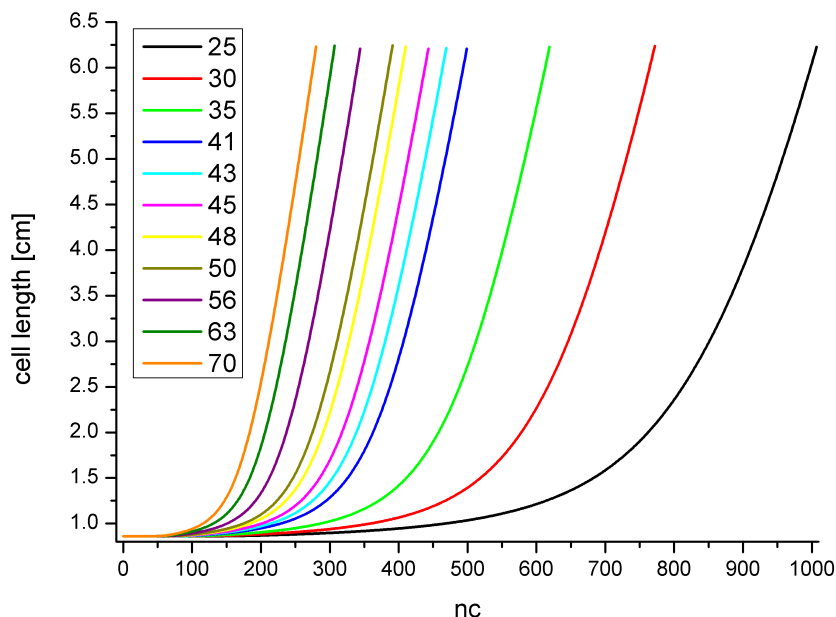


Figure 5.5: Cell length as a function of the cell number for the set 11 RFQs.

charge subroutine to make sure that the effect of space charge is treated in the same way for multigrid and for multipole expansion runs.

5.2.1 Illustration of the Field

Since the generation of the mesh and the solving for the potential is always done in the same way, an arbitrary RFQ can be chosen to illustrate the external field inside an RFQ. The RFQ with an aperture factor of 48 was chosen, because it is somewhere in the middle.

In the following the potential as well as the corresponding electric field components are shown for different cells along the RFQ for two different planes. In Figure 5.7 the potential and the electric field for cell number 10 in the xy -plane are shown. On the picture of the potential the electrodes at opposite potentials can be seen. The beam axis has a zero potential, since the modulation at this position of the RFQ is very small. The breakout angle φ (defined in Figure 5.6) of 10 degrees of the electrodes is also visible. The second picture illustrates the x -component of the electric field (E_x). At the beam axis E_x is equal to zero and it rises linearly up to its maximum value by approaching the x -electrode. The transition from vacuum to electrode seems to be

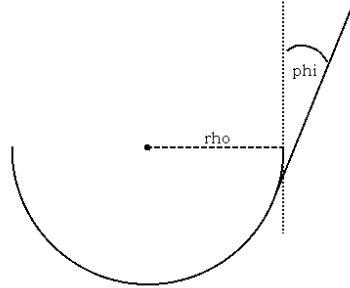


Figure 5.6: Definition of the breakout angle

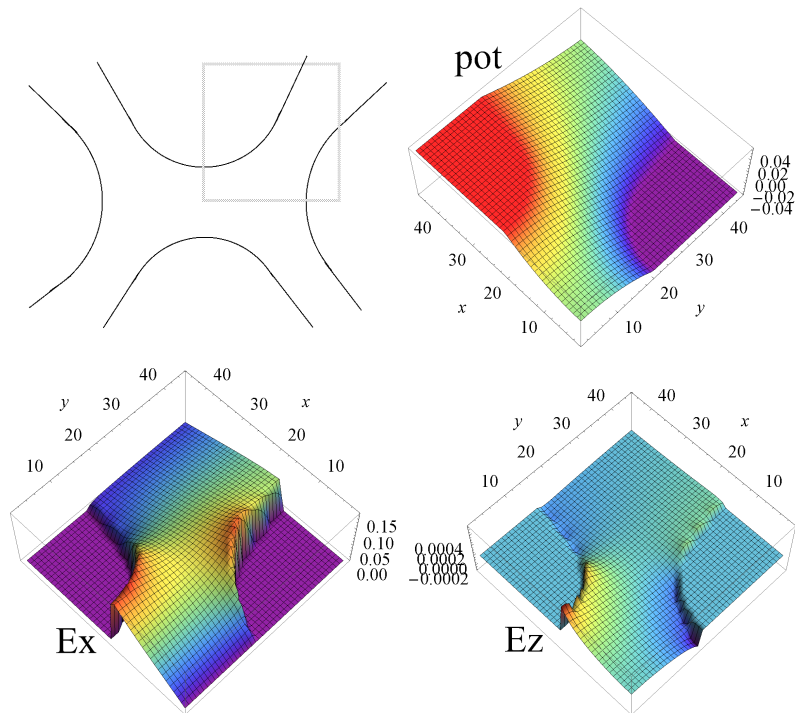


Figure 5.7: XY-plane of the potential, E_x and E_z through cell 10.

somewhat rough. There are two reasons for this kind of behaviour. For finding each field component for one regular grid point, the two-sided derivative schema is used and therefore the potential of each neighbouring grid point has to be known. When the center grid point lies on the surface of the electrode (shifted grid point), the value of one of the neighbouring grid points is equal to the center grid point and therefore the one-sided derivative schema is used. The necessary change of the schema is not perfectly smooth.

The second reason is due to shifting the last grid point to make sure that there is always a (shifted) grid point lying on the surface of the electrode. This effect is not taken into account while plotting the potential and field components. So the surface plots look rougher than they actually are. This is the dominant effect.

The longitudinal field component E_z indicates a small longitudinal field at the region close to the electrodes, with the amplitude lower than the transverse field by a factor of 400. Again, there is only a very small modulation at this point.

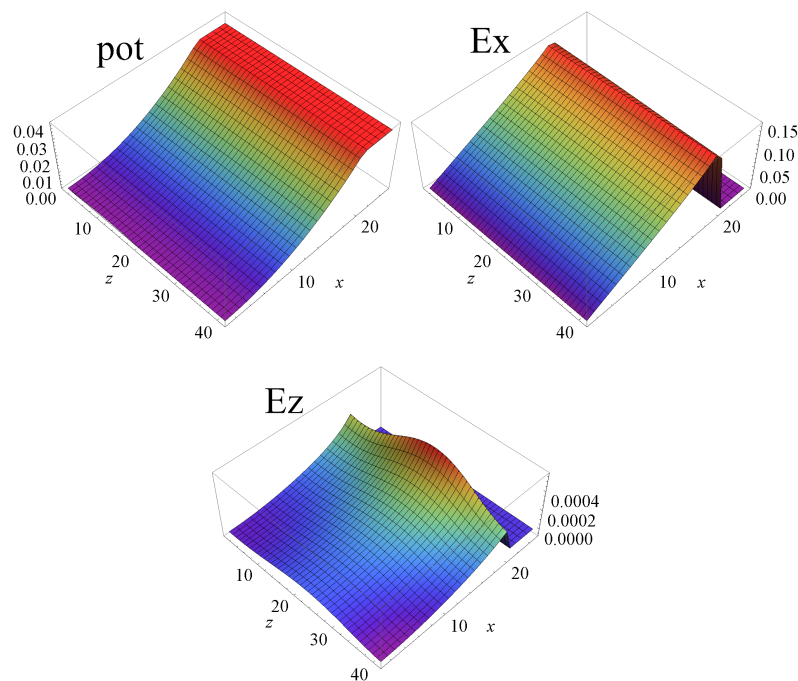


Figure 5.8: XZ-plane of the potential, E_x and E_z at the center of cell 10.

Figure 5.8 shows the potential and the electric field components for the same cell, but in the xz-plane. On the potential plot the electrode can be seen with its constant potential. A little effect of the small modulation can be noticed. The E_x -component of the field increases linearly from the beam axis to its maximum at the

electrodes without any perturbation. The longitudinal field component is very small around the beam axis, but it increases a little at the electrodes due to a very small modulation. Along the beam axis as well as on any line parallel to the beam axis the longitudinal field has a sinusoidal shape.

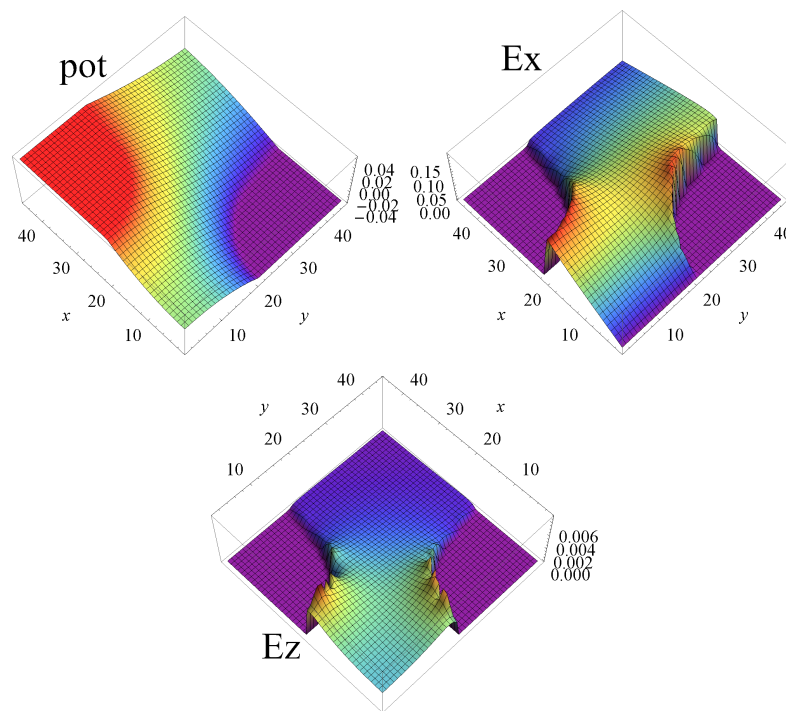


Figure 5.9: XY-plane of the potential, E_x and E_z at the center of cell 50.

The potential and field components for cell 50 for the xy- and xz-plane are shown in Figures 5.9 and 5.10. The longitudinal field components have increased compared to cell 10 as expected. Particles on the beam axis see some bunching forces due to the on axis longitudinal field component, which increase smoothly up to the electrodes with some remains of the shifted grid point effect. The transverse field component has not changed much. On the xz-plane (Figure 5.10) the influence of the modulation on the potential and the longitudinal field component can be seen. The potential at the beam axis has a sinusoidal change in its amplitude, which results in a non-zero longitudinal field component. The maximum is again at the region close to the electrodes, but it is quite flat up to 2/3 of the aperture.

The last cell considered here is accelerating cell (400) with a modulation of $m = 1.8$. The potential and the two components of the electric field are shown in Figure 5.11 for the xy-plane and in Figure 5.12 for the xz-plane. In the transverse

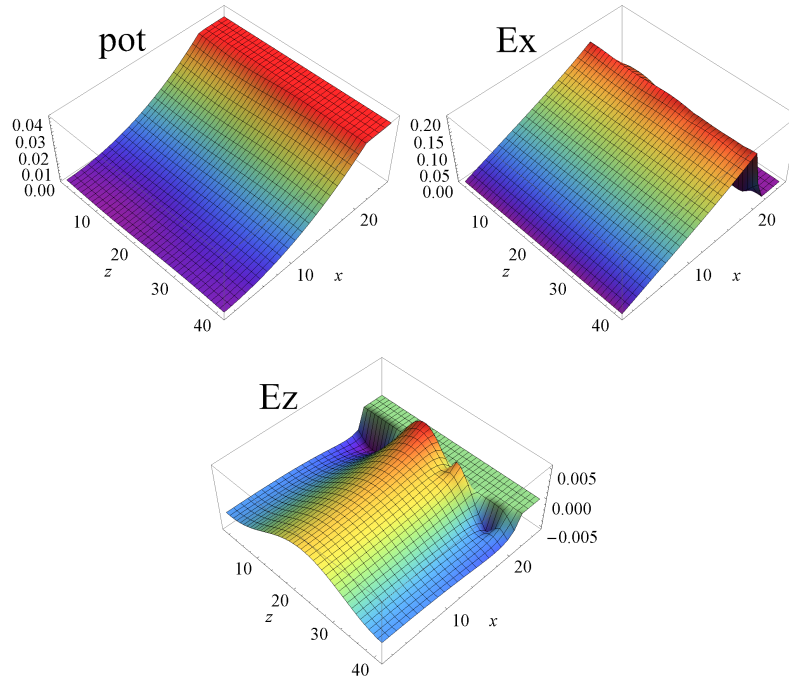


Figure 5.10: XZ-plane of the potential, E_x and E_z at the center of cell 50.

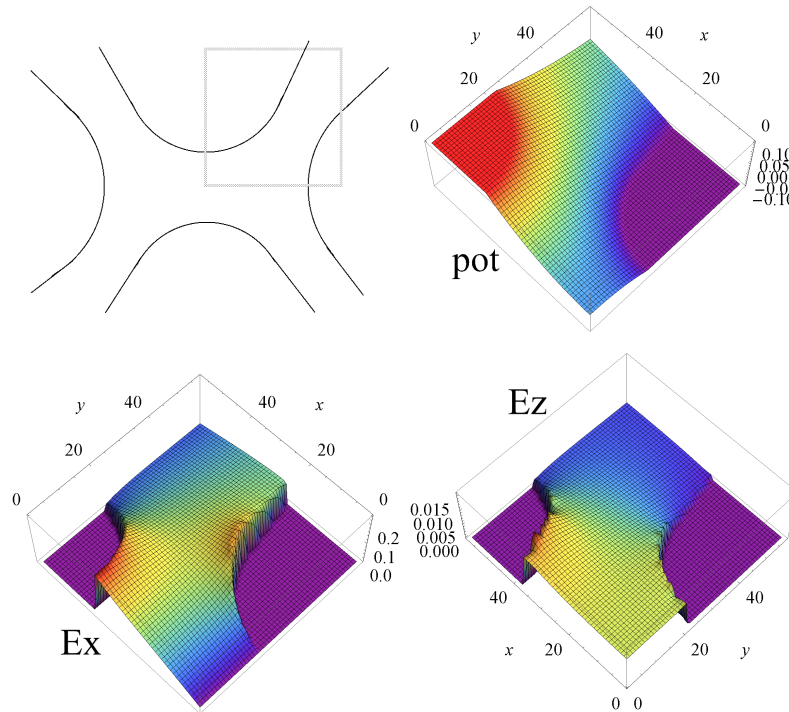


Figure 5.11: XY-plane of the potential, E_x and E_z at the center of cell 400.

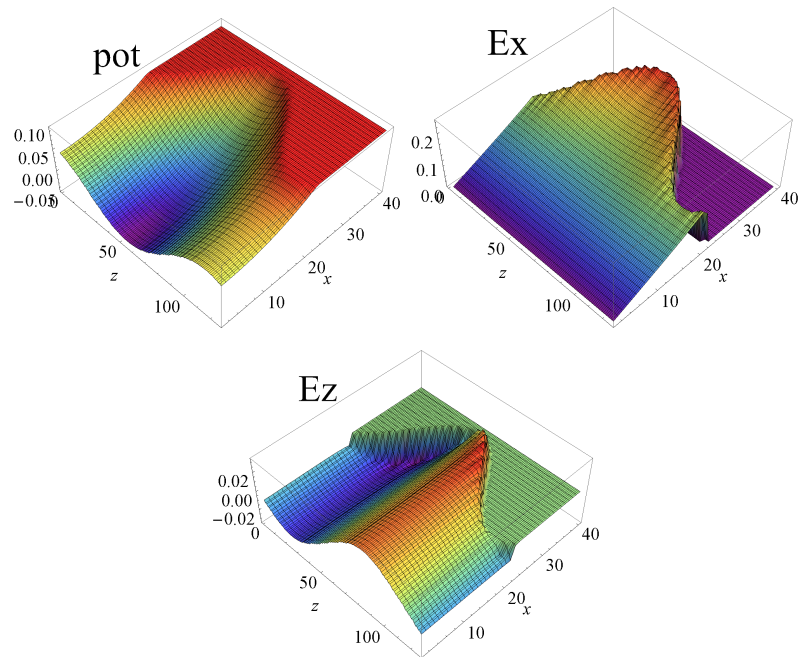


Figure 5.12: XZ-plane of the potential, E_x and E_z at the center of cell 400.

plane the potential at the beam axis is not zero any more, but pushed to a lower values by the modulation. The displacement of the horizontal and vertical electrode is quite different, changing the shape of the potential. The shape of E_x is basically the same than in cell 50: linear increase towards the x-electrode. The potential along the beam axis (Figure 5.12) has a sinusoidal shape, which is directly corresponding to the modulation on the electrodes. The transverse field has also remained unchanged (besides the modulation of the electrodes), but the longitudinal field has increased its strength compared to the previously shown cell.

5.2.2 Comparison to Potential of Multipole Expansion

Method

One reason for implementing a Poisson solver was that the multipole expansion is only accurate within the region of the minimum aperture, since it derives from the cylindrically symmetric approximation of equation 2.36 in chapter 2, and its coefficients are calculated by integrating along an arc with a radius of the minimum aperture on a field map found by another Poisson solver. Therefore a difference in the region beyond the minimum aperture is expected.

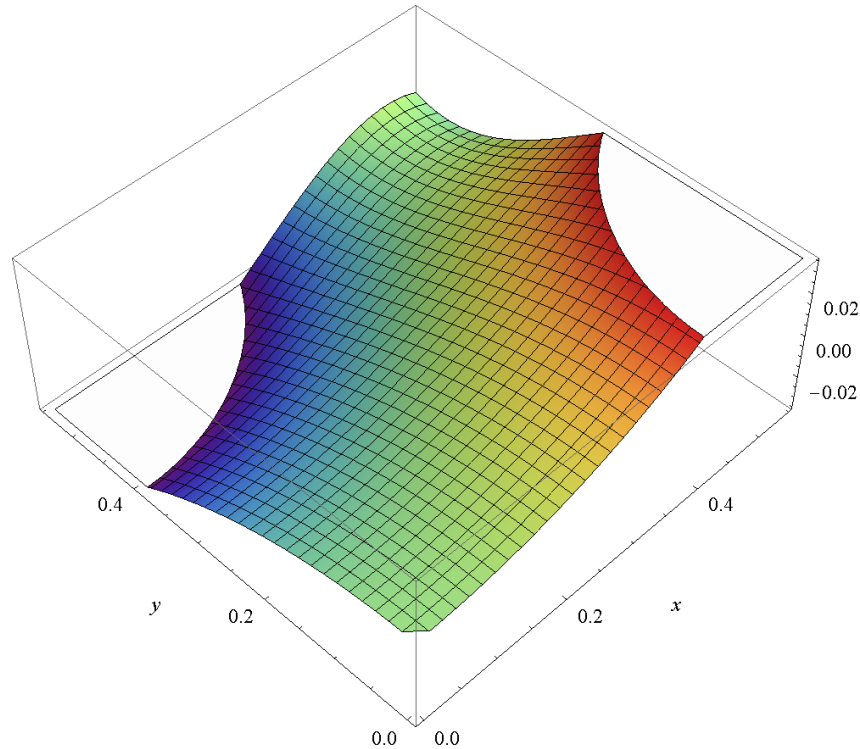


Figure 5.13: Potential from the multipole expansion method at the center of cell 150 as a function of x and y .

Figure 5.13 shows the 8-term multipole potential in the xy -plane at the center of a cell, truncated at the vane boundaries; the white areas at the top and bottom indicate regions where the potential is higher than the positive vane voltage or lower than the negative voltage. Apparently, there seems to be a second positive and negative electrode, which is due to the inaccuracy of this description of the potential. At the region of the beam axis the potential has the expected shape.

Figure 5.14 shows the potentials from the two different methods at the same position. In the useful zone at the beam axis the two potentials compare actually quite well. Only further out there are major differences. Only a few particles will never go so far and therefore both methods can be reasonably be used. It has to be noted that the modulation at this position is quite small ($m = 1.16$) and the potential at the middle of the cell is shown where the displacement of the horizontal and the vertical electrode is the same. So it is not surprising nor significant that the two methods give similar potentials. It indicates that the Poisson solver finds a potential which compares quite well to the potential from the multipole expansion method in a situation where the multipole expansion method is a accurate description of the external field.

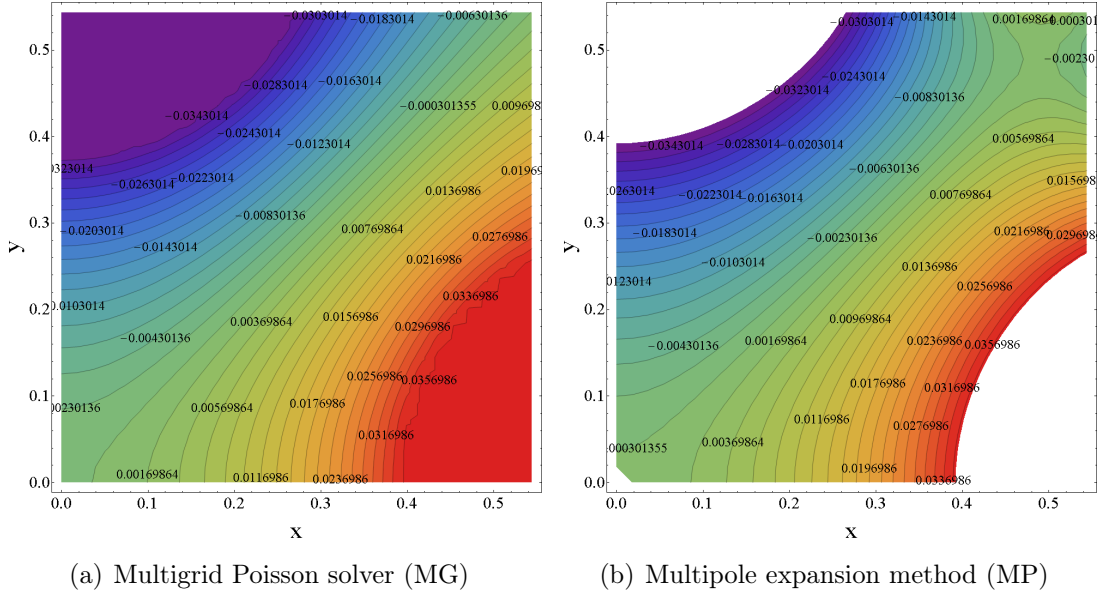


Figure 5.14: XY-plane of the potential from the multigrid Poisson solver and from the multipole expansion method at the center of cell 150.

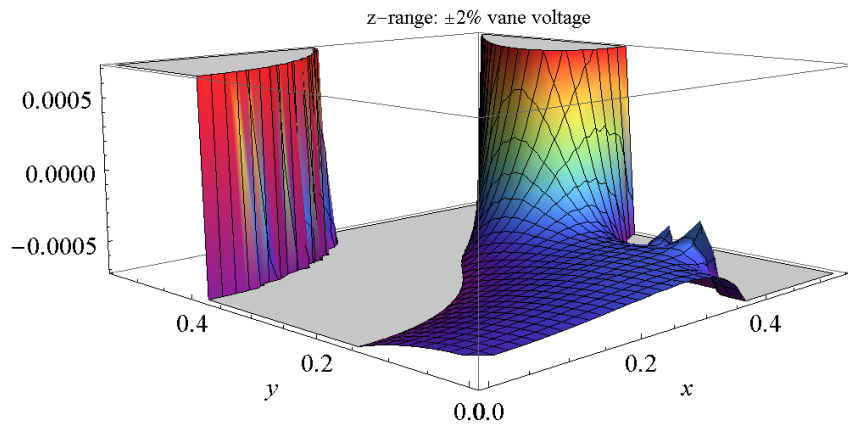


Figure 5.15: Absolute difference of the potentials from the multipole expansion method and from the multigrid Poisson solver at the center of cell 150.

The absolute differences of the two potentials are shown in Figure 5.15. The z range of the plot is $\pm 2\%$ of the vane voltage. It can be seen that there is a offset of around 1.5% of the vane voltage. Beside that, the difference is relative smooth and small. The point at the beam axis is missing, because the multipole expansion method gives its potential normally in cylindrical coordinates and the transformation to Cartesian coordinates involves an arctangent.

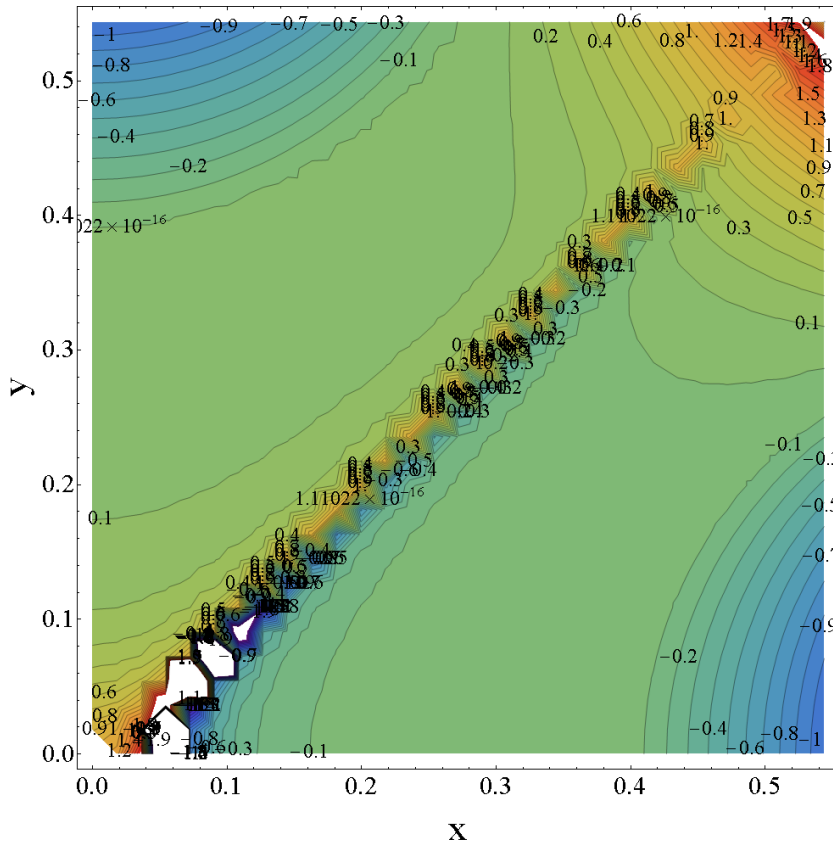


Figure 5.16: Relative difference (MG-MP)/MG of the potentials from the multipole expansion method and from the multigrid Poisson solver at the center of cell 150.

The last picture of cell 150 is the relative difference shown in Figure 5.16. The problem on relative differences is that the potential crosses through zero and than the relative values become big without any importance. Beside this effect the relative difference at the beam axis is less than 10% .

Now, we consider a situation in which the limitation of the multipole expansion method is revealed. The potential at the end of a cell with a modulation of

$m = 2.3$ for the two different methods is shown in Figure 5.17. Potentials that are greater than the vane voltage have been cut off. Obviously, the shape of the electrodes (white area) of the MP-potential is not even close to the shape of the electrodes. Close to the beam axis the two methods give similar potentials, but with increasing displacement from the beam axis, differences increase as well. In between the electrodes, the potential has to change from plus to minus the vane voltage. For the MP-potential the distance between the electrodes has become very small compared to the actual shape of the electrodes used in the MG-potential (potential from the multigrid Poisson solver), therefore the electric field calculated from the MP-potential will be higher than it essentially is. Also the position of the horizontal vane in the MP-potential is too far away from the axes and therefore the corresponding electric field is too low. In Figure 5.18 the relative differences of the potentials are shown. At the beam axis

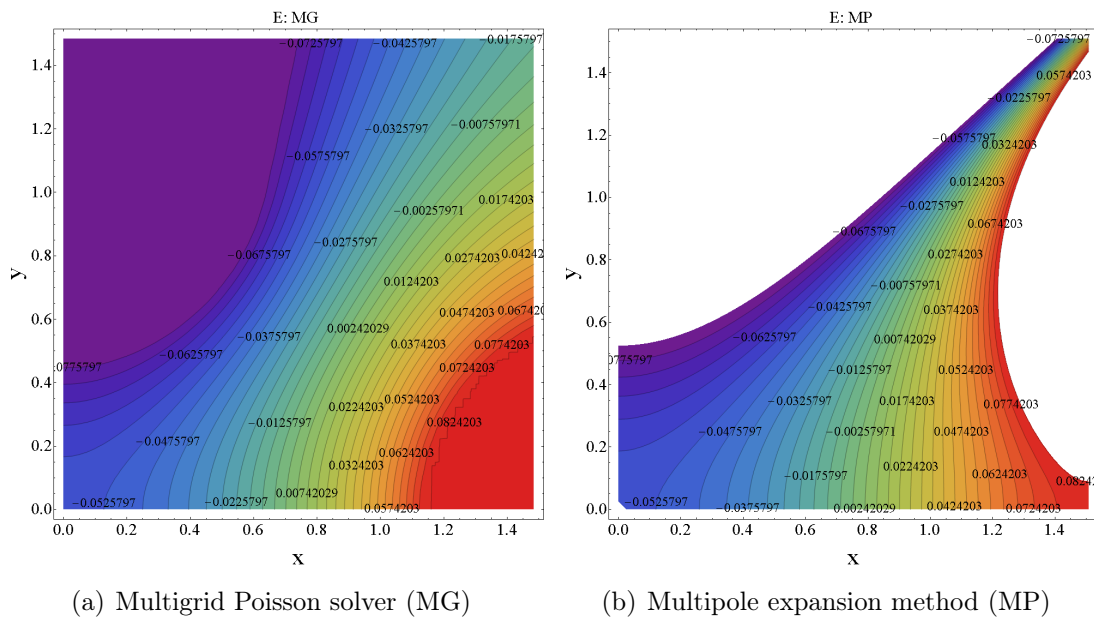


Figure 5.17: Potential from the multigrid Poisson solver and from the multipole expansion method at the end of cell 300.

the difference is again less than 10%, but as soon as the displacement from the axis increases the difference become bigger than 40%. Towards the horizontal vane the error of the MP-potential becomes even bigger.

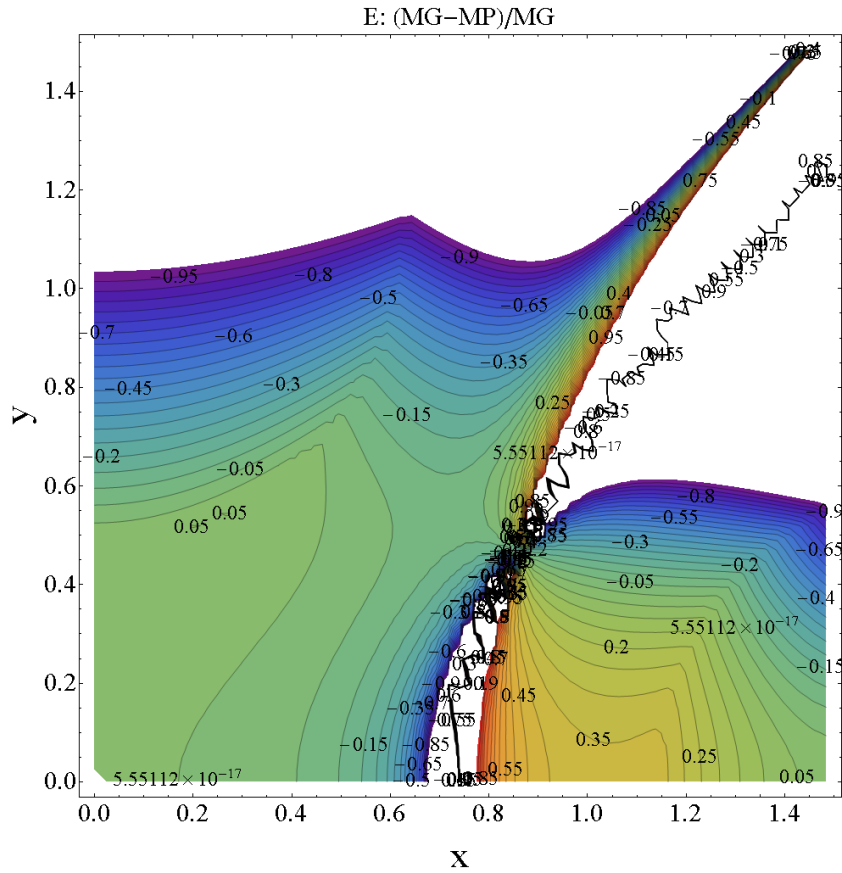


Figure 5.18: Relative difference $(MG-MP)/MG$ of the potentials from the multipole expansion method and from the multigrid Poisson solver at the end of cell 300.

5.2.3 Comparison of E_x

Different potentials as shown in the previous section will lead to different electric fields. The x-component of the electric field in the xy-plane for the multipole expansion method and for the multigrid Poisson solver is shown in Figure 5.19. In the left picture (MG-field) the electrodes are visible as those regions with a flat zero electric field. The multipole expansion method does not have any information about the electrodes. Starting from the x-axis in both plots the field components increases linearly with equidistant equipotential lines. In the MG-case this incline stops at the vertical electrode whereas it continues for the MP-case. This is not a problem, since particles which touch the electrodes are considered transversely lost. In between the electrodes the field component increases further for the MP-case. In the MG plot there are some local maxima at the electrodes, which are not present in MP plot.

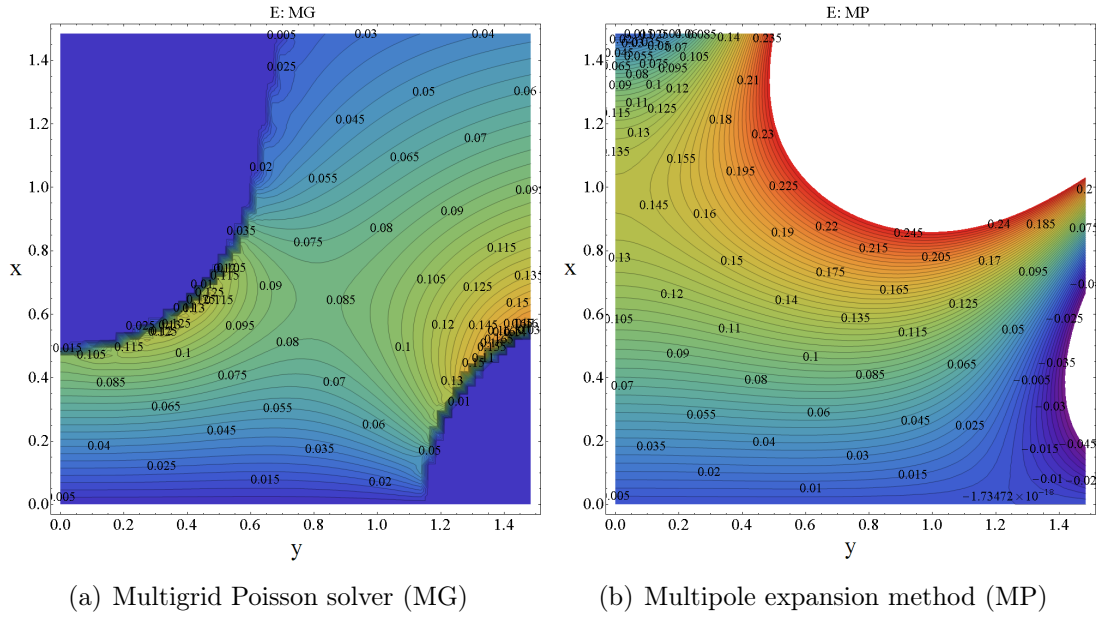


Figure 5.19: X-component of the electric field (E_x) in the xy-plane at the end of a accelerating cell.

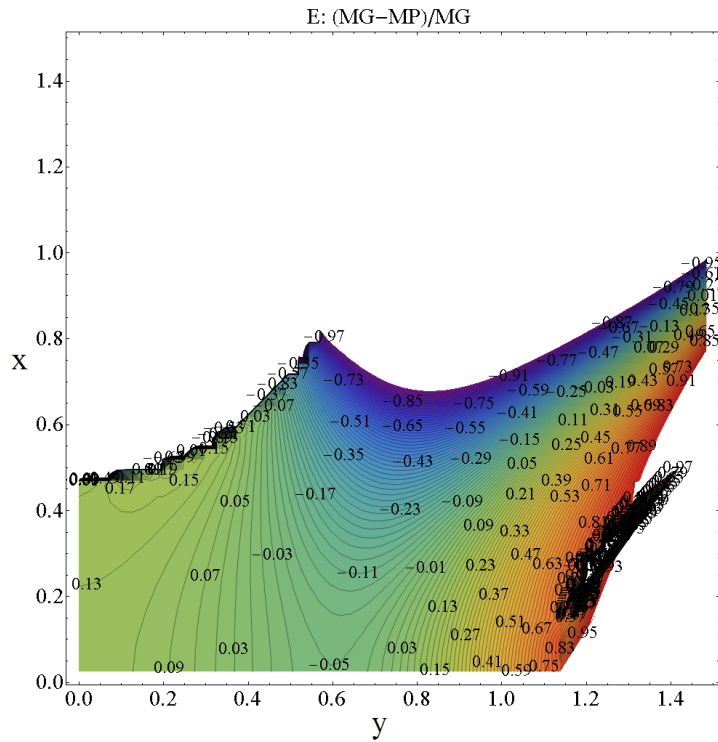


Figure 5.20: Relative difference (MG-MP)/MG of the x-component of the electric field (E_x) in the xy-plane at the end of a accelerating cell.

The relative difference of the two plots is shown in Figure 5.20 and at the useful zone around the beam axis the difference is less than 15% - this is, however, a very significant difference in terms of achieving a physically correct and accurate simulation. Starting from in between the electrodes the field starts to look quite different. Especially in front of the electrodes there are effects that can not be represented by the multipole expansion method.

The absolute value of the electric field at the same position is shown in Figure

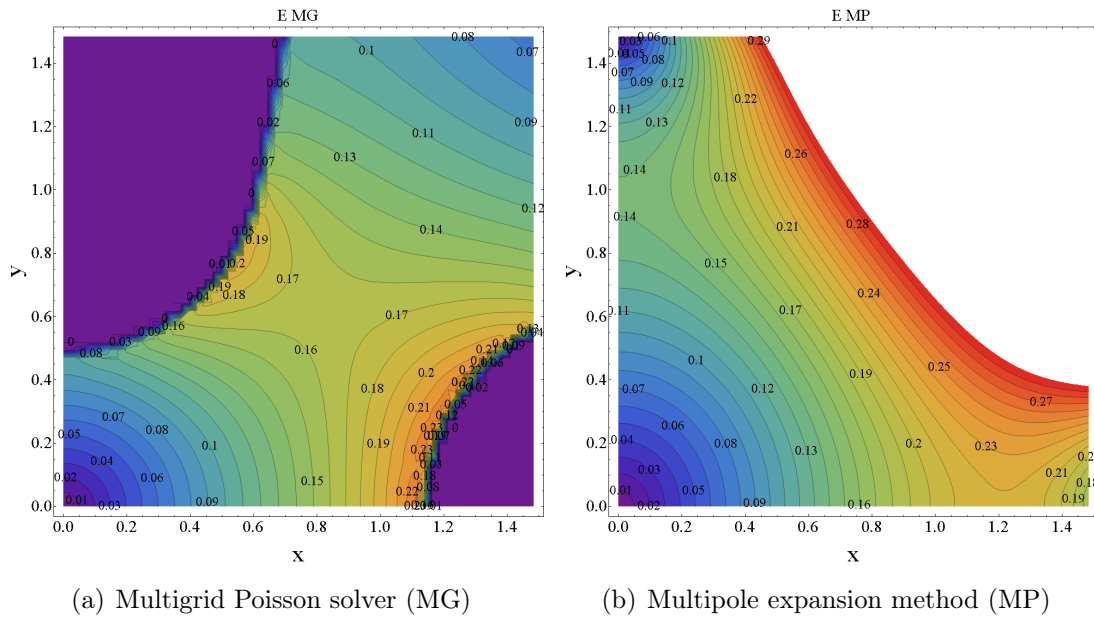


Figure 5.21: Absolute value of the electric field (E) in the xy -plane at the end of an accelerating cell for multigrid Poisson solver and multipole expansion method.

5.21. The maximum electric field is in the region close to the electrodes and does not appear on the field plot from the multipole expansion method. At bigger distances away from the beam axis (lower left corner) the MP-field increases to its maximum whereas the MG-field tends to decrease which is reasonable since the vane voltage remains constant and the distance between the electrodes increase. Therefore a big relative difference is expected with a minimum at the beam axis. Figure 5.22 showing the relative difference of the absolute values of the field confirms this.

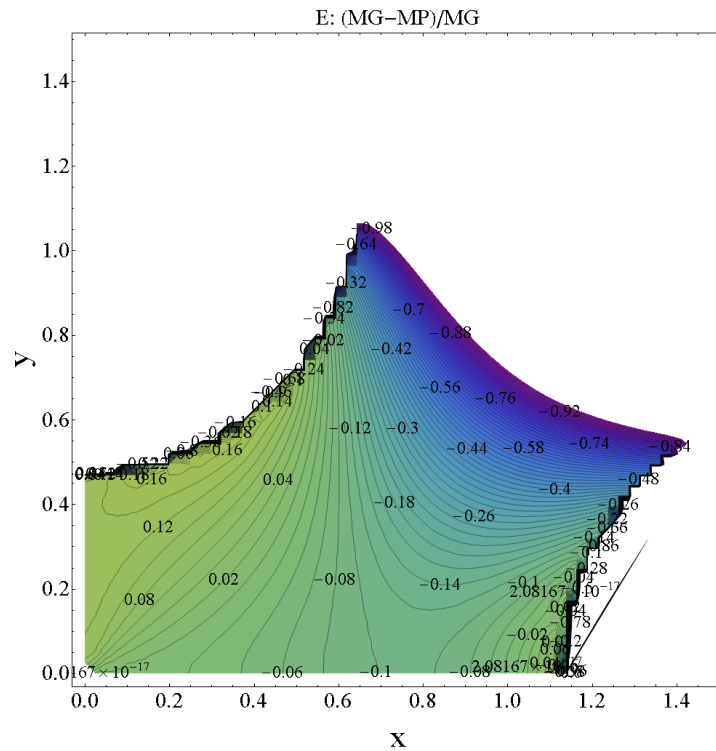


Figure 5.22: Relative difference $(MG-MP)/MG$ of absolute value of the electric field (E) in the xy -plane at the end of an accelerating cell.

5.2.4 Influence on the Single Particle Dynamics

As the next step, the influences on single particle dynamics is now analyzed. The first particle analyzed is the synchronous particle shown in Figure 5.23. As there is no true synchronous particle in the time code, a particle that remains on-axis transversely, receives only the accelerating force, and is not affected by space charge is added for diagnostics. Here the phase of that particle is plotted as function of the cell number for three different RFQs. The black curve is the design synchronous phase, the red curve comes from a run using the multipole expansion method for representing the electric field and the blue curve is the one from external field of the Poisson solver. In all three RFQs the behavior of the MP-phase (multipole expansion method) compares very well to the design phase. This is due to the usage of the multipole expansion method in the design procedure. So the synchronous particles is excited to the same external field, ideally, with which the RFQ was designed. When the Poisson solver is used to calculate the external field the behavior of the synchronous particle changes. For small apertures (a -factor=63) the difference is small and increases with increasing

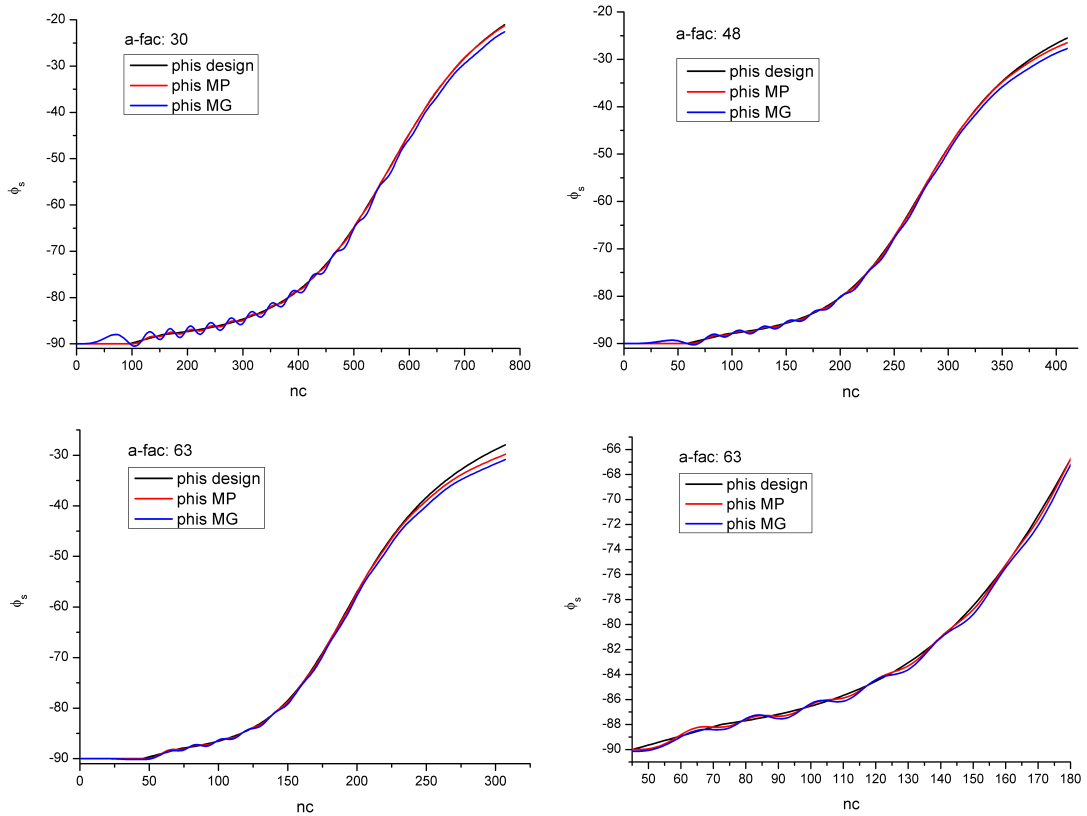


Figure 5.23: Synchronous phase as function of the cell number for different RFQs (30, 48, 63) and different method for the external field (MG: multigrid Poisson Solver; MP: multipole expansion method).

apertures. For big apertures the phase of the synchronous particle oscillates around the design phase in the beginning of the structure. With increasing phase this oscillation is damped. The graphs do not indicate which behaviour is right, but it clarifies that the dynamic of the particles depend on the chosen method for the external field.

Secondly, an arbitrary particle was chosen and the two different approaches were set up to determine the longitudinal kicks (change in momenta) of that particle along the RFQ, but only one method was driving the particle, to make sure that the positions for the two setups remain the same. The transverse kicks along the complete structure are shown in Figure 5.24. The blue curve indicates the difference of the kicks from multipole expansion method and Poisson solver. The oscillation of the RF (high frequency) as well as the betatron oscillation of the single particle through the bunch (low frequency oscillation) can be seen. The betatron oscillation frequency seems to decrease along the RFQ, which is due to the energy gain of the particle: classic betatron

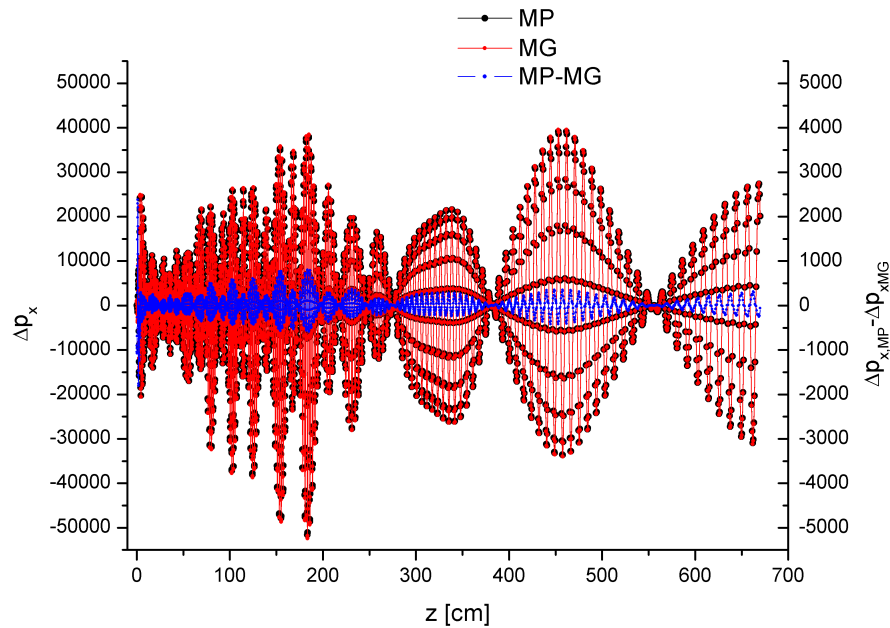


Figure 5.24: Transverse kicks from multipole expansion method and multigrid Poisson solver on a single particle $\Delta r_{Start} = 0.5 \cdot r_{rms}$ along the RFQ (MG: multigrid Poisson Solver; MP: multipole expansion method).

damping. In general the amplitude of the MP-kicks is bigger than the MG-kicks, but the difference is not very big in the main part of the RFQ. In the beginning of the RFQ the difference is a little bigger than in the rest of the structure and hence the transverse kicks for the first 20 cm are shown in Figure 5.25. The multipole expansion method does not have an accurate representation of the fringe field region and it starts in our case directly with the first cell of the radial matching section, whereas the multigrid Poisson solver starts with a grounded plate (representing the tank wall) followed by an empty cell and then the electrodes start. This gives a more realistic picture of the real machine. For further studies a more precise map of this region can be drawn with bore hole and a thick tank wall. Thus, the rise of the field is different from MP to MG. The MP-kicks start with zero, since there is no fringe field effect taken into account, but the multigrid Poisson solver assigns some non-zero kicks to the particle. In the radial matching section the aperture changes quite rapidly and hence the multipole coefficients need to be changed as well which does not happen. The Poisson solver on the other hand finds the potential introduced by the actual shape of the electrodes giving a more precise description of a real machine.

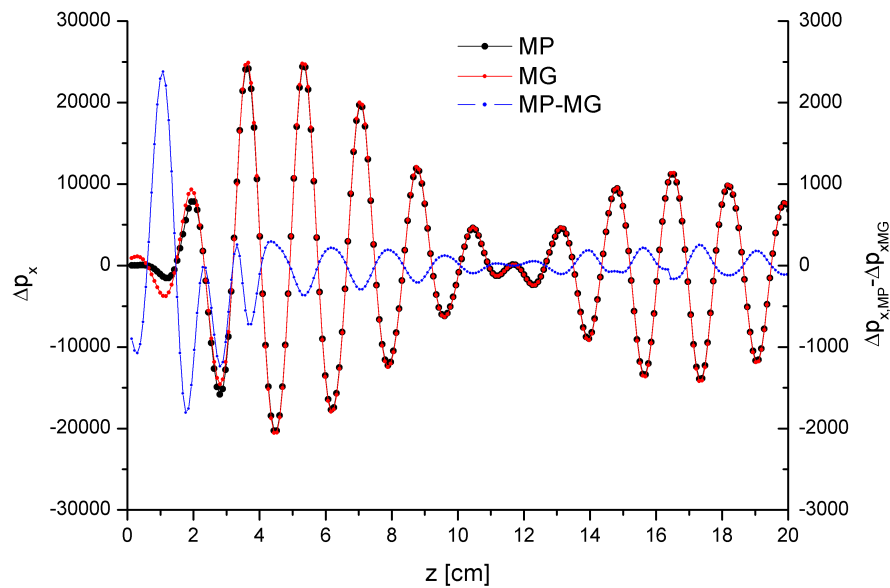


Figure 5.25: Transverse kicks from multipole expansion method and multigrid Poisson solver on a single particle along the beginning of the RFQ (MG: multigrid Poisson Solver; MP: multipole expansion method).

In Figure 5.26 the evolution of the longitudinal kicks are shown for the same particle. As for the transverse kicks, two different type of oscillations take place. One is the oscillation of the RF and the other is the synchrotron oscillation of the particle passing longitudinally through the bunch. In the beginning of the structure the kicks oscillate about zero and the energy of the particle remains unchanged (only some bunching takes place). After some cells inside the RFQ the longitudinal kicks oscillate about a positive value and the particle gets accelerated. The shape of the curves from the multigrid Poisson solver and from the multipole expansion method are again quite similar in the main part of the RFQ.

In the beginning of the structure the differences are big compared to the small longitudinal field components (Figure 5.27). After the radial matching section the longitudinal kicks are very small and they increase slowly to form the bunch. In the radial matching section however the longitudinal electric field is not equal to zero, because the quadrupole geometry is perturbed by the change of the aperture. The multipole expansion method obtains in this region a different field than the multigrid Poisson solver which takes the actual shape of the electrodes into account.

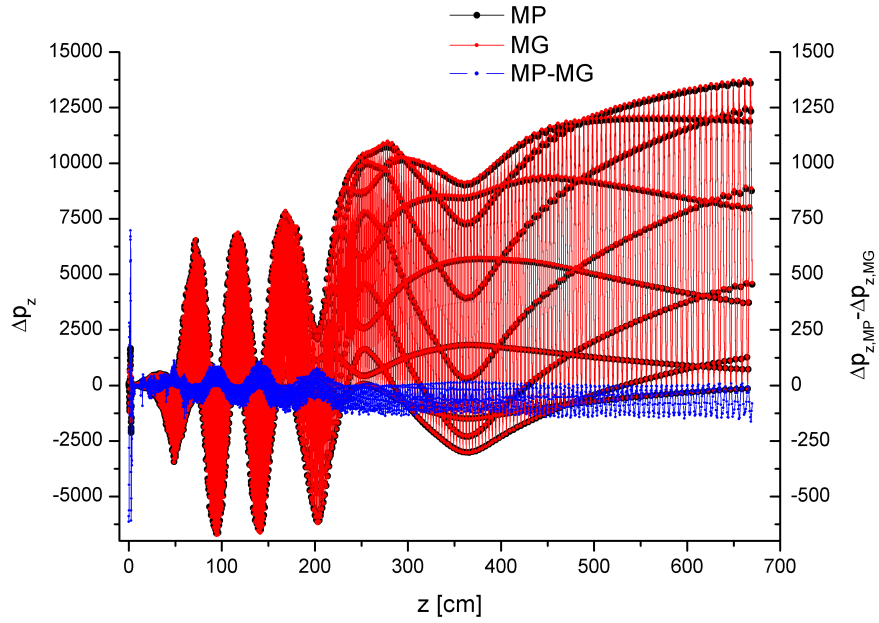


Figure 5.26: Longitudinal kicks from multipole expansion method and multigrid Poisson solver on a single particle ($\varphi = 0^\circ$) along the RFQ.

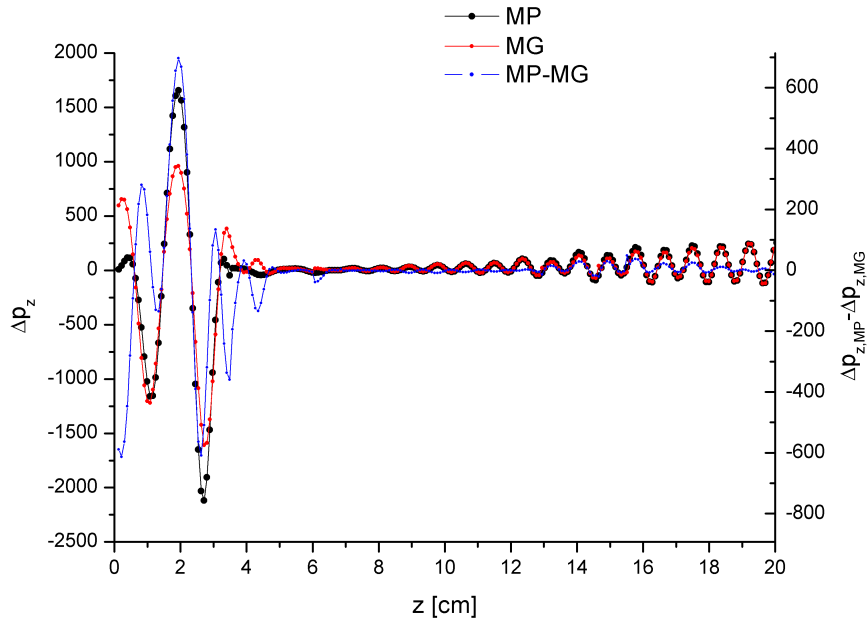


Figure 5.27: Longitudinal kicks from multipole expansion method and multigrid Poisson solver on a single particle along the beginning of the RFQ.

5.2.5 Collective Effects

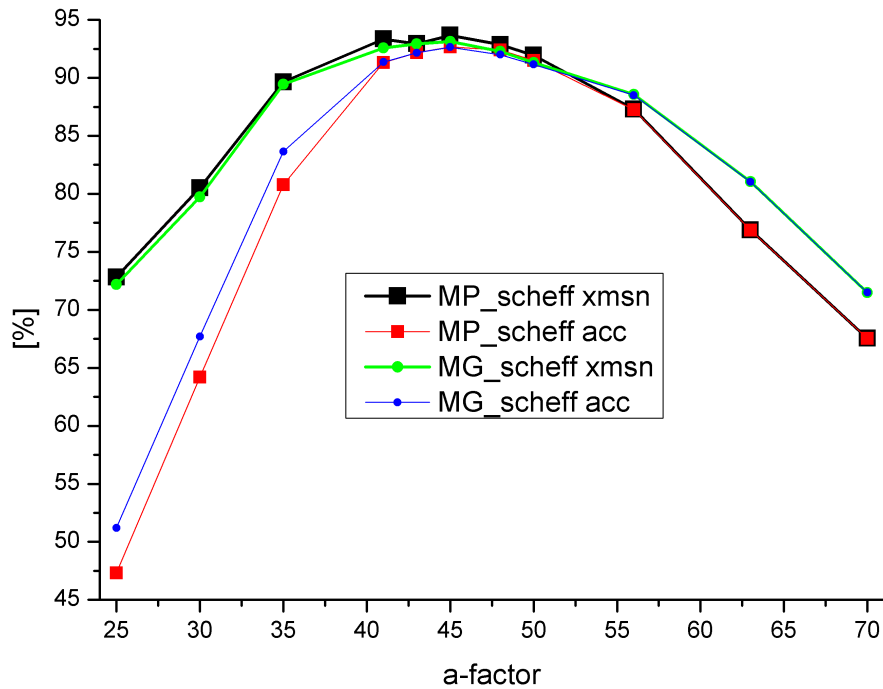


Figure 5.28: Transmission (xmsn) and percentage of accelerated beam (acc) for different external fields (MG: multigrid Poisson solver; MP: multipole expansion method) for the set of 11 test-RFQs.

The influence of the different descriptions of the external field on the transmission are discussed in this section. The runs used here were both done with the same space charge routine (SCHEFF) and different options for the external field. A zero current run can not be considered due to the very high transmission for all the RFQs and the behavior of the beam in the quadrupole channel is different. Figure 5.28 shows the transmission and the fraction of accelerated particles as a function of the aperture factor. The wavelength over $((\text{aperture factor})/10)$ gives the minimum aperture at the end of the shaper section. On the left hand side the aperture of the RFQs is big and becomes smaller with increasing a-factor. The transmission curve for the multipole expansion method and for the multigrid Poisson solver are very close for the RFQs with a medium and big aperture. Once the aperture has become small enough, the results from the two different method start to deviate from another. The

multigrid Poisson solver gives higher values for the transmission. For the first three large aperture (a-factor 25, 30 and 35) RFQs the fraction of accelerated is higher for the MG cases than for the multipole expansion method.

This behavior of the transmission curve fits quite well in the considerations so far. For big apertures, radial losses are not as large an effect, and the multipole expansion method agrees more closely with the Poisson solver. For smaller apertures the effects at the aperture and therefore at the edge of the area of validity of the multipole expansion method become important and the multigrid Poisson solver is a more accurate description of the external field. There is a difference between the multipole expansion method and the multigrid Poisson solver and a Poisson solver should be used for precise simulations.

5.2.6 Sensitivity of the Poisson Solver

The next step is to analyze the sensitivity of the multigrid Poisson solver. There are two different types of parameters to be chosen. The first are the number of multigrid iterations being executed and the number of smoothing cycles on every grid. Figure 5.29 shows the influence of these two parameters on the number of accelerated particles for the set of test-RFQs. All curves are very similar except the black curve (3 multigrid iterations with 4 smoothing cycles) which is the roughest setting used in this comparison. As the standard settings 5 multigrid iterations and 4 smoothing cycles on every grid (except when the ratio of dr and dz exceeds 4 (then 7)) is used; this is the green curve in the plot. A further increase of the number of multigrid iterations does not change the results for the transmission.

The second parameter which needs to be chosen is the grid resolution dr and dz : the distance between two neighboring grid points. They are determined as a fraction of the minimum aperture transversely and as a fraction of the cell length longitudinally. In Figure 5.30 the influence of the denominator of the fractions on the number of accelerated particles are shown. When the grid is too coarse (black and red curve) the shape of the curve differs from the one with a finer grid. The values obtained are too low. Once the grid is fine enough the number of accelerated particles does not change, when the grid resolution is further increased. As a standard setting a denominator of 20 is used which makes $dr = \text{aperture}/20$ and $dz = \text{celllength}/20$.

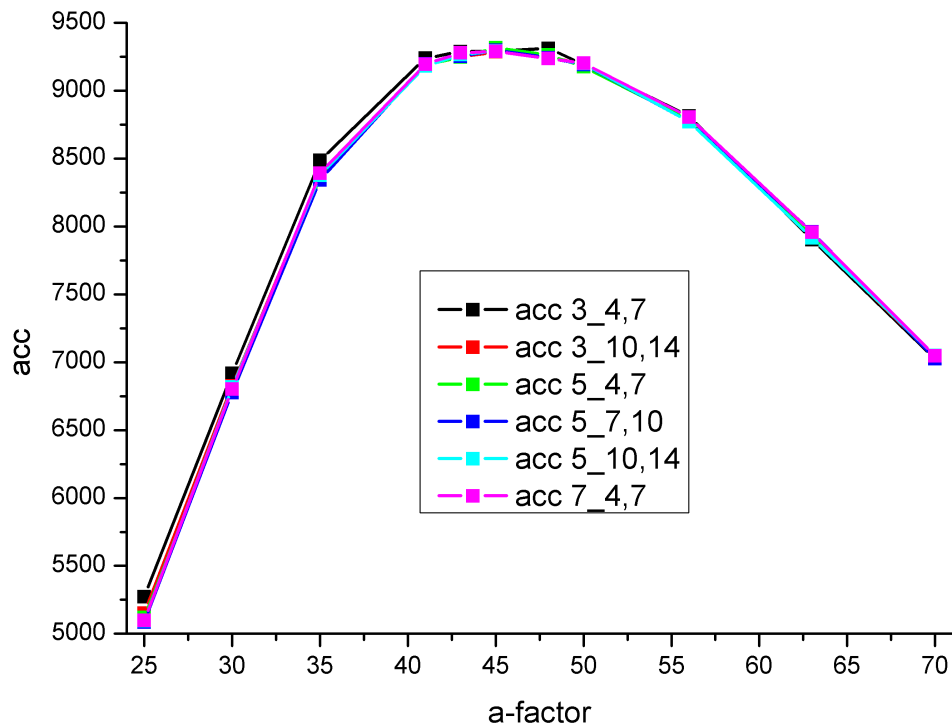


Figure 5.29: Influence of the number of multigrid iterations (first number) and smoothing cycles (second number and third for ratios of h_x/dz greater than 4) on the number of accelerated particles for the set of 11 test-RFQs.

5.3 Internal Field

As the next step, the space charge effect is now analyzed. First, routines are compared that do not take the influence of image charges on the electrodes into account. The first routine is the well known two dimensional SCHEFF routine (developed at Los Alamos National Laboratory), in which the beam is represented by charged rings and the effect of charged rings on rings can be calculated exactly analytically. The crux of SCHEFF is how well a three dimensional charge density can be mapped onto a two dimensional grid. The second routine used for comparison is PICNIC, a particle-in-cell approach based on numerical calculation of the interaction between cubes [PLN98]. The last routine is the multigrid Poisson solver whose implementation is a part of this thesis. The boundary of the mesh is a conducting cylinder with a radius of twice the maximum aperture and with zero potential. Calculation time is quite bad for PICNIC

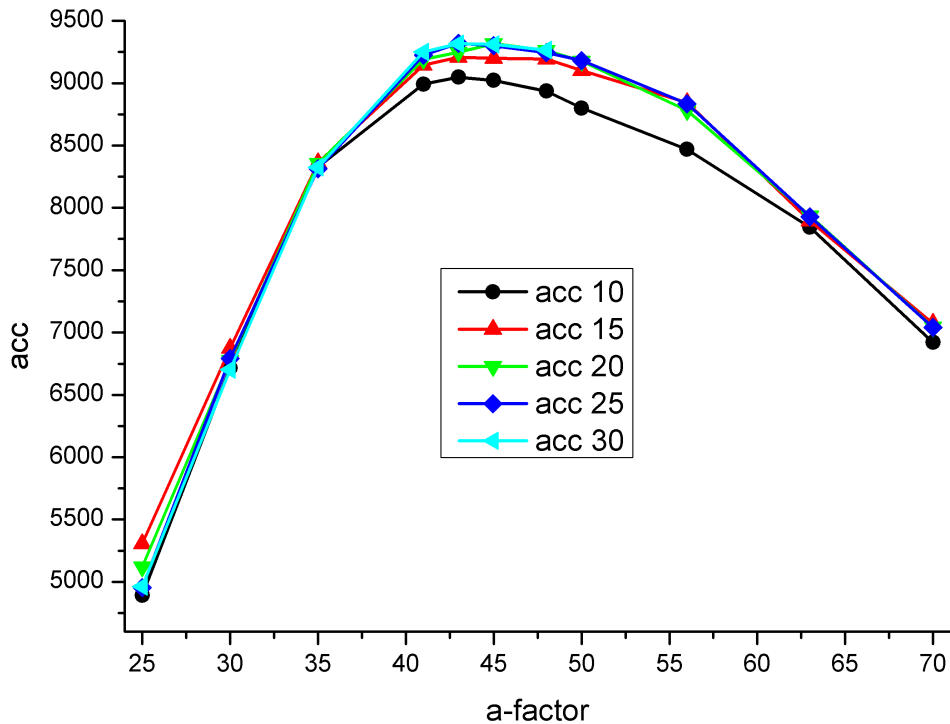


Figure 5.30: Number of accelerated particles as a function of the grid resolution ($dr=\text{aperture}/x$ and $dz=\text{cell length}/x$) for the set of 11 test-RFQs.

(5 h), it becomes better with the multigrid Poisson solver (30 min) and it is best for SCHEFF (10 min). Figure 5.31 shows the effect of the size of the grounded cylinder on the MG-transmission. There is a little influence within the range of 0.2%. In the MG routine the boundary conditions can easily be changed to have the shape of the electrodes in order to take the effect of image charges on the electrodes into account.

The first two space charge routines only consider a single bunch of particles. The effect of neighboring bunches is added later by superposition, thereby the neighboring bunches are treated as point charges and up to 20 leading and trailing bunches are taken into account in order to fully regard this effect. The multigrid Poisson solver uses its boundary conditions to take care of the neighboring bunch effect. The length of the space charge mesh is always set to twice the cell length with the bunch in its middle. The boundary is not mirrored, but kept periodic in the sense that the $n+1$ grid point and the first grid point have identical values. Doing so, the neighboring bunches are fully taken into account except for the slight effect of changing vane parameters.

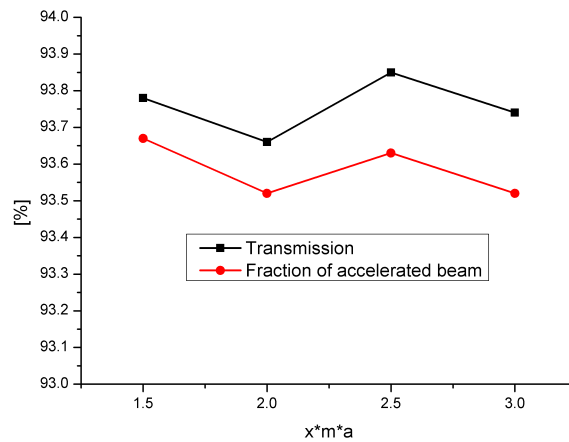


Figure 5.31: Influence of the radius of the zero potential cylinder for the multigrid Poisson solver as the space charge routine on the transmission.

5.3.1 Influence on Single Particle Dynamics

As for the external field an arbitrary particles was chosen and the space charge kicks on the particles from different space charge routines were logged as it travels through the quadrupole channel. In Figure 5.32 the evolution of the transverse space charge kicks from SCHEFF and multigrid Poisson solver without image charges is shown as well as the difference of the two (blue curve). The particle oscillates with its transverse phase advance through the bunch, the resulting kicks show this kind of oscillation as well. The phase advance is defined per focusing period and the geometric length of this focusing period increases with the energy of the particle. Hence the oscillation seems to be damped when plotting against the longitudinal z position. The shape of the curves from SCHEFF and from the Poisson solver are close, but the extrema are different. In the beginning (shown in Figure 5.33 in more detail) SCHEFF gives somewhat higher kicks than the Poisson solver does. At the end of the structure it is the other way around and the Poisson solver gives higher kicks. The micro structure of the curve, when the particle is at the edge of the bunch, is also very similar in the two curves. For this particle, which does not leave the bunch too far, the effect of images charges is minor.

The picture for the longitudinal kicks (Δp_z) is quite similar. The longitudinal kicks are shown in Figure 5.34. Again, the shape of the curves is quite the same, but the values from SCHEFF are higher for the whole structure. In the beginning of the

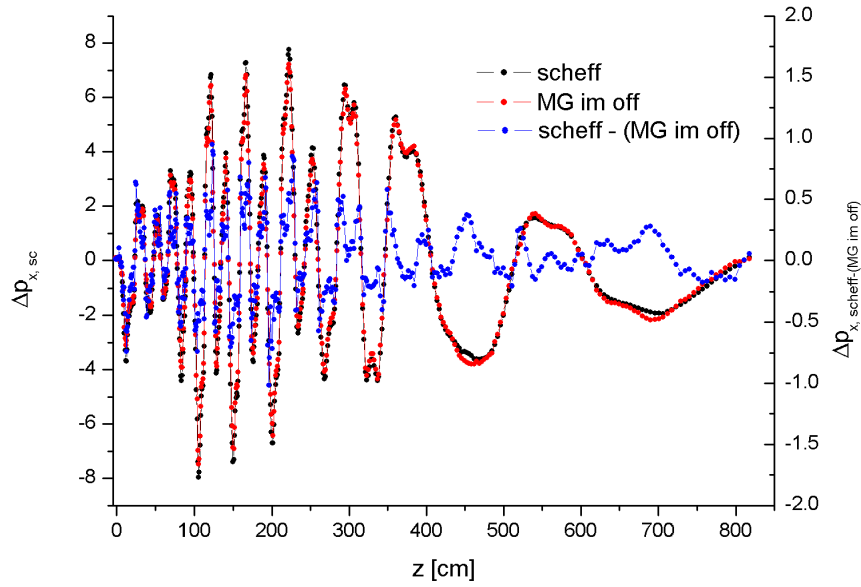


Figure 5.32: Transverse space charge kicks from SCHEFF and multigrid Poisson solver without image charge effect and the difference of the two (SCHEFF-MG) along the RFQ.

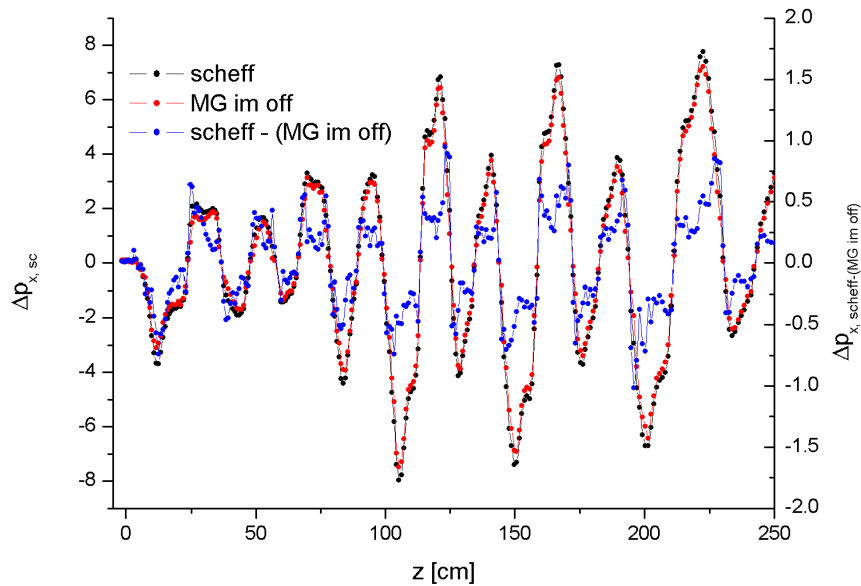


Figure 5.33: Transverse space charge kicks from SCHEFF and multigrid Poisson solver without image charge effect and the difference of the two (SCHEFF-MG) for the first 2.5 m of the RFQ.

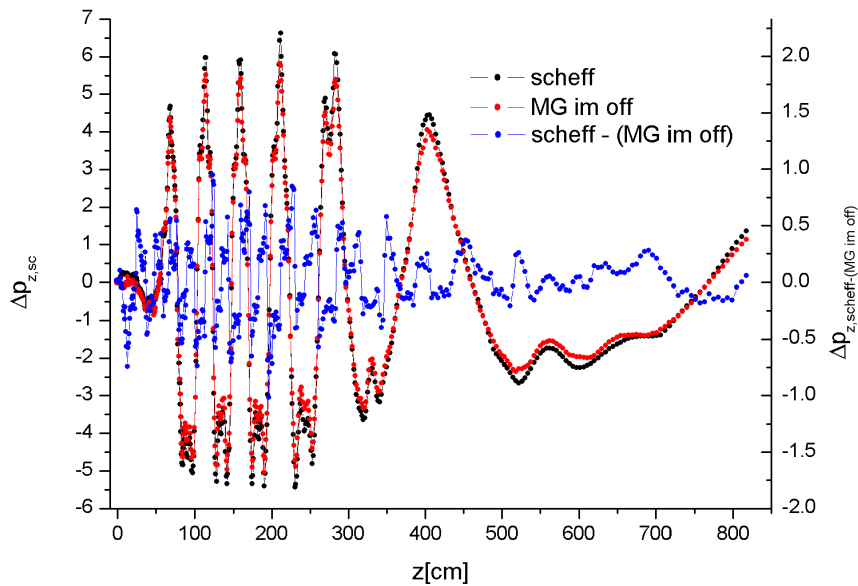


Figure 5.34: Longitudinal space charge kicks from SCHEFF and multigrid Poisson solver without image charge effect and the difference of the two (SCHEFF-MG) along the RFQ.

RFQ the effect of space charge on the longitudinal dynamic of the beam is small, because the input beam is DC and longitudinal forces cancels. This changes when the beam becomes bunched.

5.3.2 Collective Effects

To compare the influence of the routines used to calculate the space charge effect on the transmission, the set of RFQs was simulated using the same MG-routine for the external field. The settings for the mesh in terms of the resolution of the mesh for SCHEFF and for the Poisson solver were chosen equal. For PICNIC two different settings were used (one with the longitudinal grid extent set at ± 3.5 times the longitudinal rms beam size including smoothing, and with 5 times excluding smoothing). The transmission curves for different space charge routines as a function of the aperture-factor are shown in Figure 5.35. Roughly, the shape of the curves are similar. The peak of the transmission curves does not depend on the chosen space charge routine. So finding the optimum is independent of the routine used in this case. Overall, SCHEFF gives the lowest transmission for every RFQ, but the difference to the

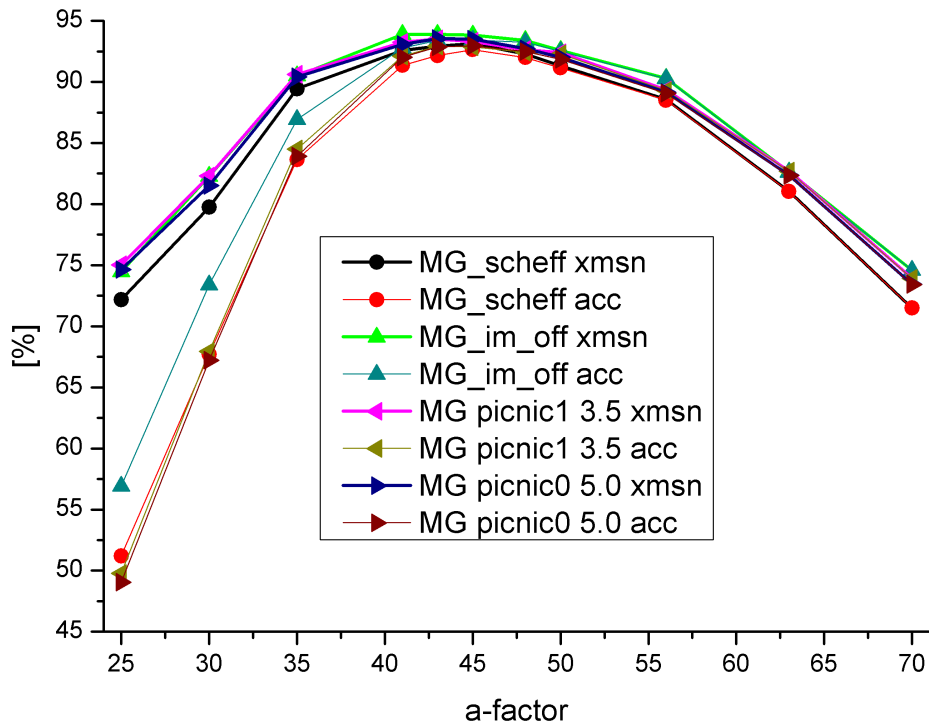


Figure 5.35: Transmission (xmsn) and percentage of accelerated beam (acc) for different routines for the internal field without image charges for the set of 11 RFQs (MG: multigrid Poisson solver; im off: image charge effect turned off).

other routines becomes smaller at the peak. For the RFQs with a small aperture (big a-factor) the routines PICNIC with both settings and the multigrid Poisson solver the results are very close, only SCHEFF is 2.5% lower. On the right hand side of the plot the situation is the same. In the middle with already high values for the transmission the multigrid Poisson solver gives the highest results and stays high longer than the other curves leading to a flatter plateau. The percentages of accelerated beam for SCHEFF and PICNIC are very close over whole range, only the Poisson solver gives higher values for RFQs with big apertures. The 3D PICNIC should be more correct than SCHEFF, and the longitudinal boundary condition of the MG routine may be more accurate than the SCHEFF/Picnic point-to-point neighboring bunch treatments. So it appears justified to assert that the MG Poisson solution is preferred.

5.3.3 Sensitivity of the Poisson Solver

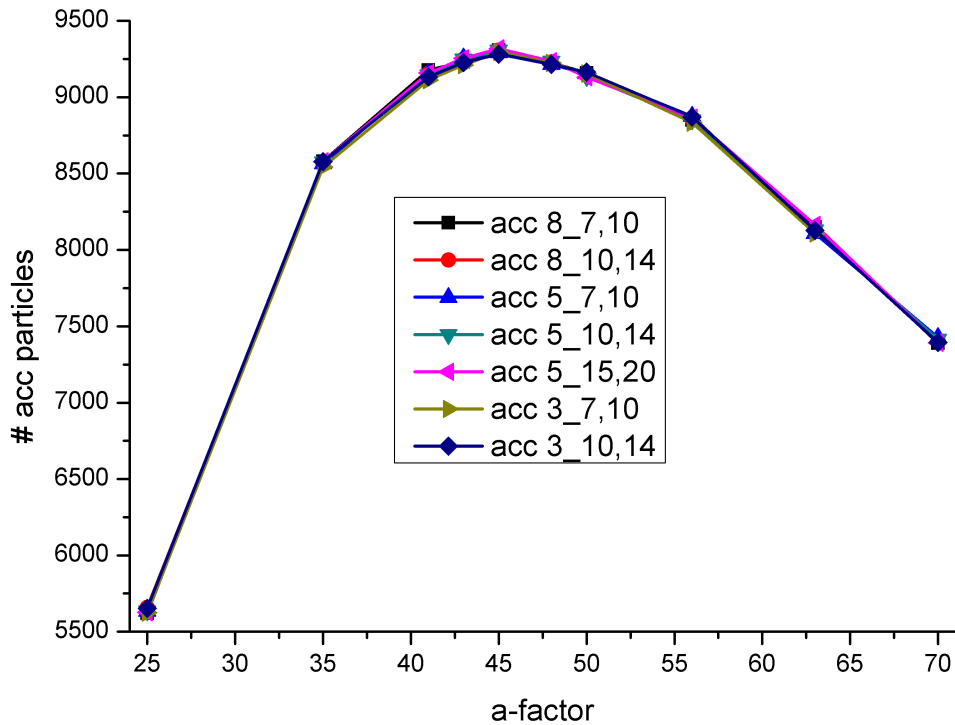


Figure 5.36: Influence of the number of multigrid iterations (first number) and smoothing cycles (second number and third for ratios of h_x/d_z greater than 4) on the number of accelerated particles for the set of 11 RFQs.

The sensitivity of the Poisson solver has already been analyzed for the external field which does not include a charge density on the grid. Because this has changed for the internal field calculation, the sensitivity of the Poisson solver is analyzed again but with a charge density introducing the field. Figure 5.36 illustrates the effect of the number of multigrid iterations and the number of smoothing cycles on the number of accelerated particles. All used settings produce similar curves which lie within 1%. The standard settings are 5 multigrid iterations and 7 (10 for the ratio of dr/d_z greater than 4) smoothing cycles per grid (blue curve).

The influence of the grid resolution on the number of accelerated particles is shown in Figure 5.37. It is stronger than the influence of the number of multigrid iterations. With increasing grid resolution (from black to blue) the number of accel-

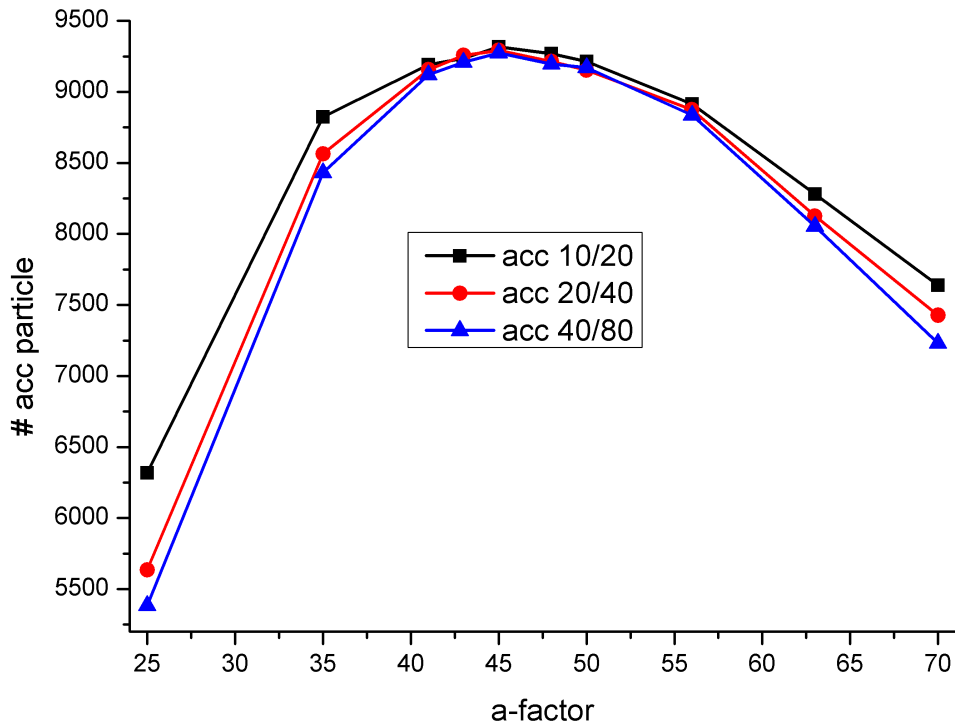


Figure 5.37: Number of accelerated particles as a function of the grid resolution (dr =aperture/ x and dz =cell length/ y) for the set of 11 RFQs.

erated particles decreases on both sides of the curve (small and large apertures) and at the optimum for medium apertures the effect is much smaller and the values are similar for the different settings. The red curve (dr =aperture/20; dz =celllength/40) is a good compromise between running time and accuracy and is therefore chosen as the standard settings for the solver.

5.3.4 Space Charge with Image Charge Effect

Now the influence of image charges on electrodes introduced by the beam will be determined. The same multigrid Poisson solver is used for the space charge calculation, with different boundary conditions as the only difference. For neglecting the image charge, the transverse boundary of the grid is again a grounded cylinder with the radius of twice the maximum aperture. Image charges are introduced to force the potential on the conducting surfaces to a certain value. In the case of the electrodes

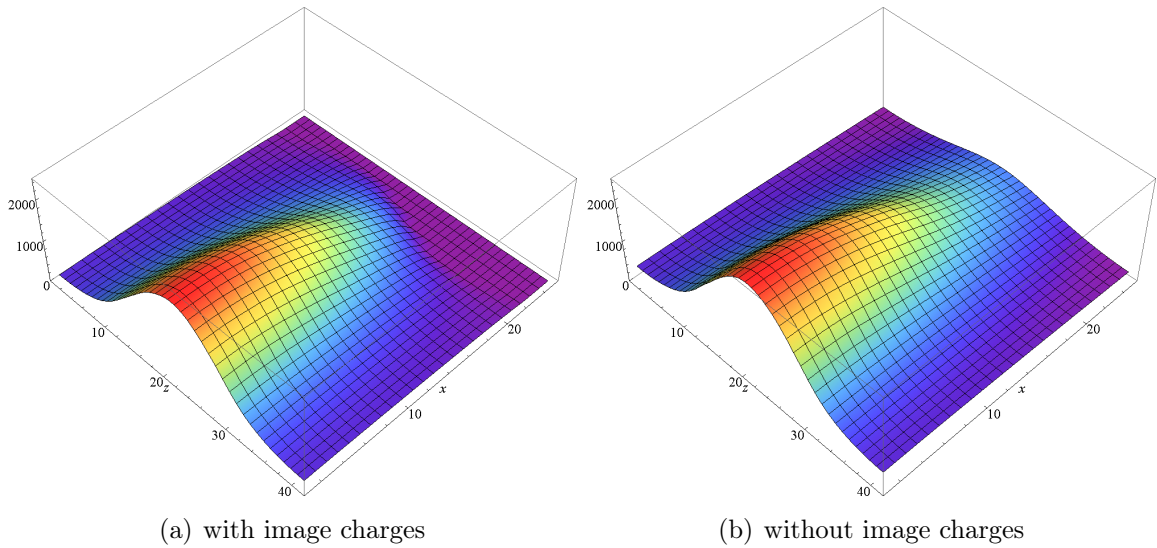


Figure 5.38: Space charge potential at a xz -plane with and without image charges.

of an RFQ the potential on the electrodes has to vanish, because the internal and the external fields are treated separately and are combined by superposition.

The potential with and without image charges in the xz -plane of certain cell in an RFQ is shown in Figure 5.38. On the left plot the position of the vane can be seen as the region where the potential is equal to zero. The potential on the other plot falls off smoothly. The shape of the two potentials along the beam axis are quite similar. The maximum of the potential is in the region where the majority of the particles is located.

The x -component of the potential is shown in Figure 5.39. In the center of the bunch, at the middle of the z -axis, the E_x increases linearly to its maximum and then falls off for the case without the image effect (right picture) or increases further after a small plateau to maximum in front of the vane for the case with image charges. On the axis the transverse electric field vanishes as expected. The field in front of the vane is not very smooth and some steps are present, because of the shifted grid points. Shifted grid points are not shifted for plotting and the effect is therefore smaller than it appears, so the roughness there does not have any influence on the beam dynamic, furthermore particle entering the electrodes are considered lost. The picture indicates that the effect of image charges on the electrodes can be quite strong for particles leaving the core.

In Figure 5.40 the corresponding longitudinal field E_z is shown. In the middle

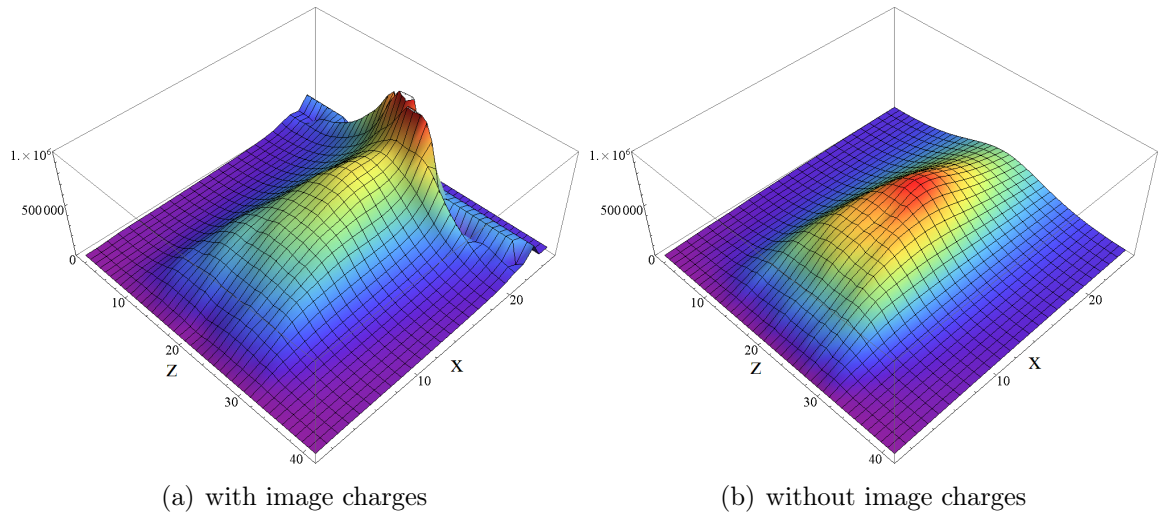


Figure 5.39: Transverse field E_x from space charge at a xz -plane with and without image charges.

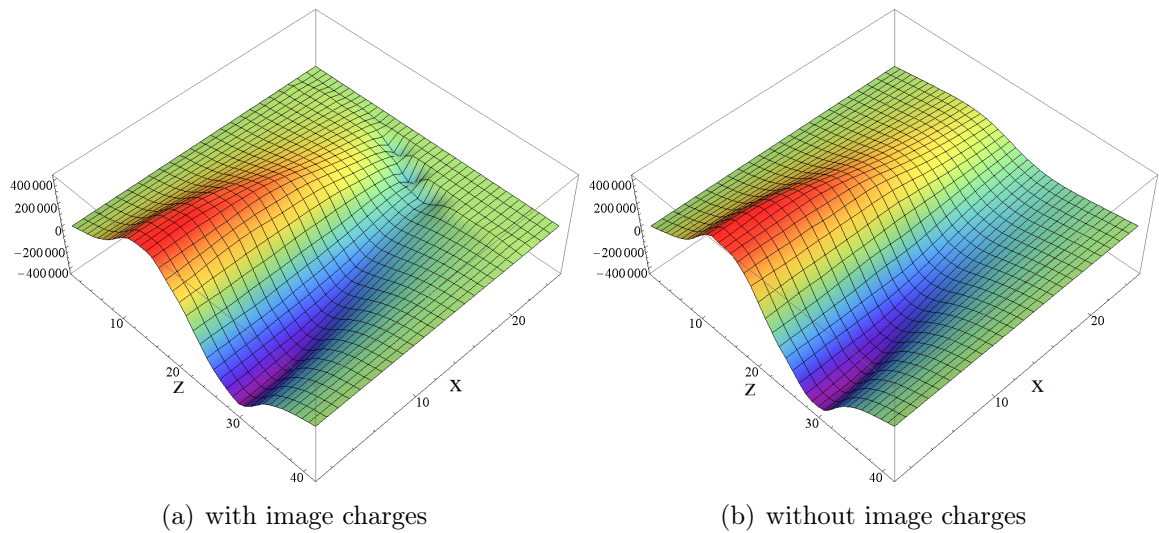


Figure 5.40: Longitudinal field E_z from space charge at a xz -plane with and without image charges.

of the bunch, E_z is zero as expected and changes its value in both directions linearly toward its extrema to fall off to zero again. The transition from vacuum to the vane looks more rough and stepped than it actually is, because the plotting routine does not take the shift of the grid points inside the electrodes into account.

The relative difference between the longitudinal field E_z with and without image charges on the electrodes is shown in Figure 5.41. At the center of the bunch

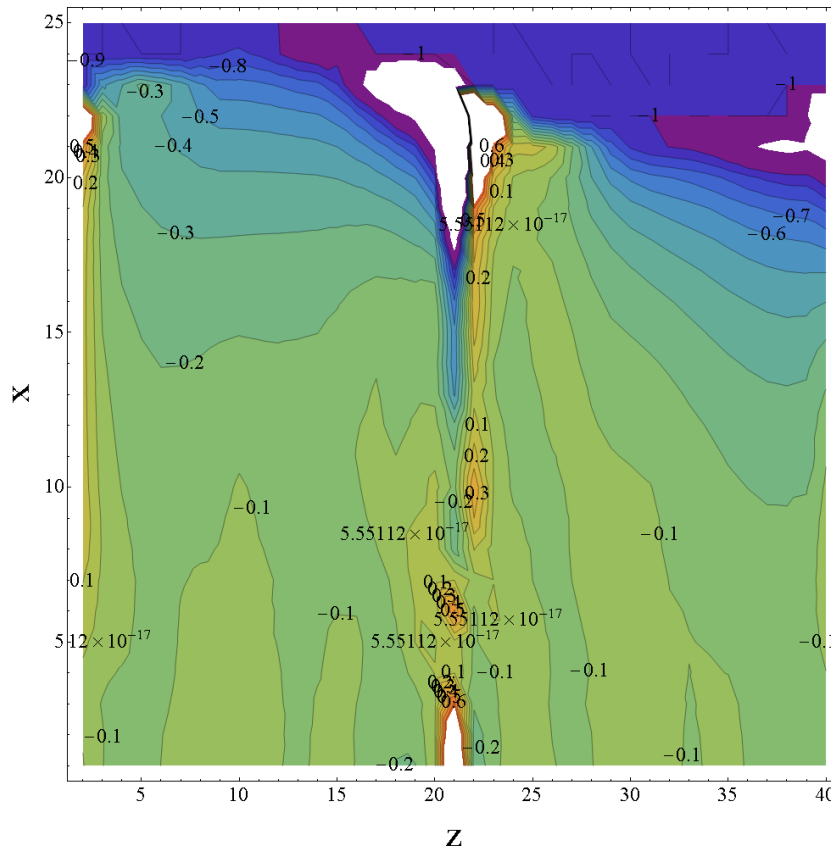


Figure 5.41: Relative difference $(\text{IMON}-\text{IMOFF})/\text{IMOFF}$ of the longitudinal field E_z with and without image charges in the xz -plane.

E_z is zero and the relative values can become quite big. Beside that, the field with image charge effect is as high as 10% in the useful zone at the beam axis. In front of the electrodes the difference is quite big.

The influence of image charges placed on the surface of the electrodes on the results of the simulation in terms of transmission and fraction of accelerated particles for the set of RFQs is shown in Figure 5.42. The (black, red) curve is a result of a simulation using the full multigrid Poisson solver without image charges (grounded cylinder with a radius of twice the maximum aperture), which has already been compared to in the examination of the pure space charge effect. For the runs with image charges (blue, green) the same settings are used, but the boundary conditions of the space charge Poisson solver was changed from the cylinder to the shape of the electrodes. Including the image charges significantly lowers the transmission for all simulated RFQs with some dependence of the aperture. For big apertures (left

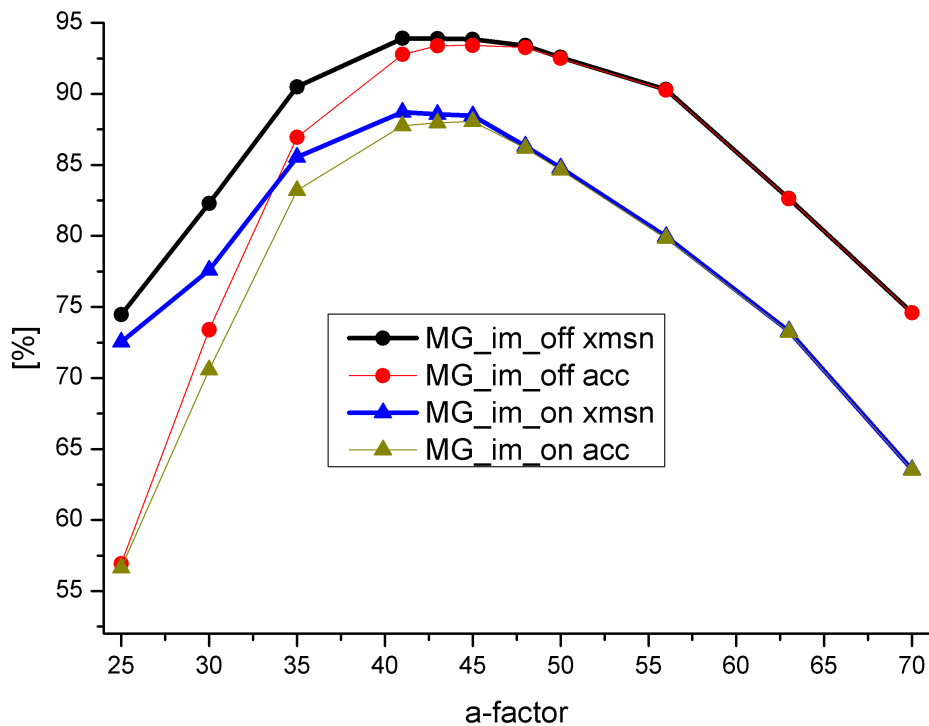


Figure 5.42: Transmission (xmsn) and percentage of accelerated beam (acc) illustrating the effect of image charges on the electrodes for the set of 11 RFQs.

hand side) the effect of image charges is smaller than for the small apertures on the right hand side. This holds especially for the fraction of accelerated particles. The position of the maxima as well as the basic shape of the curve has not changed with the image charges. The difference for the best transmitting RFQs is about 5% and increases for decreasing apertures to about 10%. This is a bigger effect than implied by other (less accurate) routines (<2% in transmission) used in PARMTEQM for instance [CWY⁺05].

To explain why the effect is stronger for smaller apertures, the percentage of particles are plotted as a function of their minimum distance to the electrodes along the structure in Figure 5.43. In the RFQ with a medium aperture (black curve) only a few percent of the transmitted particles come closer to the electrodes than 10% of the aperture. For an RFQ with a smaller aperture, 15% of the particles come closer to the electrodes than 10% of the aperture. Closer than 20% of the aperture come 20% of the particles for the medium aperture and more than 40% for the small aperture.

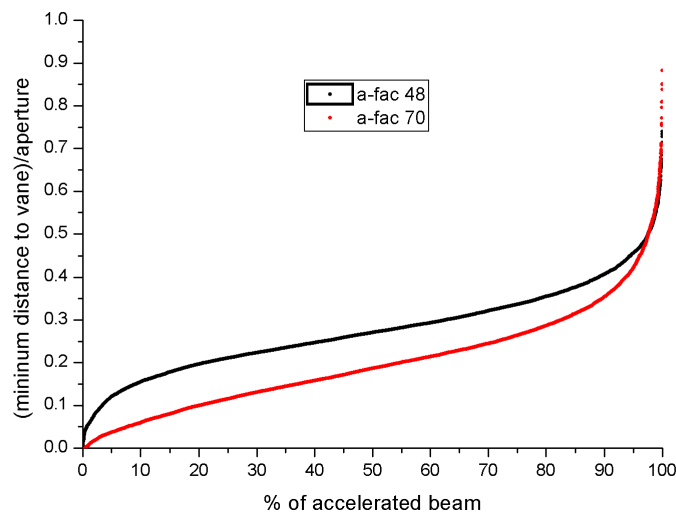


Figure 5.43: Minimum distances of the particles to the vane as a function of the percentage of the beam that was accelerated.

For both RFQs the number of particles staying more than 40% of the aperture away from the electrodes is very small. So the number of particles entering the region where the effect of image charges has a strong influence on the field increases with smaller apertures. Also the image charge effect is stronger in those cases, since the distance between the beam introducing the image charges and the surface of the electrodes is small. Because of the opposite charge of the image charges the image charge effect is always defocusing in the transverse plane, but might have a small longitudinal focusing effect on particles in front or behind the bunch. Summing up, a small aperture will increase the strength of the image charge effect compared to a big aperture in two ways and gives therefore an explanation of why the image charges on the electrodes have such a strong influence on the transmission especially for small apertures.

This strong effect has not been predicted by other simulation programs e.g. PARMTEQM, which uses some approximations to calculate the influence of image charges on the beam. For precise simulations of high current RFQs which are dominated by space charge forces, it is necessary to include the image charge effect as accurate as possible. This can not be done by using some approximations, but it can be simulated by using a 3D (multigrid) Poisson solver taking the exact boundaries in form of the electrodes into account. Simulating the image effect correctly, helps

to improve designs especially for high current, high frequency applications with small apertures and when losses in the high energy part of the RFQ need to be minimized to reduce radiation and to avoid activation of the machine.

This finding that the image forces in RFQs are stronger than previously thought helps to resolve the observation that actual RFQs have usually demonstrated lower transmission than predicted by simulation programs using approximate methods [Jam97].

6 Experiments with the MAFF RFQ

In the previous chapters work on particle dynamic simulations has been presented. For designing and building RFQs the particle dynamic is only one part that needs to be taken care of. Other issues are the selection and the design of the resonance structure (see 2.2 for an overview of different resonator concepts), the precise manufacture and the assembling of the resonator as well as the tuning and the commissioning of the RFQ. The following chapter deals with the commissioning and beam test of an RFQ. The particle dynamic codes described in the first part of the thesis have been used to test a given design of an RFQ under different conditions like unflatness, influence of the input emittances, variation of the input energy et cetera. They are important tools to understand the behaviour of the particles inside the structure especially for error diagnostics and to eliminate the electrode layout as possible source of errors. So the quantities which have been simulated are now measured at a real structure.

The Munich Accelerator for Fission Fragments (MAFF) was a plan for a Radioactive Ion Beam (RIB) facility in Munich which was designed to use thermal neutrons from the FRM-II to produce radioactive ions and to accelerate them for various experiments. Most other RIB facilities use a driver accelerator to produce radioactive ions. MAFF was designed to accelerate very neutron-rich fission fragments to a final energy from 3.7 up to 5.9 MeV/u. The beam intensity was limited to $3 \cdot 10^{11}$ particles per second [HGA⁺03]. The machine was planned to be used for the creation of super-heavy elements ($100 \leq Z \leq 120$) by fusion reactions, nuclear spectroscopy of exotic nuclei and for other applications e.g. medicine.

The radioactive ions are produced by thermal neutrons induced fission of ^{235}U at a large cross section of 580 b. The production target consists of porous graphite loaded with $^{235}\text{UC}_2$ which is enclosed in a rhenium container with an inner lining of vitreous carbon. The produced ions have a charge of one. For a sufficient acceleration

a higher charge to mass ratio and therefore higher charge stages are needed. Charge breeding can be done in either an electron beam ion source (EBIS) or electron cyclotron resonance ion source (ECRIS). For the MAFF project a maximum charge to mass ratio of 6.3 was projected. The planned linac has a total length of about 20 m and contains an IH-RFQ, three IH-structures and two identical 7-gap IH-resonators for energy variation. It runs with a duty factor of 10% at a frequency of 101.28 MHz in the first section and with 202.56 MHz in the high energy part. The energy variation is done by turning the last IH-structure on and off and by using the last 7-gap structure either to accelerate or to decelerate the beam. The energy spread at the target is designed to be less than 0.2%. Over all, the MAFF linac is in low-energy part very similar to the REX-ISOLDE linac [HAA⁺01], [HKS⁺98], [HKB⁺97].

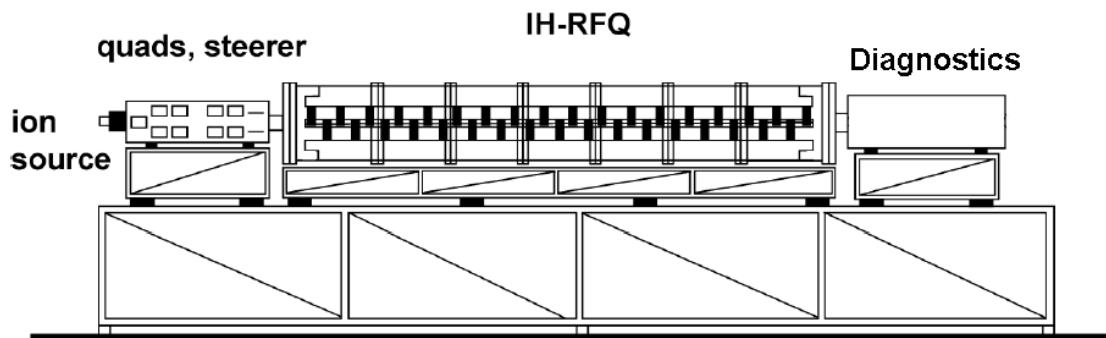


Figure 6.1: Scheme of the test stand [BHF⁺06].

The concept of the RFQ for MAFF differs from many other projects since it uses an IH-type cavity. Using an IH-type cavity should lead to a higher R_p -value, which is a measure for the efficiency of transforming RF power to accelerating voltage, compared to a 4-Rod structure like the REX-ISOLDE RFQ [SKH01]. The IH-RFQ cavity is excited in the TE_{111} -mode. The first IH-RFQ is the 36 MHz high current injector (HSI) at GSI [Rat98]. The particle dynamics layout of the MAFF RFQ is very similar to the REX-ISOLDE RFQ [Sie01]. It is designed to accelerate particles with a mass to charge ratio of 6.3 from 3 keV/u to 300 keV/u with a maximum intervane voltage of 70 kV. The structure with a length of 289 cm is divided into 7 individual modules to allow fabricating the structure from bulk copper in order to increase rf performance. The five inner modules are identical with a length of 400 mm and the two end-modules have a length of 425 mm [PKHS]. The parts of the RFQ have been manufactured at NTG Gelnhausen and the assembly took place at IAP in Frankfurt, because the plan to build MAFF was abandoned, but the RFQ will be used for other

applications. A first test stand was build in order to measure the performance of the machine (Figure 6.1) [BHF⁺06]. As an ion source a filament driven volume ion source [MPJ⁺00] has been set up followed by a electrostatic quadrupole triplet and horizontal and vertical steerer. A helium beam (He^{+1}) has been used, because mass to charge ratio lies in the range of the accelerator and the ion source produces only one charge state and one isotope.

6.1 Basics of RF-Structures

This section gives a short overview of RF parameters that are important in accelerator context. The parameters will be used in the description of the experiments at the MAFF IH-RFQ to describe the RF-structures: resonance frequency f , quality factor Q and impedance.

6.1.1 Quality Factor Q

Resonators are oscillatory systems in which electric currents are excited by an injected RF of a certain frequency f_0 on the surface of the structure. In real systems energy is dissipated during the oscillation. The amount of energy, which dissipates during one period, is described by the quality factor Q_0 . The quality factor is defined by

$$Q_0 = \frac{\omega W}{P}, \quad (6.1)$$

where ω is the angular frequency, W the energy stored in the resonator and P is the dissipated power or the dissipated energy times the period T . Typical values for the quality factor of normal conducting resonators are between 10^3 and 10^5 and for superconducting resonators between 10^8 and 10^{10} (in the frequency range 20 – 400 MHz) [Pod08]. Since the skin depth decreases with higher frequencies, the volume in which the current flows and therefore the quality factor also decrease.

Coupling RF into an resonator structure and varying the frequency around the resonance frequency, the resonance curve can be obtained (Figure 6.2). The amplitude of the electric and magnetic field as the function of the frequency can then be described with the Lorentz-curve, which is given by:

$$|A(\omega)| = \frac{|A_0|}{\sqrt{1 + Q_0^2(\Delta\omega/\omega_0)^2}}, \quad (6.2)$$

where $A(\omega)$ is the amplitude of the field at the frequency ω , A_0 is the amplitude of the field at the resonance frequency ω_0 , and $\Delta\omega = 2(\omega - \omega_0) = \omega_2 - \omega_1$ is twice the difference between the driving and the resonance frequency. It has to be noted that Q_0 is the intrinsic or unloaded quality factor. This means that all losses take place in the resonator and coupling effects of the coupling loop and losses in the amplifier and beam loading are neglected. They will be considered in the external quality factor. To measure the quality factor of a resonator the so called “3-dB-method” can be used.

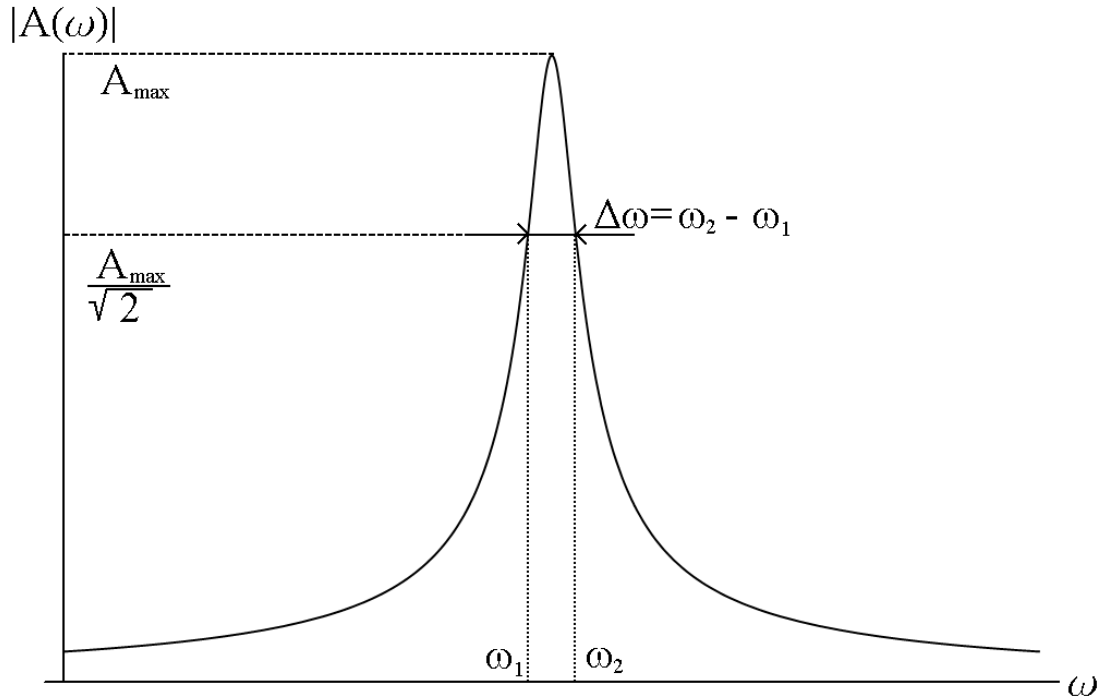


Figure 6.2: Shape of a resonance curve around the resonance frequency ω_0 . The quality factor can be determined by the width of the resonance curve where the amplitude has decreased by a factor of $\sqrt{2}$.

The RF characteristics of a resonator can be approximated by three parameters: shunt resistance R , capacitance C , and inductance L which form a parallel resonant circuit (Figure 6.3). The quality factor can be rewritten:

$$Q_0 = \omega_0 \frac{W}{N} = \omega_0 \frac{\frac{1}{2}LI_L^2}{\frac{1}{2}RI_R^2} = \omega_0 \frac{\frac{1}{2}L \frac{U^2}{\omega_0^2 L^2}}{\frac{1}{2}R \frac{U^2}{R^2}} = \frac{R}{\omega_0 L} = \omega_0 CR \quad (6.3)$$

The impedance Z of a parallel resonant circuit can be calculated from the single

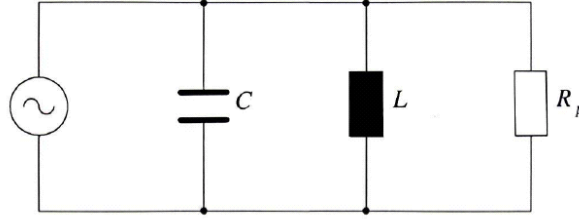


Figure 6.3: Equivalent parallel resonance circuit [Bec97].

impedances following

$$\frac{1}{Z} = \frac{1}{Z_r} + \frac{1}{Z_c} + \frac{1}{Z_L} \quad (6.4)$$

$$= \frac{1}{R} + j \left(\omega C - \frac{1}{\omega L} \right). \quad (6.5)$$

In the case of a resonance the impedance becomes maximal and $\omega C = 1/\omega L$, which leads to the Thomson formula $\omega_0 = \frac{1}{\sqrt{LC}}$. At the resonance frequency ω_0 the conductance value $Y = 1/Z$ becomes real and the phase shift between the current and the voltage vanishes. To determine the width of the resonance curve the frequency is varied with $\delta\omega$ around ω_0 in equation 6.5 and substituted in equation 6.3:

$$\frac{1}{Z} = \frac{1}{R} + j \left(\omega_0 C + \delta\omega C - \frac{1}{\omega_0 L} + \frac{\delta\omega}{\omega_0^2 L} \right) \quad (6.6)$$

$$= \frac{1}{R} \left(1 + 2j \frac{\delta\omega}{\omega_0} Q_0 \right) \quad (6.7)$$

$$\frac{1}{\text{Re}(Z)} = \frac{1}{R} \sqrt{1 + 4Q_0^2 \left(\frac{\delta\omega}{\omega_0} \right)^2} \quad (6.8)$$

When the frequency is changed by $\frac{\delta\omega}{\omega_0} = \pm \frac{1}{2Q_0}$ away from the resonance frequency the amplitude of the voltage has decreased by a factor of $\frac{1}{\sqrt{2}}$ and the power has decreased by $\frac{1}{2}$. Now the quality factor can be written as

$$Q_0 = \frac{\omega_0}{2\delta\omega} = \frac{\omega_0}{\Delta\omega} = \frac{f_0}{\Delta f}, \quad (6.9)$$

where $\Delta\omega$ and Δf were the frequency variation when the voltage has dropped by a factor of $\frac{1}{\sqrt{2}}$ which is on a logarithmic scale $20 \lg \frac{1}{\sqrt{2}} \approx -3$ dB [Fis07].

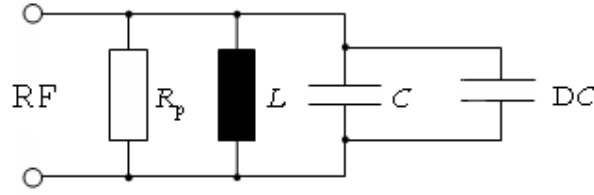


Figure 6.4: Equivalent circuit of RFQ and perturbation capacitance.

6.1.2 Shunt Impedance

The shunt impedance or R_p -value is a second important RF parameter of RFQ type structures. It correlates the maximal Voltage U_{max} at the vane tips to the average dissipated power \bar{N} .

$$R_{p,0} = \frac{U_{max}^2}{\bar{N}}. \quad (6.10)$$

In the stationary case the average dissipated power is equal to the power delivered from the amplifier with no beam loading. Therefore the shunt impedance is a direct measure of the efficiency of the structure to convert RF power into an electric field between the electrodes. High $R_{p,0}$ -values correlate to high efficiency. With

$$R_p = \frac{Q}{\omega_0 C} \quad (6.11)$$

the R_p -value depends on the total capacity of the electrodes and is therefore a length dependent value, since the total capacity increases with longer electrodes. In order to compare RFQs of different lengths a parameter is necessary which does not depend on the length of the RFQ. Often the R_{pL} -value is used

$$R_{pL} = R_p \cdot L \quad [\Omega m]. \quad (6.12)$$

The shunt impedance of an RFQ resonator can be measured by adding a small known perturbation capacitance onto the electrodes [Sch90]. The equivalent circuit is shown in figure 6.4. The resonance frequency then changes to

$$\omega_0^* = \omega_0 - \Delta\omega = \frac{1}{\sqrt{L(C + \Delta C)}}. \quad (6.13)$$

This can be rewritten as

$$\frac{\Delta\omega_0}{\omega_0} = \frac{\Delta W}{W} = 1 - \frac{1}{\sqrt{1 + \frac{\Delta C}{C}}} \approx \frac{\Delta C}{2C}. \quad (6.14)$$

Making use of the definition of the quality factor and the shunt impedance the equation can be rewritten

$$R_p = \frac{2Q\Delta f}{\pi f_0^2 C_s}. \quad (6.15)$$

The factor 2 in the numerator of R_p -value is necessary, because the vane voltage of the RFQ is measured as the amplitude of the voltage and the RF power is measured in rms terms. The perturbation capacitance has to be small compared to the capacity of the electrodes. Typical values for the capacitance of the electrodes for a four rod RFQ are between 80 and 120 pF/m. Capacitances of 1 pF, which are the smallest commercial capacitances, have rather big production variation of 20% [Mül09]. With suitable calibration the influence of the production variation can be reduced [Sch90].

6.2 Measurement of Shunt Impedance

Since no accelerated beam was measured after the IH-RFQ with the setup described above [ZBH⁺08], the following measurements were done in order to find out if the reason for this behaviour is caused either by the setup and operation of the machine or by the layout of the particle dynamics. First step was to measure the actual condition of the machine to eliminate construction problems. The shunt impedance was measured to make sure that the intervane voltage of the IH-RFQ is high enough to not only transport particles, but to accelerate them as well with the given power amplifier. The second step was to measure the energy spectrum of a proton beam in order to assure that the IH-RFQ can accelerate at a lower intervane voltage. Next step was to measure the transmission of the IH-RFQ and to compare the results with simulations.

The shunt impedance of the IH-RFQ was measured directly with two different methods. One method uses a perturbation capacitor and the other one uses gamma spectroscopy to determine the intervane voltage by a given RF power; equation 6.10 then gives the shunt impedance.

6.2.1 Perturbation Capacitor

First, the shunt impedance was measured with a perturbation capacitor at low RF power levels. Since the error of the small capacitors used to perturbate the field varies, three different capacitors have been used for the measurement. The resonance frequency is 104.688 MHz with a quality factor Q_0 is 5980. The R_p -values vary between 45 k Ω and 50 k Ω (see equation 6.15); the error is 25% (5% from the quality factor and 20% from the perturbation capacitor and the frequency measurement). Table 6.1 gives an overview of the measurements. Because of the big error of the measurement, another method was used to determine the shunt impedance.

Capacitor	1	2	3
Δf [MHz]	0.143	0.136	0.13
R_p [k Ω]	48	46	45
Shunt impedance [k Ω m]	150	142	136

Table 6.1: Shunt impedance measurements with three different capacitors.

6.2.2 Gamma-Spectroscopy

Second, the shunt impedance was measured at a high RF level, by measuring the intervane voltage and the RF power level. The RF power in the structure was measured using a coupling loop, which was calibrated at low RF levels and the voltage was measured by gamma spectroscopy. The bremsstrahlung of electrons is measured which are produced by residual gas ionization. Depending on the phase of the RF and the location of ionization the electrons can see a maximum voltage of $\pm U_0/2$, which oscillates sinusoidal, when they are produced at one electrode and then accelerated toward an adjacent electrode where they hit the copper and produce bremsstrahlung. The expected spectrum is a continuous γ -spectrum. For measuring the bremsstrahlung a semiconducting detector was used. The detector was calibrated with an Am^{241} -probe, which emits photons with an energy of 59.6 keV and 26.4 keV.

The first measurement of the bremsstrahlung spectrum of the RFQ was done with an RF power of 32 kW (Figure 6.5). The maximum energy of the photons is between 28 keV and 30 keV. The corresponding R_p -values are 24.5 and 28 k Ω .

Since this value was so much lower than expected, it seemed likely that the structure had some kind of problem. Up to that point, the IH-RFQ was equipped with four tuning plates to capacitively adjust the flatness and resonance frequency

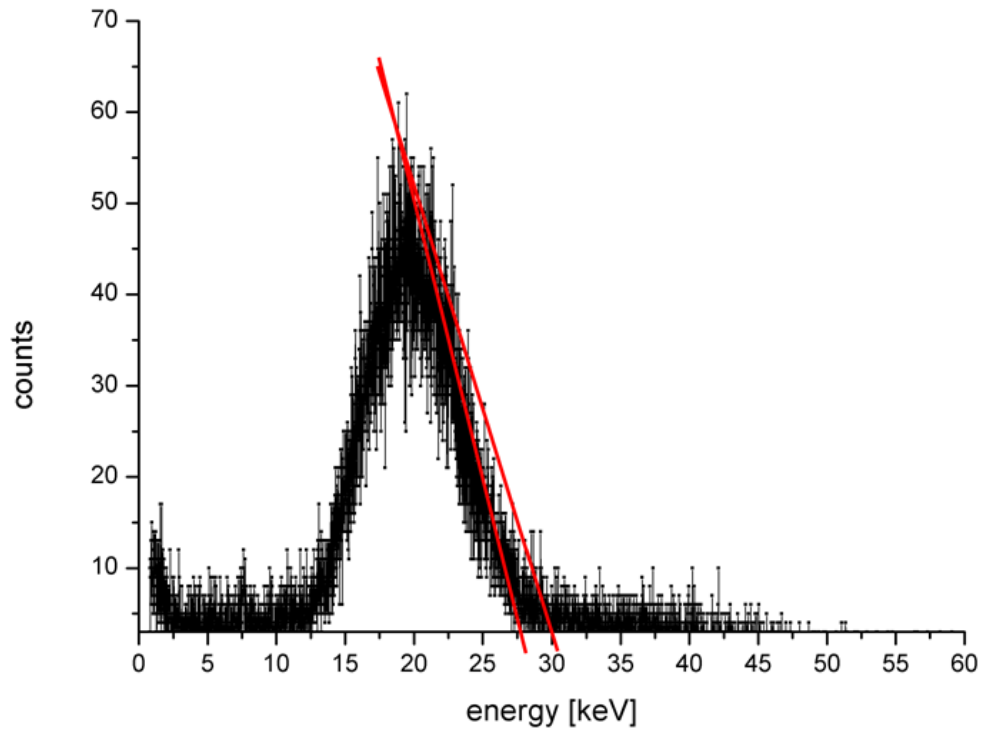


Figure 6.5: γ -Spectrum of IH-RFQ with RF power of 32 kW with tuning plates mounted inside the structure.

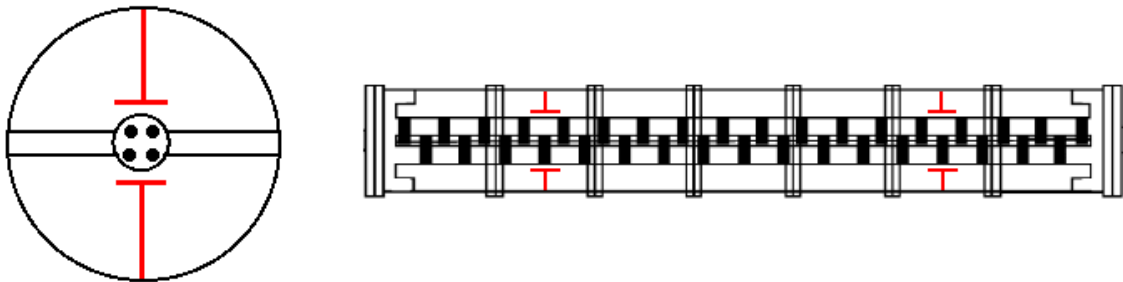


Figure 6.6: Scheme of the IH-RFQ with tuning plates (red).

(Figure 6.6). It was observed that the stamps of these tuning plates became quite warm during operation. After the removal of the tuning plates the R_p -value of the structure had increased. Figure 6.7 shows the spectrum without the tuning plates. A maximal photon energy between 32.5 keV and 38 keV was determined, corresponding

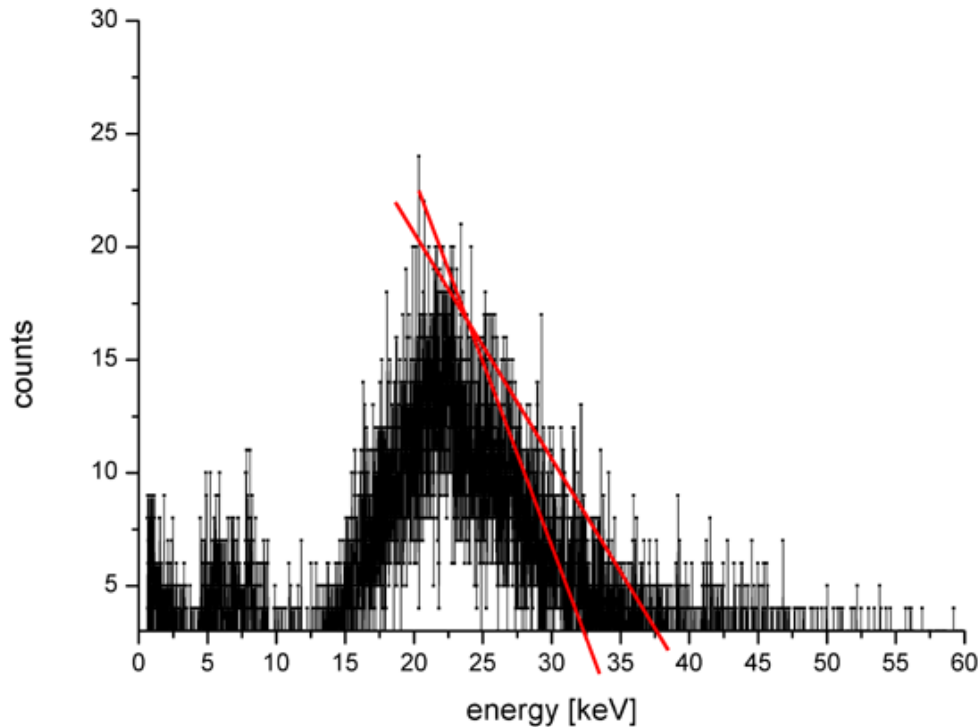


Figure 6.7: γ -Spectrum of IH-RFQ with RF power of 30 kW after removing the tuning plates.

R_p -values are 35 k Ω and 48 k Ω . The values vary much, because the RF amplifier was at this point not able to produce and transmit a stable RF power amplitude to the resonator and because of discharges and a thermal drift of the resonator. The error of the R_p -value measurements are typically between 5 and 10% due to the precision of the RF power measurement and to the field measurement in the resonator. In our measurements the unstable RF power amplitude increased to error additionally, but the R_p -values are clearly below the expected.

6.3 Measurement of the Output Energy

First beam tests have only shown a output beam current of 8 μ A with an input current of 1 mA and it was not known, whether the beam has only be transported trough the RFQ or has been accelerated to the design output energy of the RFQ [ZBH⁺08]. As the next step an energy spectrum of the RFQ was measured. A proton beam was chosen

for this purpose, because of the lower required intervane voltage and therefore lower RF power. The electrostatic lens system was suspected to cause a high beam loss for protons and the question of alignment was never satisfactorily answered. Therefore, the ion source was mounted directly in front of the RFQ. Simulations of this scenario predicted a proton transmission of only 10%. For measuring an energy spectrum a low transmission is no problem. The energy measurement was done using a dipole magnet and a Faraday cup. A straightforward plot is the exciting current of the dipole magnet versus the current on the cup. The magnet is sensitive to the momenta of the particles.

$$qvB = m\omega^2 r = m \frac{v^2}{r}$$

$$\Leftrightarrow p = qBr$$

Therefore the abscissa can only be changed to the energy of a certain charge to mass ratio. In Figure 6.8, showing the energy spectrum for two different RF power levels, this was done for protons. The accelerated protons are clearly noticeable at an energy

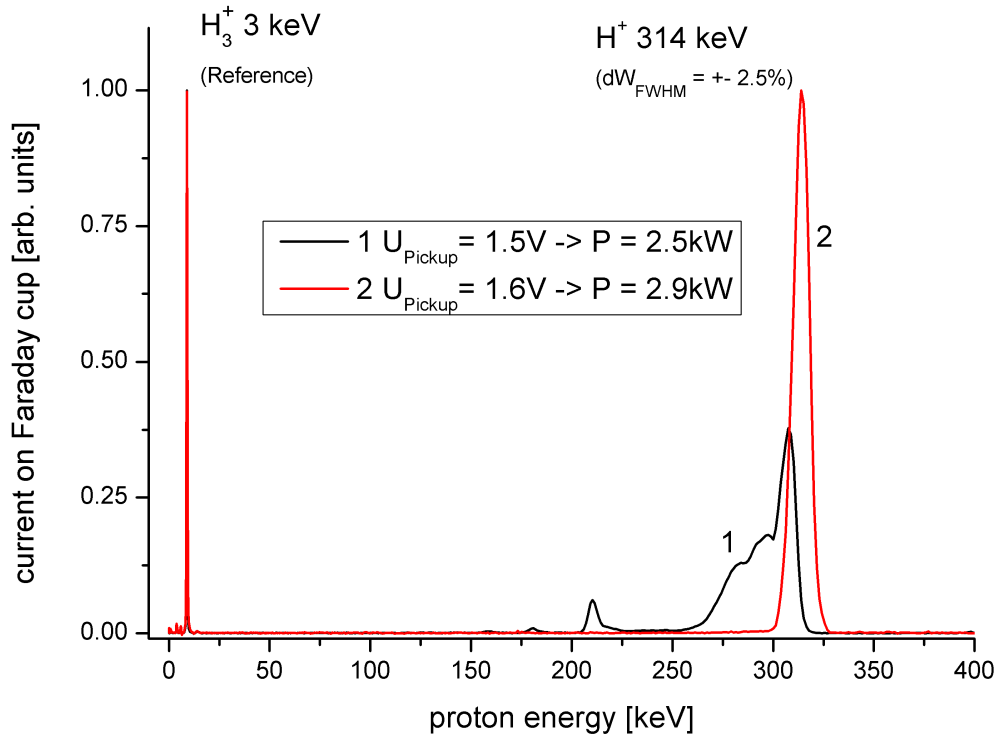


Figure 6.8: Energy spectrum of a proton beam with different RF power levels.

of about 314 keV (red curve). The design energy of the IH-RFQ is 300 keV/u for a frequency of 101.28 MHz, but the structure's resonance frequency now was 104.688 MHz. The fixed cell length of an accelerating cell is given by

$$cl = \frac{\beta\lambda}{2}.$$

A higher frequency and therefore a smaller wavelength λ leads to a higher β to maintain synchronism to the cell length. So a higher output energy was expected. The signal of an RF probe with a damping factor of 56.5 dB was measured to 1.6 V which is equivalent to an RF power of 2.8 kW. When the RF power level is not high enough (black curve), the acceleration process could not be completely finished and many particles leave the RFQ bunched, shaped, and accelerated to a certain fraction of the output energy. The black curve was produced with an RF power of 2.5 kW. With increasing RF power the RFQ gets pushed toward its operating point. This type of ion source produces a big fraction of H_3 . The intervane voltage and the injection energy are not high enough to accelerate these particles, but they get transported and show up in the energy spectrum with their injection energy. The RF power needed to accelerate protons can be used to calculate the R_p -value of the machine, if one assumes that the voltage on the electrodes is the same as in the simulation for acceleration. Doing so, a R_p -value of 32 k Ω was calculated. Since the unflatness of the IH-RFQ was round 15%, a higher value for the intervane voltage is necessary to accelerate particles. Simulations show that a 10% higher voltage should be assumed which leads to an increase of the R_p -value to 38 k Ω . This is a more realistic value.

6.4 Measurement of the Transmission

In beam dynamic simulations the transmission of a given structure is easy to determine, since all coordinates of all particles are known at any time, as well as the position where they get lost if they hit the electrodes. The transmission is the simple ratio of the number of particles at the start of the structure to the number of particles at the end. When it comes to determine the transmission of a real structure it is a rather difficult measure, because one has no knowledge of the number and position of the particles at all. Thus the beam currents before and behind the structure are determined. For measuring the beam current a Fast-Faraday cup has been used. To determine the beam current at the front end of the structure, only that fraction of the beam should

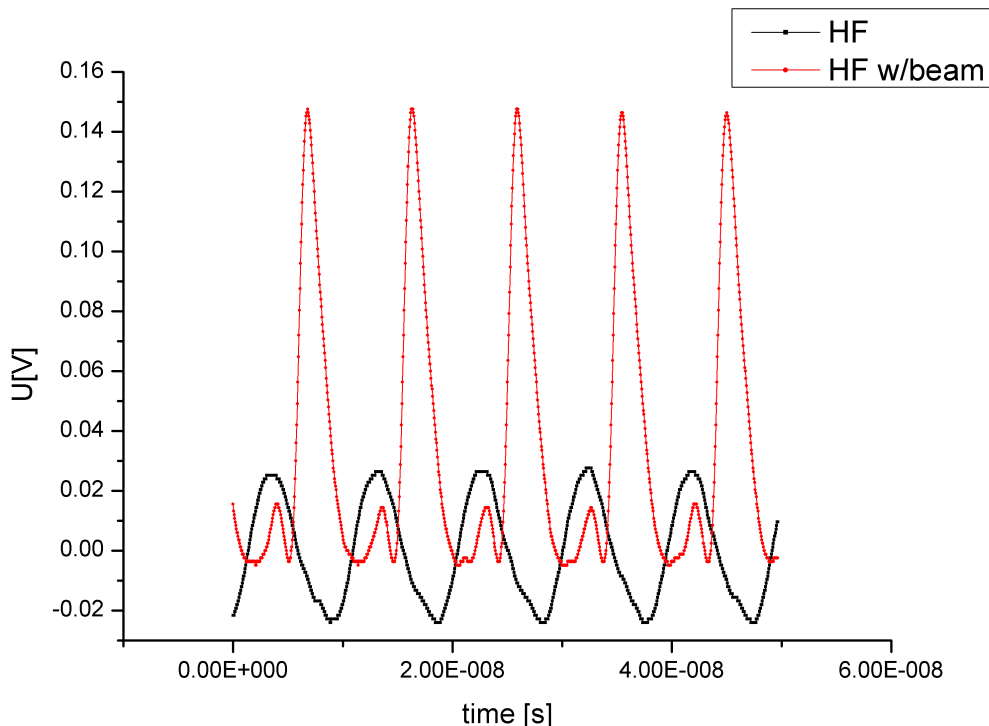


Figure 6.9: Signal on the fast Faraday cup after the RFQ with and without beam.

be considered which lies in the acceptance of the structure. If that is not done, the transmission will be far lower than it actually is. One feature of an RFQ is that it can bunch a dc beam, shape it and then accelerate it. Therefore normally a dc beam is injected into the RFQ and a bunched beam is ejected. For comparing a dc beam with a bunched beam the signal of the bunched beam has to be averaged an RF period. While bunching, all particles from a phase from -180° to 180° are ideally compressed into a phase width of $40 - 60^\circ$. Since current is charge per time, this leads to a higher peak current than for the same dc beam.

For measuring the transmission of the MAFF IH-RFQ the following setup for the beamline has been chosen: volume ion source which has been used before, Faraday cup with electrode to propel secondary electrons to measure the dc beam behind the ion source, a single solenoid lens to match the beam to the RFQ, RFQ, and a fast Faraday cup behind the RFQ to measure the bunched, accelerated beam. The beam current behind the ion source was measured to be 0.8 mA. The signal of the Faraday cup after the RFQ is shown on Figure 6.9. The black curve shows the signal when the ion source is turned off and only the RF is inducing a signal on the cup (a periodic

Input beam current	0.8 mA
Output peak current	3 mA
Average output current	0.6 mA
Transmission	75%
Phase width	90°
Intervane voltage need to accelerate (from simulation)	38 kV
RF-power	40 kW
R_p -value	38 – 44 kΩm

Table 6.2: Table of the measurement

signal with an average of zero). The red curve is the signal with beam and RF. One can clearly see the bunched beam with a peak current of 3 mA. The average current is 0.6 mA. This leads to a transmission of $75\% \pm 15\%$. The error of the transmission is due to the uncertainty of the beam current before the RFQ and the proper match to the RFQ and partly to the averaging of the signal behind the RFQ which should also get rid of the perturbation of the RF signal. To have a better picture of the shape of the bunched beam, the signal without the beam can be subtracted from the signal with beam. (One difficulty is to get the two signals in the right phase correlation.) This graph is shown on Figure 6.10 and can be used to calculate the phase spread of the beam. The FWHM of the bunch is $2.45 \cdot 10^{-9}$ s which is equivalent to a phase width of approximate 90°. The design phase width is about 42°. That and the shape of the curve with a much steeper increase of current than its decrease suggest that there are particles which have not been accelerated to their full energy and therefore lie behind the main bunch. A possible reason for that kind of longitudinal shape is that the intervane voltage is still a little to low and the limited resolution of the Faraday cup. The design intervane voltage is 9.5 kV per $\frac{q}{A}$. Therefore a voltage of 38 kV is needed for He^+ . The RF power for acceleration was measured to be about 40 kW with a two way coupler and with a pickup loop. This leads to a R_p -value of about 36 kΩ with a systematic error of $\pm 20\%$. Because of the unflatness of the field of the IH-RFQ a voltage of 42 kV is needed to accelerate. This corresponds to a R_p -value of 44 kΩ. Unfortunately, it was not possible to increase the RF-power due to limitations of the amplifier.

The uncertainty of the RF-power measurement is based on limitations of the coupler. The amplifier produces a certain fraction of higher harmonics; the higher the output level, the bigger the fraction of higher harmonics. This higher harmonics leads to an additional error of the RF power measurement.

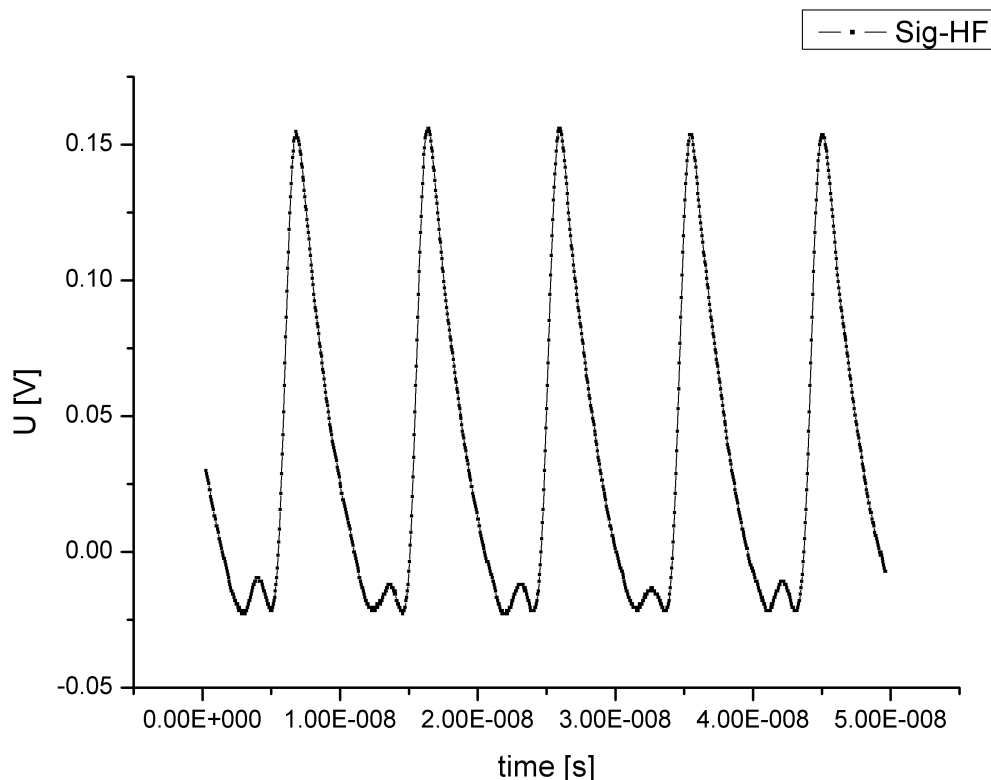


Figure 6.10: Difference of the two signals of Figure 6.9.

Perturbation Capacitor (average)	46 k Ω
Gamma Spectroscopy	42 k Ω
Acceleration of protons	38 k Ω
Acceleration of He	44 k Ω
Average	42.6 k Ω standard deviation 3.6 k Ω

Table 6.3: Overview of the different measurements of the R_p -value.

6.5 Overview of Shunt Impedance Measurements

The shunt impedance of the MAFF IH-RFQ has been measured using different techniques. Table 6.3 gives an overview of the different results. Although the error of each measurement was estimated to be quite high, the four different methods have an average of $42.6 \text{ k}\Omega \pm 3.6 \text{ k}\Omega$. The standard deviation is less than 10%. The length normalized shunt impedance of the MAFF IH-RFQ is $128 \text{ k}\Omega\text{m}$ and is therefore in the range of REX-ISOLDE RFQ.

6.6 Comparison to beam dynamic simulations

For simulating particle dynamic of the MAFF IH-RFQ the RFQ-structure parameters (a, m, L, V) were used to get the information of the actual shape of the vanes. Other parameters like input energy, beam current, frequency et cetera. are also known. The only data which is roughly known is the input emittance of the beam. The characteristics of the volume ion source was determined as a diploma work by J. Fischbach [Fis10], but was modified to match the IH-RFQ. For an accurate simulation of the RFQ the emittance in front of the vanes (RFQ) behind the solenoid needs to be known. For the following simulation the input emittance was estimated to be 0.015 cm rad (see Table 6.4).

beam current	0.8 mA
ϵ	0.015 cm rad
α	1.17
β	8.090 cm rad

Table 6.4: Overview of the input beam.

The evolution of the simulation in terms of x,y position, phase and energy is shown in Figure 6.11. The oscillation in the transverse planes indicate that the beam is slightly mismatched in the beginning of the RFQ. The bunching process takes place quite well (phase plot), but some particles leave the bucket at the end of the RFQ and fall behind. At the beginning of the RFQ the energy of all particles is the same. After some distance, when the bunching process has started, the energy distribution of the particles is expanded. Some gain and some loose energy. At the end of the structure, the energy spread of the beam is reduced to less than 25 keV/u. A small fraction of particles get transported with the wrong energy. The transmission in this case is about 77% and the percentage of accelerated particles is about 75%. The shape of the beam in the last cell of the IH-RFQ is shown in Figure 6.12. It is focused in the x-plane and it is defocused in the y-plane. The phase width of the bunch is about 30° by an energy spread of less than 25 keV. The small fraction of unaccelerated beam is not shown in these graphs.

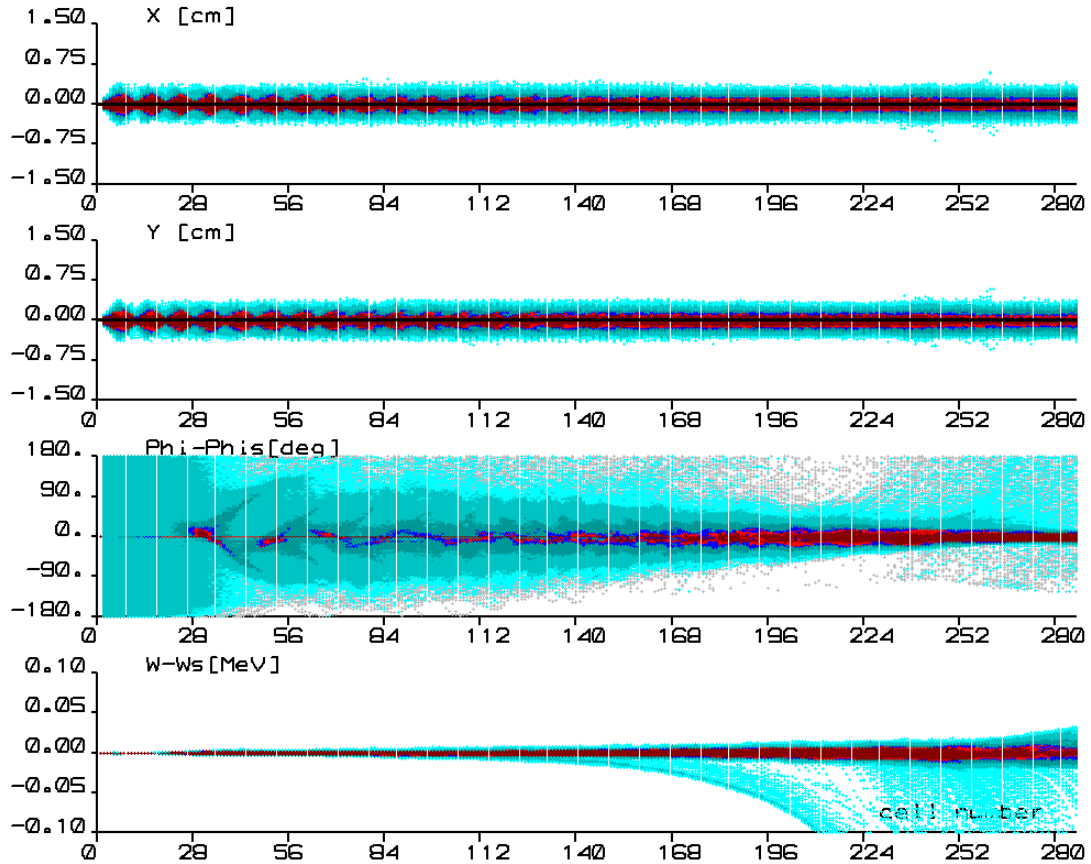


Figure 6.11: Evolution of the simulation of the MAFF IH-RFQ.

6.7 Conclusion

The measurements discussed above show that the MAFF IH-RFQ was assembled correctly and is capable of accelerating particles with a mass to charge ratio of 4. The problems solved include the bad R_p -value due to the tuning plates, replacement of the injection system, intensive conditioning of the RFQ, and using precise measuring methods for the beam current especially with the fast Faraday cup. Problems still to overcome are mainly to eliminate the limitation of the structure to operate at higher RF-levels. There are some regions in the RFQ which are sources for sparking, which should be upgraded. A more precise measurement of the transmission including measurements of the emittance at the entrance of the RFQ and behind the RFQ are needed which leads to a larger experimental setup to compare them to simulations more precisely. The measured values for the impedance, beam transmission and beam energy of the MAFF IH-RFQ were close to the design parameters.

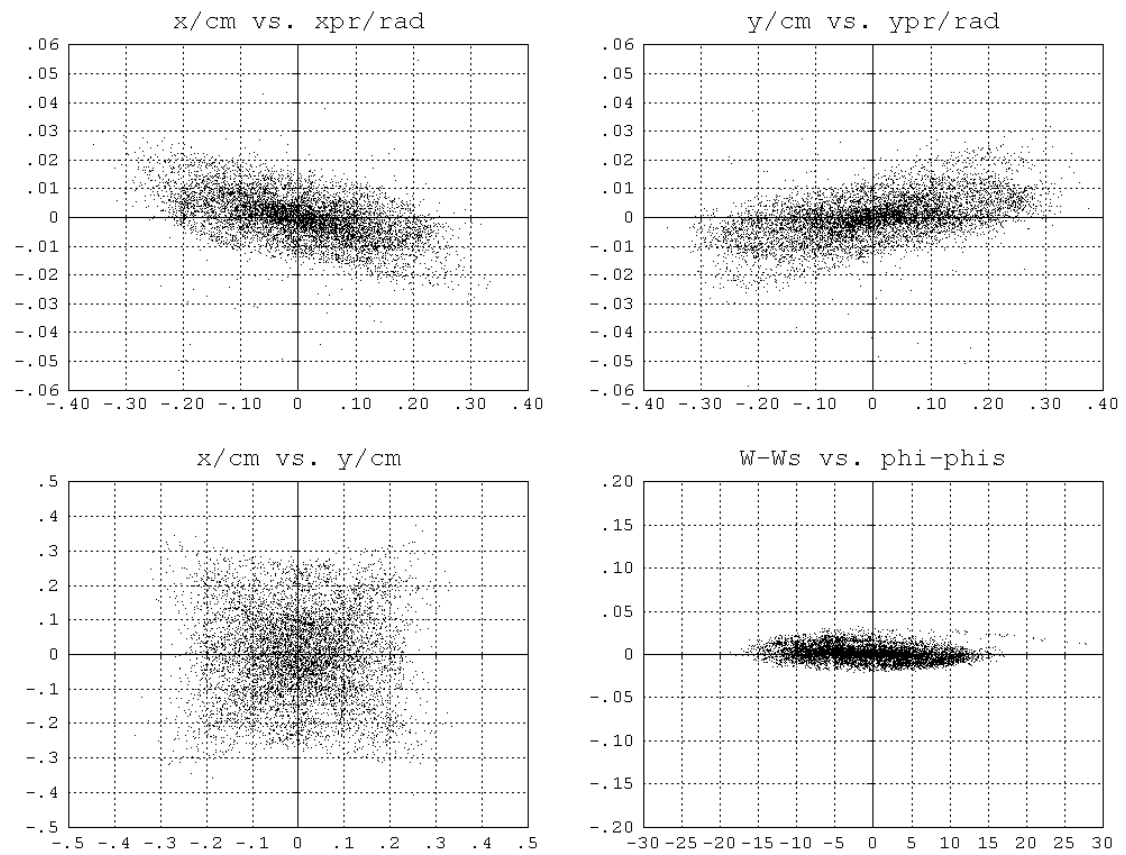


Figure 6.12: Beam in the last cell of the MAFF IH-RFQ.

7 Summary

A basic introduction to RFQs has been given in the first part of this thesis. The principle and the main ideas of the RFQ have been described and a small summary of different resonator concepts has been given. Two different strategies of designing RFQs have been introduced. The analytic description of the electric fields inside the quadrupole channel has been derived and the two term simplification was shown as well as the limitation of these approaches.

The main work of this thesis was the implementation and analysis of a multigrid Poisson solver to describe the potential and electric field of RFQs which are needed to simulate the particle dynamics accurately. The main two ingredients of a multigrid Poisson solver are the ability of a Gauß-Seidel iteration method to smooth the error of an approximation within a few iteration steps and the coarse grid principle. The smoothing corresponds to a damping of the high frequency components of the error. After the smoothing, the error term can well be approximated on a coarser grid in which the low frequency components of the error on the fine grid are converted to high frequency errors on the coarse grid which can be damped further with the same Gauß-Seidel method.

After implementation, the multigrid Poisson solver was analyzed using two different type of test problems: with and without a charge density. These two situations correspond to the calculation of the internal and external fields of RFQs. As a charge density, a homogeneously charged ball and cylinder were used to represent the bunched and unbunched beam and placed inside a quadruple channel. The solver showed a good performance.

Next, the performance of the solver to calculate the external potentials (and fields) of RFQs was analyzed. First, the potentials and corresponding electric field components were illustrated for different geometries of RFQ cells in terms of modulation, cell length and aperture. After illustrating the results of the multigrid Poisson solver, a comparison to the field of the old multipole expansion method was made. The multipole expansion method is an accurate representation of the field within the

minimum aperture, as limited by cylindrical symmetry. Within these limitations the multigrid Poisson solver and the multipole expansion method agree well. Beyond the limitation the two methods give different fields. It was shown that particles leave the region in which the multipole expansion method gives correct fields and that the transmission is affected therefrom as well as the single particle dynamic. The multigrid Poisson solver also gives a more realistic description of the field in the beginning of the RFQ, because it takes the tank wall into account, and this effect is shown as well. Closing the analysis of the external field, the transmission and fraction of accelerated particles of the set of 12 RFQs for the two different methods were shown. For RFQs with small apertures and big modulations the two different methods give different values for the transmission due to the limitation of the multipole expansion method.

The internal space charge fields without images was analyzed at the level of single particle dynamic and compared to the well known SCHEFF routine from LANL, showing major differences for the analyzed particle. For comparing influences on the transmissions of the set of 12 RFQs a third space charge routine (PICNIC) was considered as well. The basic shape of the transmission curve was the same independent of space charge routines, but the absolute values differ a little from routine to routine, with SCHEFF about 2% lower than the other routines. The multigrid Poisson solver and PICNIC agree quite well (less than 1%), but PICNIC has an extremely long running time.

The major advantage of the multigrid Poisson solver in calculating space charge effects compared to the other two routines used here is that the Poisson solver can take the effect of image charges on the electrodes into account by just changing the boundaries to have the shape of the vanes whereas all other settings remain unchanged. The influence of doing so on the potentials and field are shown. It was demonstrated that the effect of image charges on the vanes on the space charge field is very big in the region close to the electrodes. Particles in that region will see a stronger transversely defocusing force than without images. The result is that the transmission decreases by as much as 10% which is considerably more than determined by other (inexact) routines before. This is an important result, because knowing about the big effect of image charges on the electrodes it allows it to be taken into account while designing the RFQ to increase the performance of the machine. It is also an important factor in resolving the traditional difference observed between the transmission of actual RFQs and the transmission predicted by earlier simulations.

In the last chapter of this thesis some experimental work on the MAFF (Mu-

nich Accelerator for Fission Fragments) IH-RFQ is described. The MAFF RFQ was designed to accelerate very neutron-rich fission fragments for various experiments. The machine was assembled in Frankfurt and a beam test stand was built. As a part of this thesis the shunt impedance of the structure was measured using different techniques, the output energy of the structure were measured and finally its transmission was determined and compared to the beam dynamics simulations of the RFQ. Unfortunately, the transmission measurements were done without exact knowledge of the beam's emittance. So the comparison to the simulation is somewhat rough, but with a reasonable guess of the emittance a good comparison between the measurement and simulation was obtained.

Bibliography

- [AFM⁺89] ARAI, S. ; FUKUSHIMA, T. ; MORIMOTO, T. ; TOJYO, E. ; TOKUDA, N. ; YOSHIZAWA, M. ; HATTORI, T.: Development of a split coaxial RFQ at INS. In: *Nuclear Instruments and Methods in Physics Research Section A: Accelerators, Spectrometers, Detectors and Associated Equipment* 278 (1989), Nr. 1, S. 236 – 240. – ISSN 0168–9002. – Proceeding of the International Symposium on Heavy Ion Inertial Fusion Darmstadt, FRG, June 28-30, 1988
- [Bec97] BECHTOLD, A.: *Aufbau eines Schwerionen-RFQ-Beschleunigers mit hohem Tastverhältnis*, Goethe-Universität, Diplomarbeit, 1997
- [BHF⁺06] BECHTOLD, A. ; HABS, D. ; FISCHBACH, J. ; RATZINGER, U. ; REHBERG, J. ; REICHWEIN, M. ; SCHEMPF, A. ; KESTER, O. ; HÄUSER, J.: The MAFF IH-RFQ test stand at the IAP Frankfurt. In: *Proceedings of EPAC 2006*, 2006, S. 1577–1579
- [Cra84] CRANDALL, K. R.: RFQ Radial Matching Sections and Fringe Fields. In: *Proceedings of the 1984 Linear Accelerator Conference* GSI-84-11, May 7-11, 1984, S. 109–111
- [CSW79] CRANDALL, K. R. ; STOKES, R.H. ; WANGLER, T.P.: RF Quadrupole Beam Dynamic Design Studies. In: WITKOVER, R. L. (Hrsg.) ; Brookhaven National Laboratory (Veranst.): *Proceedings of the 1979 Linear Accelerator Conference* Brookhaven National Laboratory, 1979, S. 205–216
- [CWY⁺05] CRANDALL, K. ; WANGLER, T. ; YOUNG, L. ; J. BILLEN, G. N. ; SCHRAGE, D.: *RFQ Design Codes*. Bd. LA-UR-96-1836. Los Alamos National Laboratory, 2005
- [Dei87] DEITINGHOFF, H.: Zur Bedienung des PARMTEQ-Programms auf der IBM der GSI / Institut für Angewandte Physik. 1987 (Int-Rep. 87-18). – Int-Rep.
- [Dup00] DUPERRIER, R.: *Intense Beam Dynamics in RFQ*, Universite de PARIS-SUD U.F.R. Scientifique d’Orsay, Diss., July 2000

-
- [Fis07] FISCHER, P.: *Ein Hochleistungs-RFQ-Beschleuniger für Deuteronen*, Fachbereich Physik der Johann Wolfgang Goethe - Universität Frankfurt am Main, Diss., 2007
- [Fis10] FISCHBACH, J.: *Aufbau und Inbetriebnahme einer Volumen-Ionenquelle für den Teststand des MAFF IH-RFQ*, Institut für Angewandte Physik, Goethe-Universität, Frankfurt am Main, Diplomarbeit, 2010
- [HAA⁺01] HABS, D. ; AMES, F. ; ASSMANN, W. ; EMHOFER, S. ; ENGELS, O. ; GROSS, M. ; KESTER, O. ; MAIER, H. J. ; REITER, P. ; SIEBER, T. ; THIROLF, P.: The REX-ISOLDE-project and the Munich accelerator for fission fragments MAFF. In: *Progress in Particle and Nuclear Physics* 46 (2001), Nr. 1, S. 343 – 358. – ISSN 0146–6410
- [HE88] HOCKNEY, R. W. ; EASTWOOD, J. W.: *Computer Simulation Using Particles*. Bristol: Hilger, 1988
- [HGA⁺03] HABS, D. ; GROSS, M. ; ASSMANN, W. ; AMES, F. ; BONGERS, H. ; EMHOFER, S. ; HEINZ, S. ; HENRY, S. ; KESTER, O. ; NEUMAYR, J. ; OSPALD, F. ; REITER, P. ; SIEBER, T. ; SZERYPO, J. ; THIROLF, P. G. ; VARENTSOV, V. ; WILFART, T. ; FAESTERMANN, T. ; KRÜCKEN, R. ; MAIER-KOMOR, P.: The Munich accelerator for fission fragments MAFF. In: *Nuclear Instruments and Methods in Physics Research Section B: Beam Interactions with Materials and Atoms* 204 (2003), S. 739 – 745. – ISSN 0168–583X. – 14th International Conference on Electromagnetic Isotope Separators and Techniques Related to their Applications
- [HKB⁺97] HABS, D. ; KESTER, O. ; BOLLEN, G. ; LILJEBY, L. ; RENSFELT, K. G. ; SCHWALM, D. ; HAHN, R. von ; WALTER, G. ; DUPPEN, P. V.: The REX-ISOLDE project. In: *Nuclear Physics A* 616 (1997), Nr. 1-2, S. 29 – 38. – ISSN 0375–9474. – Radioactive Nuclear Beams
- [HKS⁺98] HABS, D. ; KESTER, O. ; SIEBER, T. ; KOLBE, A. ; OTT, J. ; BOLLEN, G. ; AMES, F. ; SCHWALM, D. ; HAHN, R. von ; REPNOW, R. ; PODLECH, H. ; SCHEMPP, A. ; RATZINGER, U. ; LILJEBY, L. ; RENSFELT, K. G. ; WENANDER, F. ; JONSSON, B. ; NYMAN, G. ; DUPPEN, P. V. ; HUYSE, M. ; RICHTER, A. ; SHRIEDER, G. ; WALTER, G. ; COLLABORATION, REX-ISOLDE: The REX-ISOLDE project. In: *Nuclear Instruments and Methods in Physics Research Section B: Beam Interactions with Materials and Atoms* 139 (1998), Nr. 1-4, S. 128 – 135. – ISSN 0168–583X
- [Jac62] JACKSON, J. D.: *Classical Electrodynamics*. New York : John Wiley & Sons, 1962
- [Jam81] JAMESON, R. A.: Equipartitioning in linear accelerators. In: *Proceedings of the 1981 Linear Accelerator Conference* (1981)
-

-
- [Jam93] JAMESON, R. A.: On scaling and optimization of high-intensity, low-beam-loss RF linacs for neutron source drivers. In: *AIP Conf. Proc.* 279 (1993), S. 969–998
- [Jam97] JAMESON, R. A.: A Discussion of RFQ Linac Simulation / Los Alamos National Laboratory. 1997 (LA-CP-97-54). – Report. – Re-published as LA-UR-07-0876, 2/8/07
- [Jam07a] JAMESON, R. A.: RFQ Designs and Beam-Loss Distributions for IFMIF / Oak Ridge National Laboratory (ORNL). 2007 (ORNL/TM-2007/001). – Technical Report
- [Jam07b] JAMESON, R. A.: RFQ Design Studies - Investigation (incomplete) of Dependence of Optimization on Codes. In: *st EU-JA Workshop on IFMIF-EVEDA Accelerator* (7-9 March 2007). – Paris, France
- [Kle83] KLEIN, H.: Development of the different RFQ accelerating structures and operation experience. In: *IEEE Transactions on Nuclear Science* Vol. NS-30 (1983), August, Nr. No. 4, S. 3313
- [KT70] KAPCHINSKIY, M. ; TEPLYAKOV, V.A.: Linear Ion Accelerator with Spatially Homogenous Focusing. In: *Prib. Tekh. Eksp.* 119, No. 2 (1970)
- [LJDK96] LI, D. ; JAMESON, R. A. ; DEITINGHOFF, H. ; KLEIN, H.: PARTICLE DYNAMICS DESIGN ASPECTS FOR AN IFMIF D+ RFQ. In: *Proceedings of EPAC96* (1996)
- [LLD⁺89] LEIPE, P. ; LANGBEIN, K. ; DEITINGHOF, H. ; KLEIN, H. ; SCHEMPP, A.: Acceleration of intense proton beam with split coaxial four-rod RFQ. In: *Nuclear Instruments and Methods in Physics Research Section A: Accelerators, Spectrometers, Detectors and Associated Equipment* 278 (1989), Nr. 1, S. 213 – 219. – ISSN 0168–9002. – Proceeding of the International Symposium on Heavy Ion Inertial Fusion Darmstadt, FRG, June 28-30, 1988
- [Mau08] MAUS, J.: *Untersuchungen zur Teilchendynamiksimulation in RFQs*, Institut für Angewandte Physik, Johann Wolfgang Goethe-Universität, Frankfurt am Main, Diplomarbeit, 2008
- [MCM⁺06] MEUSEL, O. ; CHAU, L.P. ; MUELLER, I. ; RATZINGER, U. ; SCHEMPP, A. ; VOLK, K. ; ZHANG, C.: Development Of An Intense Neutron Source “FRANZ” In Frankfurt. In: *Proceedings of LINAC 2006, Knoxville, Tennessee USA* (2006), S. 159 – 161
- [Mül79] MÜLLER, R. W.: Layout of a High Intensity Linac for Very Heavy Ions With RF Quadrupole Focusing. In: *GSI-Report 79-7, Darmstadt* (1979)

-
- [Mül09] MÜLLER, I.: *Unofficial verbal lecture*. November 2009
- [MPJ⁺00] MEUSEL, O. ; POZIMSKI, J. ; JAKOB, A. ; LAKATOS, A. ; KLEIN, H.: Low Energy Beam Transport for Heavy Ions using Space Charge Lenses. In: *Proceedings of EPAC 2000*, 2000, S. 2258
- [PKHS] PASINI, M ; KESTER O. ; HABS, D. ; SIEBER, T.: RF Design of the MAFF IH-RFQ. In: *Proceedings of EPAC 2004*, S. 1216
- [PLN98] PICHOFF, N. ; LAGNIEL, J.M. ; NATH, S.: Simulation results with an alternate 3D space charge routine, PICNIC. In: *Proceedings of the 1997 Linear Accelerator Conference, Chicago (1998)*, S. 141–143
- [Pod08] PODLECH, H.: *Anwendungen der Supraleitung in Beschleuniger- und Fusionstechnologie*. IAP - Universität Frankfurt, 2008
- [Rat96] RATZINGER, U.: The New GSI Prestripper Linac for High Current Heavy Ion Beams. In: *Proceedings of the LINAC 96 (1996)*, S. 288–292
- [Rat98] RATZINGER, U.: *Effiziente Hochfrequenz-Linearbeschleuniger für leichte und schwere Ionen*. Habilitationsschrift, 1998
- [Sch90] SCHEMPP, A.: *Beiträge zur Entwicklung der Radiofrequenz- Quadrupol (RFQ)-Beschleuniger*. Habilitationsschrift, Inst. f. Angew. Physik, Frankfurt am Main, 1990
- [Sch96] SCHEMPP, A.: Design of compact RFQS. In: *Proceedings of the 1996 Linear Accelerator Conference (1996)*, S. 53–55
- [Sie01] SIEBER, T.: *Entwicklung von 4-Rod- und IH- Radio-Frequenz-Quadrupol (RFQ)-Beschleunigern für radioaktive Ionenstrahlen bei REX-ISOLDE und MAFF*, Ludwig-Maximilians-Universität München, Diss., 2001
- [SKH01] SIEBER, T. ; KESTER, O. ; HABS, D.: Comparison of 4-Rod and IH-RFQ accelerator at 101 MHz. In: *Annual report of the Beschleunigerlaboratorium der LMU München and TU München (2001)*
- [Sta90] STAPLES, J. W.: *RFQ's-An Introduction*. Lawrence Berkeley Laboratory University of California Berkeley, California, September 1990
- [Thi07] THIBUS, J.: *Numerische Berechnung zum Ionenstrahl-Funneling*, Fachbereich Physik der Johann Wolfgang Goethe - Universität Frankfurt am Main, Diss., 2007
- [TOS01] TROTTENBERG, U. ; OOSTERLEE, C. ; SCHÜLLER, A.: *Multigrid*. Academic Press, 2001
- [Wan98] WANGLER, Th.: *RF Linear Accelerators*. 2. Wiley, 1998 (II)

- [YJL⁺06] YAN, X.Q. ; JAMESON, R.A. ; LU, Y.R. ; .GUO, Z.Y ; FANG, J.X. ; CHEN, J.E.: MATCHED AND EQUIPARTITIONED METHOD FOR HIGHINTENSITY RFQ ACCELERATORS. In: *Proceedings of EPAC06*. Edinburgh, Scotland, 2006, S. 2814ff
- [ZBH⁺08] ZIMMERMANN, H. ; BECHTOLD, A. ; HABS, D. ; KOLB, P. ; SCHEMPP, A.: Beam Tests With The MAFF IH-RFQ At The IAP-Frankfurt. In: *Proceedings of EPAC 2008*. Genoa, Italy, 2008, S. 817–819
- [Zha05] ZHANG, C.: *Research on High Current Radio Frequency Quadrupole Accelerators for Neutron Production*, School of Physics, Peking University, Diss., 2005
- [ZJZ⁺08] ZHANG, Zhou-Li ; JAMESON, R.A. ; ZHAO, Hong-Wei ; LIU, Yong ; ZHANG, Sheng-Hu ; ZHANG, Cong: Beam dynamics design of an RFQ for a planned accelerator, which uses a direct plasma injection scheme. In: *Nuclear Instruments and Methods in Physics Research Section A: Accelerators, Spectrometers, Detectors and Associated Equipment* 592 (2008), Nr. 3, S. 197 – 200. – ISSN 0168–9002

Lebenslauf

Persönliche Daten

Name	Johannes Maus
Geburtsdatum	15.08.1984
Geburtsort	Frankfurt am Main

Ausbildung

1991 - 1994	Ebelfeldschule, Grundschule, Frankfurt
1994 – 2001	Liebigschule, Gymnasium, Frankfurt
2001 – 2002	Naaman Forest High School, Garland, Texas, USA
2002 – 2004	Liebigschule, Gymnasium, Frankfurt
06/2004	Abitur
2004-2008	Studium der Physik an der Johann Wolfgang Goethe Universität, Frankfurt
08/2006	Diplom-Vorprüfung, Nebenfach: Geophysik
09/2006-04/2008	Diplomarbeit: “Untersuchungen zur Teilchendynamik-simulation in RFQs”
04/2008	Diplom-Hauptprüfung, Nebenfach: Astronomie
2008	Anstellung als wissenschaftlicher Mitarbeiter am Institut für Angewandte Physik. Beginn der Arbeiten zur vorliegenden Dissertation

Akademische Lehrer

H. Appelshäuser, J. Baumeister, T. Boller, R. Dörner, C. Gros, W. Hofstetter, M. Huth, J. Jacoby, M. Kasner, P. Kopietz, M. Lang, G. Marinescu, J. A. Maruhn, H. Podlech, U. Ratzinger, H. Roskos, G. Rumpker, H. Schmeling, A. Schempp, T. Stöhlker, H. Ströbele, J. Struckmeier, R. Tetzlaff, J. Weidmann, B. Wiedemann, H. Zimmermann,

Danksagung

Zuerst möchte ich Herrn Prof. Dr. A. Schempp für die Aufnahme in seine Arbeitsgruppe danken. Für seine gute Betreuung und für die Freiheiten, die er mir bei der Arbeit ließ, bin ich ihm ebenso zu Dank verpflichtet wie für seine Unterstützung von Projekten, die über die Arbeit hinaus gingen. Mein Dank gilt ebenfalls Herrn Prof. Dr. U. Ratzinger für sein Interesse an dieser Arbeit.

Herrn Dr. R. A. Jameson danke ich besonders für die großartige Zusammenarbeit in den letzten zwei Jahren. Durch sein ständiges Hinterfragen von Ergebnissen und seinen Sachverstand habe ich sehr viel gelernt. Bedanken möchte ich mich auch für seine Einführung in die Kunst RFQs zu designen und seiner Hilfe beim „Debuggen“.

Den Herren Dr. A. Bechtold und Dr. H. Zimmermann möchte ich für ihre Einleitungen in das Experimentieren am RFQ danken. Auch dies war jeweils eine sehr angenehme und erfolgreiche Zusammenarbeit. Herrn Dr. O. Meusel gilt mein Dank für seine Hilfe zur Durchführung der Transmissionsmessung. Ein großes Dankeschön geht an die Werkstatt unter der Leitung von Herrn Reploeg und an Herrn I. Müller für viele Reparaturen und lehrreiche Gespräche.

Meinem Zimmerkollegen U. Bartz möchte ich sehr für die angenehme Atmosphäre und Gespräche physikalischer sowie nicht physikalischer Natur danken. Danken möchte ich auch der gesamten Arbeitsgruppe Schempp. Es ist ein Haufen voller wunderbarer Chaoten, die es stets schaffen eine angenehme „Arbeitsatmosphäre“ aufkommen zu lassen ohne den Bezug zum Angenehmen zu verlieren.

Ein ganz besonderes Dankeschön möchte ich an meine Eltern Jutta und Arnold richten für ihre große Unterstützung, Geduld und Reflektionen. Zum Schluss noch ein ganz herzlichen Danke an meine Verlobte Sonja für Geduld, liebevolle Unterstützung und Motivation.